An Acousto-optical Correlation Spectrometer

for

Radio Astronomy

Thesis by

Kwok-wai Cheung

In Partial fulfillment of the Requirements

for the Degree of

Doctor of Philosophy

California Institute of Technology

Pasadena, California

1987

(Submitted March 23, 1987)

to my parents

Acknowledgements

During the past few years of graduate study at Caltech, I have been very fortunate to be able to work at Robinson, where I met many wonderful people, teachers and friends, who gave me much enlightenment, affection, and love, and where I enjoyed an extremely satisfying and rewarding graduate student life. But most of all, I am particularly indebted to my advisor Professor A.T.Moffet, who has given me so much guidance, help and support throughout these years, and I appreciate all the things he has done for me especially in a few situations when I was in big trouble. I enjoyed all the freedom he gave me in selecting my research directions, and the encouragement to venture into many new research areas.

I'd like to thank many professors and colleagues who have been my teachers in various matters, especially Professor K.Y.Lo, who has been very hospitable, and who has put in an enormous amount of time educating me. Whether I become a good scientist or not, I appreciate all the care he has given me, I thank Professors T.J.Phillips and N.Z.Scoville, who have given me valuable advice and provided generous support at various times in my endeavor. Thanks go to Professor K.Libbrecht, who lent me his video camera in one of my emergencies. At the same time, I would also like to acknowledge the financial support provided by Caltech in the form of Graduate Teaching Assistantships and Graduate Research Assistantships, the NSF in the form of Graduate Research Assistantships, the Rosen Grant for the Compaq personal computers used in this research, and the Caltech President's Fund that has provided the bulk of the research funds which

made this research possible.

To the Caltech millimeter wave group and to the Owens Valley Radio Observatory staffs, I have to give my heartful thanks and admiration. Their dedicated professionalism and efficiency were manifested in my numerous encounters at the Observatory. In particular, Chief system engineer Dr.S.Scott has spent a lot of time explaining the interferometer system to me, and has helped me to interface my instrument with the system and to debug the instrument. Dr.C.Masson has helped me to start up the experimental setup and to debug the instrument, and his advice and help at various stages were very beneficial to me. Members of the professional staff Drs.G.Berge, D.Woody A.Sargent, T.Seling and S.Padin have given me a lot of help and counsel. At the observatory, I enjoyed Edna's cooking very much. Various help from Wayne, Ray, Ron, Jack, John, Larry, Harry, Kirk, Mark and Nancy are appreciated, especially Tom and Chick, who gave me a 'ton' of help during the set up of the optical table.

All the folks in Robinson have been very kind and helpful to me, and I would like to acknowledge everyone who has given me help and care in this pleasant place. It is impossible to acknowledge everyone, but below is a list of the people who have been particularly affected by my various requests for help during these years: F.Barnum, C.M.Chan, P.Chan, G.Dvorak, F.Harris, C.Herman, L.Kershaw, J.King, H.Knudson and J.Wolpert. This is the time to express my thankfulness to them.

All my fellow graduate students are good companions and gave me great moral support at various times over the years; in particular, Pawan has been the chief source. Haimin, Jim and Dean were also great office mates to have been with. Salute to Rick from whom I learned a lot of 'stereotype' American culture, to Fernando to whom I owed a computer, and to Steve for the help delivered during one of my emergencies.

To my friends at Caltech, I wish to say that their companionship has been

very meaningful and memorable. I have shared great moments in various social, cultural, recreational, physical, religious, entreprenurial and political projects with my former housemates Fai, Chi Fai, Peter, Tin Wu and Kwok Yin, and our distinguished mode of *sustai....ned* communication has been well known in Pasadena. Friends like Billy, Wilman & Wen, Vincent, Suk Man, Alex & Eta, Wen Jin, Ricky, Chuan, Kim, John, Ming Chung, Henry and Yiu Fai have been most wonderful to be with. The now defunct subCaltech organism Dà Yōng Guǎng had been a source of constant inspiration, excitement, and fun, and a place to learn about the biological behaviours of the microworld. As the retired master of this place, I have to express my great regret for its demise.

To my friends outside the institute, I wish to say that their companionship has been especially meaningful and will be eternal. To Timothy, who brought me into a venture which changed my life; to the Todd's family, Walter, Rita and Frank, who adopted me during my final days at Caltech and gave me family love and care; to Jenny, James, Kit, Kammy, and the whole kinship group who have given me much love; to William, Mr. and Mrs.Wu, and Mrs.Lai, who gave me much love and care.

Finally, and most importantly, I would like to express my deepest thanks to my family, especially my mother, my grandmother, my sisters, my brother and my brothers-in-law, my uncles and aunts, for their encouragement, support, and understanding. I dedicate this thesis to them.

Abstract

The objective of this thesis research is to develop and construct a wide-band, high resolution, two-channel prototype acousto-optic correlation spectrometer (AOCS) to analyze signals received by the three element millimeter-wave interferometer at Caltech's Owens Valley Radio Observatory (OVRO) which may be used to study the distribution of carbon monoxide and other molecules in galaxies.

The proposed correlation spectrometer has the main advantage of large time-bandwidth products and hence of low cost per frequency channel. Thus, it is suitable for many scientific objectives that require both large bandwidth and high resolution, such as mapping the distribution and temperature of the interstellar gases of galactic sources and extragalactic sources or studying the atmospheric conditions of planets in the solar system.

Phase switching has been used to reduce the zero level variation of this instrument, and is found to be more effective than other schemes used by the single dish acousto-optical spectrometers.

Both the frequency resolution and the frequency coverage of this instrument can be changed easily, and give it a flexibility not attainable by the filter-bank spectrometers. The relative light weight and compactness of this instrument make it a good candidate for outer space applications.

An absolute calibration of the instrument has been attempted by using the system temperature as a scale for both the correlated signal received and the noise fluc-

tuation of the instrument. A statistical method has been used to measure the various noise contributions of the instrument, which allows a very precise characterization of the zero level stability and the noise degradation of the system. The visibility loss of the present instrument was measured to be about 50%, and the noise degradation was about 40%. These losses were not due to any theoretical limitations but were the results of the imperfections in the present setup. They can be improved in the future versions of this instrument.

This instrument can be used to measure any RF spectrum and the cross spectrum of any two RF signals. Since it is a time integrating device, its sensitivity can be as high as one desires. With phase switching, one can compare the frequency characteristics of two closely matched microwave devices with great sensitivity. Because of its compactness, low cost and high sensitivity, it could be a useful and practical instrument for microwave measurements.

Contents

Chapter 1

Introduction

1.1 Aperture synthesis and spectral line radio astronomy

Radio telescopes achieve high angular resolution by correlating the signals from two or more antennas in a process known as aperture synthesis [33]. The complex correlaton between the signals from a pair of antennas is proportional to the Fourier component of the source map at a spatial frequency corresponding to the separation between the antennas, measured in wavelengths.

When observations are made of the spectral lines emitted by atoms or molecules in a distant astronomical object [84],[13], [14] the dimension of frequency is added to the two spatial dimensions of the map. These spectral line maps contain a lot of information that might reveal the physical conditions of the sources under study, such as the temperature, velocity and mass of gas flows, to help us to understand the underlying physics of the sources.

1.2 Scientific problems which require this new spectrometer

Because of the cost, one usually does not have a spectrometer with both large bandwidth and high resolution. For example, the filter bank correlation spectrometer at OVRO when this project began had only 32 channels and a total bandwidth of 32 MHz[1]

[1]The filter bank correlation spectrometer has now been expanded considerably, namely, 32 frequency channels each with 5MHz of resolution, 32 channels with 1MHz resolution and 32 channels with 50KHz

At the CO(J=1-0) frequency (about 115 GHz), it covered a velocity range of about 83 km/s. For nearby galactic objects (such as circumstellar star IRC10216 and planetary nebula NGC7027 [64]), which have a fairly small velocity spread, this velocity coverage was sufficient. But for extragalactic objects, which tend to have a much larger velocity spread due to doppler line broadening, this velocity coverage was not enough. Since we could not change the resolution or the bandwidth of the system, we had to use a less than optimum instrument when observing extragalactic objects.

For example, extended CO(J=1-0) emission had been discovered from the very interesting irregular galaxy M82, which appeared to explode outward from the nucleus of the galaxy [58],[59]. But the velocity coverage of 83km/sec allowed us to look at only a small portion of the gas distribution at a time, since M82 has a velocity spread of about 200 km/sec. Hence, a thorough study of this object would have taken three times more observation time. Obviously, this was not a good way to use our millimeter array considering the total cost of the array and the cost of the backend spectrometer. Similar situations were seen in IC342 [57] and M51 [85], which also have a large velocity spread and thus we were restricted to study only part of the spectrum.

At higher working frequencies, this problem was even more severe since the velocity coverage of the instrument is inversely proportional to the sky frequency. Thus, at about 230 GHz (CO J=2-1 transition), the 1MHz filter spectrometer covered only 43 km/sec. This was inadequate for studying most extragalactic sources.

Another case can be made in the study of planetary atmospheric conditions, where high resolution and large bandwidth are required to probe deeper into the atmosphere. For example, the CO (J=0-1) absorption line had been detected in the spectrum of Venus [48] and Mars [49]. The spectral line shows a very narrow absorption core (about

resolution. Only two of these three filters can be used simultaneously due to the limitations in the computer capability.

0.5 MHz half width) due to CO absorption at high altitude and very broad wings formed at lower altitude against atmospheric continuum emission. High resolution spectrometry is required to study the absorption core in order to determine the CO distribution high in the atmosphere, while low resolution, wide bandwidth studies are required for the broad wings at lower altitudes. Similarly, in the study of Titan [69], a resolution of about 1 MHz with a total bandwidth of more than 200 MHz is much more desirable than a single continuum channel [6]. These contradicting needs for various scientific objectives clearly requires a spectrometer with many channels and a high resolution.

1.3 Comparisons of major existing correlation spectrometers

Filter bank correlation spectrometers and digital correlation spectrometers are the two most commonly used spectrometers in aperture synthesis.

Filter bank channel spectrometers are the first generation spectrometers [32], [74]. Banks of filters are used to separate out different spectral components of the radio signal, and each component is then detected by a detector at the output of each filter. When RF signals from a single antenna dish are analyzed this way, the frequency spectrum of the RF signal is obtained. When the RF signal is from the output of a multiplying interferometer and the quadrature components of each spectral component are measured, the cross correlation of the two antennas for each spectral component is obtained.

Filter bank spectrometers suffered from channel nonuniformity because of the different filter responses from channel-to-channel [74]. This problem gets worse as the number of channels increases because of the impedance mismatch from channel-to-channel. Calibration must be done to correct for the channel non-uniformity. About 30% of power in any one channel is contributed by signal energy outside its half-power band because of the roll-off characteristics of the filter. Furthermore, such spectrometers

are very inflexible because the resolution and the number of channels cannot be changed easily.

If crystal filters (which are of higher qualities than the LC filters) are used, then the cost becomes the dominating factor because each crystal filter costs most than $300 each. Hence, the crystal filters alone for a 3-element interferometer with 64 channels cost more than $60,000. Besides, crystal filters with a large bandwidth (say 1MHz) are very expensive (>> $300 each). If LC filters are used, one is constrained by the Q-factor of the filter, which limits the total number of channels and the resolution of the filter. For example, it is very hard to design bandpass filters of the same bandwidth over more than about a 3:1 range of center frequencies [67]. Besides, each filter must be manually tuned and tested, and it is an extremely laborious process.

Digital correlation spectrometers, first proposed by Weinreb in 1963 [94], offer the flexibility lacking in filter bank spectrometers. The power spectrum is derived by Fourier-transforming the time-delay autocorrelation (or cross correlation function for interferometers) of the signal. Simply by changing the sampling rate and the baseband filter bandwidth, one can change the resolution of the spectrometer. It is very stable and less expensive than the filter bank spectrometers. But there is a moderate quantization loss during the initial analog to digital conversion [23],[26],[9],[10], and the hardware can become prohibitively costly when the number of quantization levels is more than three. Hence, it is a trade-off between hardware cost and system performance.

The most serious difficulty for this kind of spectrometer is that the spectral bandwidth is limited by the speed of the electronics. Digital electronics are presently difficult to implement with clock rates greater than 200MHz because of the delays of the gates and the crosstalks between them. Because of the sampling theorem, this is to say that the maximum bandwidth is less than 100MHz. But in millimeter wave astronomy,

we often come across situations that require a total bandwidth of a few hundred MHz [58]. In order to use the digital correlation technique in such a wide bandwidth environment, one must prefilter the wide bandwidth signal to several smaller bandwidth signals, which are then handled individually by digital correlators. Weinreb [95] has investigated the cost of such hybrid implementation. The price tag for the hardware (excluding the labor cost for assembling the components) for a single-channel hybrid spectrometer with 1.92 GHz bandwidth and 1920 resolution channels is about $200,000. To implement a similar correlator backend for our OVRO millimeter array would cost at least $500,000. If an array consists of 50 elements, then the cost would be over ten million dollars [95].

Chikada [19] has reported a new scheme to do the backend correlation for the Nobeyama five-element millimeter array. Basically, hardware FFT chips are used to transform the signals to frequency domain before they are cross-multiplied. The cross products are then accumulated and stored in memory for further processing. The maximum bandwidth is 320 MHz, adjustable to different resolutions for the 1024 resolution channels. With the support of the industries in Japan, this project has been completed. However, to reproduce a similar system would cost over one million dollars [46].

In conclusion, the traditional filter bank correlation spectrometer or digital correlation spectrometer or hybrid basically can do anything required in radio astronomy, but the cost might be prohibitively high. The goal of this research to see if acousto-optical technique can achieve the same performance less expensively.

1.4 The layout of this thesis

This thesis is divided into five chapters. Chapter 1 is an introduction to this research, which has been presented. In Chapter 2, the prototype acousto-optical correlation spectrometer is described. First, the single dish acousto-optical spectrometer

is reviewed. Then the architecture of the correlation spectrometer is described and its significant features are highlighted. After that, each part of the instrument is described in detail.

In Chapter 3, the system parameters that characterize the instrument are defined and the factors that affect these parameters are described. The two most important system parameters are the frequency resolution of the instrument and the signal-to-noise ratio (SNR) degradation of the instrument due to the various effects. All the factors that affect these two parameters are considered.

In Chapter 4, the performance of the instrument is measured. First the methodology of calibration is explained. Then the experimental setup for the measurement is outlined. The results of the measurements are then presented. The tests include the noise measurement of each part of the instrument, the resolution measurement, the sensitivity limit measurement, the visibility loss measurement, and the CW (single frequency) in the presence of uncorrelated noises measurement. Some data of astronomical measurement are presented at the end of the chapter.

In the concluding chapter, the various technical aspects of this research are discussed. Improvements to the present instrument are suggested. Finally, several schemes of expanding a two-element correlation spectrometer to a multi-element array are presented. Their relative merits and practicalities are discussed.

Chapter 2

The acousto-optical correlation spectrometer

In this chapter, the prototype acousto-optical correlation spectrometer is described. First, the single dish acousto-optical spectrometer is reviewed. Then the architecture of the correlation spectrometer is described and its significant features are highlighted. Detailed descriptions of each major part of the instrument are included in appendix A.

2.1 The single dish acousto-optical spectrometers

2.1.1 The principle of operation

The theory of acousto-optical deflection has been developed and verified for more than sixty years [12], [28]. The first acousto-optical spectrometer was built in the early 60's [54]. A commonly used configuration is shown in Fig. 2-1. It analyzes the radio signal as follows.

The radio signal is fed into a Bragg cell and produces ultrasonic waves, which deflect the incoming laser beam to different directions with different intensities depending on the frequency spectrum of the radio signal. The scattered laser light is collected by a linear array photo detector (such as a charge-coupled device or a photodiode array), and the spectrum of the radio signal is calculated from the amount of light collected at different directions. A summary of how the Bragg cell works is in appendix B.

2.1.2 The AOS in radio astronomy

Interest in making use of the acousto-optical effect to build large bandwidth, high resolution spectrometers in radio astronomy was aroused by Cole [22],[24],[25], when he developed a 1.5 MHz water-cell AOS with 20 KHz resolution. Since then, more powerful and better AOS have been constructed [47], [62], [66].

2.1.3 The advantages and problems with the AOS in radio astronomy

The advantages of using the acousto-optical deflectors in spectrometry are the large bandwidths, high resolutions, compactness (ideal for many applications in outer space), flexibility, simplicity in construction, and their relatively low cost. However, acousto-optical spectrometers also have their own problems. The most serious ones are the drift and the stability [62],[63].

Radio signals from galactic or extragalactic sources are many orders of magnitude weaker than typical communication or radar signals. In order to get a sufficient signal-to-noise ratio, one has to integrate for a long period of time. If the correlator is not stable enough, then there is a serious degradation to the integrated signal. Worse still, if there is a slow drift in the zero level of the instrument, the change may completely overwhelm the measurement. All kinds of mechanical vibrations, acoustic couplings and device aging tend to change the zero level of the instrument in the long term.

Recently, Masson[63] has reported the successful operation of a stable acousto-optical spectrometer, which demonstrates, to a certain extent, that the zero level variation can be minimized by a careful equipment setting and by calibrating the instrument frequently. Nonetheless, no one has been able to demonstrate that the acousto-optical correlator is stable enough for radio astronomy. Indeed, if a correlator works on the interference principle, it is even more sensitive to disturbances than the simple spectrometer,

since the interference fringes would be destroyed long before any amplitude fluctuation is seen. In a preliminary investigation, fringes had been seen to be destroyed merely by talking. For a sensitive instrument like this to work, one has to find some way to stabilize the instrument.

With a careful design of the mechanical mounting of the optical components, the vibration isolation of the optical bench, the removal of sensitive optical components, and the incorporation of a phase-switching scheme, it has been demonstrated in this research that acousto-optical correlation spectrometers are stable enough for astronomical measurements. The test data will be presented in Chapter four.

2.2 The prototype acousto-optical correlation spectrometers

2.2.1 Review of the different AOCS architectures

The possibility of using acousto-optics in interferometric spectrometry has been widely recognized by our colleagues throughout the world. For example, two Japanese groups [46],[19] and a Soviet group [30], had attempted to use acousto-optics in interferometric spectrometry. However, none of those prototype instruments performed well enough for them to be accepted by the astronomy community in routine observations.

The design used by Kai and Kosugi [46] consisted of an eleven-channel Bragg cell, interfering RF signals from eleven antennas simultaneously, and was used for single frequency observation of radio emissions from the sun at 160 MHz. Chikada [19] reported an attempt to use acousto-optics for multi-element interferometry at the Nobeyama Observatory. The report concluded with the various practical difficulties of such instruments, and their intention to abandon acousto-optics in favor of an FFT spectro-correlator. The Soviet group [30] used an architecture that directly multiplies the RF signals in the time domain before they are integrated. The scheme is elegant but there are no observational

data available.

The architecture based on the interference of two deflected laser beams [19] is adopted in this research because its architecture is very simple, and its popularity in phase array radar signal processing [27] made it well understood.

2.2.2 General description of the prototype instrument

The prototype AOCS (Fig. 2-2) is similar to the one described by Chikada [19]. Two single-channel Bragg cells are mounted on the two paths of a Mach-Zehnder-type interferometer. The laser beam is expanded to match the aperture height of the Bragg cells. The laser beam, after expanding in one dimension by the prisms, is split into two parallel and equal-intensity beams and illuminates the Bragg cells.

These two beams are Bragg-diffracted by the radio signals received from two antennas that drive the Bragg cells. Each beam produces a spectrum of the radio signal as in the single-channel AOS. The two deflected beams are then brought to interfere with each other by a mirror and a beam splitter. Since different frequency components are deflected at different angles, each frequency component of the two parallel spectra interferes with and only with the same frequency component of the other Bragg cell and produces interference fringes perpendicular to the frequency axis, similar to an ordinary two-slit interferometer illuminated with partially coherent light (Fig. 2-3). With an area array photo detector receiving the light, one can measure the fringe amplitude and the fringe phase of each frequency channel, and so the complex cross-power spectrum of the two signals can be calculated.

2.2.3 Extracting the fringes of each frequency component

As has been discussed above, different frequency components of the RF signals are diffracted at different directions, and so they do not interfere with one another. But

the same frequency components come out of the two Bragg cells in the same direction, and they interfere and produce fringes like a two-slit interferometer. So the problem of extracting the fringes of each frequency is the same as calculating the fringe visibility and phase of a two-slit interferometer. Consider coherent light propagating outward from two point sources with different amplitudes and phases (Fig. 2-4). The resultant amplitude in the Fraunhofer region is:

$$U(\theta) = a_1 \exp j(\phi_{a_1} + 2\pi d sin\theta/\lambda) + a_2 \exp j\phi_{a_2}. \tag{2.1}$$

The time-varying phase $\exp j\omega t$ has been left out for simplicity. The intensity in the Fraunhofer region is:

$$\begin{aligned} I(\theta) &= U(\theta)U^*(\theta) \\ &= a_1^2 + a_2^2 + 2a_1a_2\cos(2\pi d sin\theta/\lambda + \phi), \end{aligned} \tag{2.2}$$

where ϕ is $\phi_{a_1} - \phi_{a_2}$. Let $\theta_1, \theta_2, \theta_3$ and θ_4 be the angles such that $2\pi d \sin\theta/\lambda = 0^0$, 90^0, 180^0, 270^0, respectively. Then,

$$I(\theta_1) - I(\theta_3) = 4a_1a_2 cos\phi \tag{2.3}$$

$$I(\theta_2) - I(\theta_4) = 4a_1a_2 sin\phi. \tag{2.4}$$

Thus, one can determine the fringe amplitude and phase of the spectral correlation. In principle, one needs only three measurements to extract the fringe amplitude and phase. The advantages of taking four measurements are that the data-handling algorithm is simpler and that one can also make a correction if the separation between measurements is not exactly 90^0 (more details in Chapter 4).

If the point sources above are replaced by two rectangular apertures, then the fringes observed in the Fraunhofer region are modulated by the diffraction pattern of the apertures. The derivation is shown in Appendix C. This diffraction pattern must be corrected before the fringes are extracted.

2.2.4 Problems with the interfering AOCS

Basically, the problems with the interfering acousto-optical correlation spectrometers are the instability of the interference fringes, the difficulties in the separation of different fringes produced by the various combinations of the RF signals, the efficiency of the wide bandwidth Bragg cells, the laser power and the read-out rate requirement when the number of elements is large, and the performance degradation due to the detector noises [19].

Many of the above difficulties have been resolved as the technology advances with time. Most notable are the improvement of the Bragg cell efficiencies and bandwidths [37], and the CCD detector sensitivity. These advances have made acousto-optics attractive again, and it is important to find out if there are any fundamental difficulties that cannot be overcome.

Based on the above experiences [46],[19], [62], it appeared that the most difficult problem was the stability of the instrument. Therefore, we focused on a prototype two-channel correlation spectrometer in order to find out the stability of such instruments.

2.2.5 Features of the prototype AOCS

Single-channel commercial Bragg cells are used

The most distinctive difference between our instrument and Chikada's is that two single-channel Bragg cells are used instead of a single multi-channel Bragg cell. The use of two single-channel Bragg cells lowers the cost and also avoids the acoustic couplings between the channels that would give false correlation between the channels. For most new multi-channel Bragg cell designs, this problem has been carefully reduced. With two separate Bragg cells, it was found that the alignment of the Bragg cells and the phase shift across the frequency channels due to the difference in path lengths could be difficult

to handle practically.

Adjustable fringe separation

The separation of the two deflected beams from the Bragg cells can be adjusted by moving the mirror at the end of one arm of the interferometer (Fig. 2-2). In this way, the fringe width can be changed to match the detector geometry. This solved the difficult problem of expanding the fringe to the dimension of the detector [46].

Adjustable frequency resolution

The focal lengths of the cylindrical optics can also be changed by adjusting the separation between the concave and the convex lenses. This allows channel resolution and hence the total bandwidth to be changeable. Thus, the instrument is much more flexible than the filter-bank correlation spectrometers.

Phase Switching to remove the zero level

Phase switching is incorporated into the instrument by software. By alternately adding and subtracting frames that are phase-switched by 180^0, the zero level fluctuation of the instrument is eliminated. This is a bonus feature compared to a single-channel acousto-optical spectrometer whose zero-level has to be controlled [62],[63].

Compatibility with the existing backend correlators

The instrument was designed to operate in parallel with the existing filter bank correlators. The slow phase switching (see later section on phase switching for more details) had been incorporated and the data collection and integration of the AOCS had been synchronized with the entire interferometer. The fast phase switching can also be implemented into the AOCS by any of the following methods:

1. The addition of an electro-optical phase modulator on one arm of the AOCS optical path and phase switching at the fast phase switching rate.

2. Phase switching the RF going into one Bragg cell using a diode phase modulator.

3. Phase switching the RF going into one Bragg cell using a combination of an RF switch and a 180^0 hybrid.

However, it had not been implemented because the control computer and the CCD camera were not fast enough to handle all the data processing at the fast phase switching rate, and implementing it would not give any improvement on the zero level stability.

Inexpensive

In order to minimize the cost of such instruments, only components that are commercially available and relatively inexpensive are used. The overall hardware development cost for this prototype instrument (241 channels) is less than $20,000, including the cost of setting up the optical table and support.

Chapter 3

System analysis

In this chapter, the system parameters that characterize the instrument are defined and the factors that affect these parameters are described. The two most important system parameters are the frequency resolution of the instrument and the signal-to-noise ratio (SNR) degradation of the instrument due to the various effects.

The frequency resolution is basically limited by the time-bandwidth product of the Bragg cells, whereas many factors can contribute to the SNR degradation, namely, the detector noises, the A/D quantization error, the Bragg cell noises, the laser wavefront distortion (phase coherence) due to the surface roughness of all optical components or the air turbulence, and the fringe smearing due to the finite size of the detector pixels. These factors can be categorized into two types:

1. The lowering of the sensitivity by adding noise to the system.

2. The lowering of the visibility of the correlated signal.

The SNR degradation analysis provides answers to many system design questions, like the kind of detector to be chosen, the quality of optical components to be used, and the laser power required, etc. The sensitivity degradation can be related to the system time-bandwidth product, the charge capacity of the detector, and the frame time of integration. Thus, the optimal power requirements for the optical illumination and for driving the Bragg cells are obtained once the frame time of integration and the

area array detector characteristics are specified. These formulas will be derived in this chapter.

3.1 The frequency resolution

3.1.1 The definition of the resolution of the Bragg cell

The Rayleigh criterion is usually used to define the resolution of the Bragg cell [90]. When the Gaussian profile of illumination is considered, the resolution may be degraded by up to 25%, depending on the criteria used [77],[41].

3.1.2 The limit imposed by the time-bandwidth product of the Bragg cell

The effective time-bandwidth product is the same as the number of resolution elements (the ratio of the total bandwidth to the frequency resolution) [90],[92]. For the Bragg cells used in this research, the acoustic transit time is 10.0 μs, and the 3 db bandwidth is 100MHz, so the maximum number of resolution elements is about 1000 and the best channel resolution is about 100KHz. The higher resolution requirement prefers longer Bragg cell apertures, but this is hampered by the increased acoustic attenuation and the difficulty in impedance matching [42].

3.1.3 The Gaussian beam profile of illumination

The intensity profiles of most laser beams are Gaussian and can be controlled by adjusting the beam expander. The effect of this Gaussian beam profile of the illumination has been modelled by Hecht[42], using the concept of weighting function [54]. Basically, the superposition of the Gaussian profile on the finite aperture suppresses the sidelobes, although the resolution is slightly degraded [77], [41].

3.1.4 The acoustic attenuation in the Bragg cell

The effect of acoustic attenuation in the Bragg cell has also been modelled by Hecht[42], using the concept of weighting function [54]. Combining with the Gaussian beam profile of illumination, the acoustic attenuation causes an intrinsic exponential decay weighting, which modifies the acousto-optic index modulation, and thus causes a shift in the peak position of the Gaussian weighting function as well as a decrease in the peak amplitude. But there is no change in the shape or width of the Gaussian weighting function. Numerical calculations have been done by Hecht [42]. Typically, with a truncation ratio of 1, the 3 db lobe width would be widened by about 15% for an acoustic attenuation up to 12 db across the aperture. Thus, the resolution would also be degraded by about 15%. Most commercial Bragg cells have an acoustic attenuation much less than this, and thus the acoustic attenuation does not cause much degradation in the resolution.

3.1.5 The degradation of the resolution due to optical alignment errors

For the AOCS, misalignment of the Bragg cells can cause the different frequency components to be focused onto different positions and causes many undesirable effects. One of these effects is that the diffracted spots are tilted with respect to one another (Fig. 3-1), and thus the interference is spread across several frequency channels instead of just one channel. The resolution is thus degraded. The amount of resolution degradation depends on how well the alignment is made. Experimentally, a resolution degradation of less than 50% can be achieved with very simple alignment adjustments.

3.2 Radiometers

3.2.1 The radiometer equation

The sensitivity of a radiometer can be characterized by the following radiometer equation [31]:

$$\frac{\Delta T}{T_s} = \frac{1}{\sqrt{BT}}, \tag{3.1}$$

where T_s is the system temperature of the radiometer, B is the channel bandwidth, and T is the integration time. ΔT is the statistical detectable temperature change of the radiometer.

3.2.2 Effect of system gain fluctuation

When the system instabilities such as gain variations are taken into consideration, (3.1) becomes:

$$\frac{\Delta T}{T_s} = \sqrt{\frac{1}{BT} + (\frac{\Delta G}{G})^2}, \tag{3.2}$$

where $\frac{\Delta G}{G}$ is the fractional r. m. s. gain variation of the system. Such gain variation can easily dominate the sensitivity of a radiometer. For example, a 1% gain fluctuation would give a statistical fluctuation of $5^0 K$ when the system temperature is $500^0 K$. This would overwhelm a lot of signals.

3.2.3 Reducing the gain fluctuation by phase switching

Many schemes have been proposed to reduce this gain fluctuation [29],[73], [72],[83],[7]. The essence of all these schemes is the introduction of a reference noise signal into the system either by switching or adding. As a result, the sensitivity suffered.

For an interferometer system, phase-switching the two RF signals by 180^0 is a very powerful way to remove the gain fluctuation. Since it does not involve the introduc-

tion of a calibrated noise source into the signal, it does not cost any SNR degradation. This useful feature is implemented in the AOCS described in the previous chapter.

3.3 The AOCS as a radiometer

The AOCS can be used to measure the cross spectrum of two very weak RF signals, and hence is a kind of radiometer.

3.3.1 The black box model

To facilitate the discussion of the AOCS SNR degradation, one can model the AOCS as a black box (Fig. 3-2), such that the inputs to the black box are the outputs of the ideal radiometer, and the outputs of the black box are the actual radiometer outputs. That is, the inputs are s_i, the actual signal to be detected, and n_i, the system noise. The outputs are s_o, the estimated signal, and n_o, the degraded system noise. Both n_o and s_o may be degraded by various mechanisms.

3.3.2 Two major mechanisms of the AOCS SNR degradation

For the AOCS, the degradation in the SNR can be attributed to two major mechanisms. The first mechanism is the addition of noises by the AOCS to the system noise; i.e., $n_o > n_i$. This degradation for the AOCS is the same as for the single dish AOS. The second mechanism is the degradation of the actual signal; i.e., $s_o < s_i$. Physically, it is the degradation of the visibility of the correlated signal by various effects, such as the phase incoherence. This degradation has no analogue in the single dish AOS.

3.3.3 The definition of the radiometer SNR degradation

The degradation in the radiometer SNR ρ_r can be defined to be:

$$\rho_r = \frac{s_i/n_i}{s_o/n_o} - 1. \tag{3.3}$$

When there is no degradation, $\rho_r = 0$. When the output SNR is only half the input SNR, $\rho_r = 100\%$.

3.3.4 The definition of the AOCS sensitivity degradation

The radiometer sensitivity degradation usually refers to the degradation of the radiometer SNR because of the addition of noises. To avoid confusion, this meaning is always conformed to whenever this term is used in describing the AOCS sensitivity degradation.

From (3.1), one can define the input sensitivity S_{in} below:

$$S_{in} = \frac{\sigma_x}{\mu} = \frac{1}{\sqrt{B_n T}}, \tag{3.4}$$

where μ is the mean system noise power detected by one pixel of the detector, σ_x is the statistical fluctuation of the power detected by the detector, B_n is the noise equivalent bandwidth of one detector pixel, T is the integration time. S_{in} is the sensitivity of the ideal system (i.e., without any detector noise degradation). μ and all σ's are measured in units of number of photoelectrons detected by the detector.

Assume that the added noises (by the AOCS) are small compared to the system noise, so that the added noises do not change the mean system noise power μ; one can obtain the the sensitivity S_{out} at the output of the black box:

$$S_{out} = \frac{\sigma_z}{\mu}, \tag{3.5}$$

where μ is the same as above, and $\sigma_z^2 = \sigma_x^2 + \sigma_y^2$ is the total variance of the noise power detected (including the contribution by the black box noise σ_y^2).

The AOCS sensitivity degradation parameter ρ_s can be derived from the radiometer SNR degradation parameter ρ_r by keeping $s_i = s_o$:

$$\rho_s = \frac{n_o}{n_i} - 1 = \frac{S_{out}}{S_{in}} - 1 = \frac{\sigma_z}{\sigma_x} - 1. \tag{3.6}$$

3.3.5 The definition of the visibility degradation

As mentioned above, the second mechanism that degrades the AOCS SNR is the degradation of the measured signal. This degradation comes in the form of visibility loss of the correlated signal. The detailed mechanisms for the visibility loss will be discussed later in this chapter. The visibility loss contributes to the degradation in the AOCS SNR in the same way as the AOCS sensitivity degradation.

First the visibility V of a fringe is defined to be:

$$V =< \frac{I_{max} - I_{min}}{I_{max} + I_{min}} >, \tag{3.7}$$

where I_{max} and I_{min} are the maximum and minimun intensity of the fringe, and <> represents the ensemble average of the measurements. From this definition, one can measure the visibility loss.

Suppose some physical mechanisms cause a small change ΔI in the measurement of the intensity I, $\Delta I << I$; then the change in the measured visibility ΔV is approximately:

$$\Delta V =< \frac{2\Delta I}{I_{max} + I_{min}} > . \tag{3.8}$$

The fractional change in visibility is:

$$\frac{\Delta V}{V} =< \frac{2\Delta I}{I_{max} - I_{min}} > . \tag{3.9}$$

From (3.3), keeping $n_i = n_o$, one can see that the degradation in the AOCS SNR is the same as the fractional loss in the visibility of the correlated signal.

3.4 The SNR of the AOCS

3.4.1 The SNR of an ideal single multiplier correlation interferometer

The SNR of the ideal single multiplier correlation interferometer is given by the following expression [79],[80],[70]:

$$\frac{S}{N} = \frac{\sqrt{T_{a1}T_{a2}2BT}}{\sqrt{T_{s1}T_{s2}}}, \tag{3.10}$$

where T_{a1} and T_{a2} are the antenna temperatures of the signal, T_{s1} and T_{s2} are the system temperatures of the two antennas, B is the bandwidth, and T is the integration time.

3.4.2 The AOCS is a multiplying interferometer

The AOCS is a kind of complex spectrum multiplying correlation interferometer [19]. It differs from the single multiplier correlation interferometer only by the replication of more channels. Hence, the AOCS is a kind of multiplying interferometer, and its SNR is given by the same expression as above.

In Fig. 3-3 is shown a simplified representation of the AOCS. Let the system noise voltage going into the two Bragg cells be $N_{a1}(t)$ and $N_{a2}(t)$. $N_{a1}(t)$ and $N_{a2}(t)$ are uncorrelated, and correspond to system temperatures of T_{a1} and T_{a2}, respectively. Let the correlated signal voltage received by the antennas be $S_{a1}(t)$ and $S_{a2}(t)$. $N_{a1}(t)+S_{a1}(t)$ produce a power spectrum from Bragg cell 1, whereas $N_{a2}(t) + S_{a2}(t)$ produce a power spectrum from Bragg cell 2.

Since the different frequency components of the power spectrum are diffracted to different directions and do not interfere, it is necessary to consider only one frequency channel (as all the channels are equivalent). Let the Fourier components of this channel over a period of time T due to $N_{a1}(t)+S_{a1}(t)$ be $N_{a1}+S_{a1}$, and similarly, $N_{a2}(t)+S_{a2}(t)$ give $N_{a2}+S_{a2}$. Each Fourier component has both amplitude and phase. These Fourier

components interfere and give an interference pattern at the detector.

The intensity of the interference pattern at the center of the detector is:

$$I_0 = |N_{a1}+S_{a1}|^2+|N_{a2}+S_{a2}|^2+(N_{a1}+S_{a1})^*(N_{a2}+S_{a2})+(N_{a1}+S_{a1})(N_{a2}+S_{a2})^*. \quad (3.11)$$

The intensity of the interference pattern with respect to the angular coordinate θ can be represented by:

$$I(\theta) = |N_{a1} + S_{a1}|^2 + |N_{a2} + S_{a2}|^2 + 2|N_{a1} + S_{a1}||N_{a2} + S_{a2}| \cos(\frac{2\pi d \sin\theta}{\lambda} + \phi_0), \quad (3.12)$$

where θ is measured from the center of the two diffraction slits, d is the distance from the slits to the detector, λ is the wavelength of the illumination, and ϕ_0 is the phase difference between the signals $(N_{a1} + S_{a1})$ and $(N_{a1} + S_{a2})$. $|\ \ |$ denotes the absolute amplitude.

The first two terms are *constant biasing terms, and do not give any fringes.* The last term contains cross products of the signals and noises, and has the *same form as a single multiplier correlation spectrometer.* So, by measuring $I(0^0)$ and $I(180^0)$ and subtracting one from the other, the constant biasing term is removed while the cross terms double up. Hence, this shows that the AOCS is a multiplying interferometer. One also needs to measure $I(90^0)$ and $I(270^0)$ to obtain the quadrature component of the complex correlation. An equivalent representation is shown in Fig. 3-4.

3.4.3 The degradation of the system sensitivity by the detector noises

The degradation of the system sensitivity by the added detector noise for the single-channel acousto-optical spectrometer has been analyzed by a number of authors [61],[62], [50]. The physical origins of the photo-detector noise have also been thoroughly studied [8].

The detector noises can be classified into four main categories, namely, shot

noise, thermal noise (or fixed pattern noise), amplifier readout noise and quantization noise, the last being due to the A/D conversion of amplifier output into computer storage.

From (3.6) one can write

$$\rho_s = \frac{\sigma_z}{\sigma_x} - 1, \tag{3.13}$$

where σ_x^2 is the variance of the system noise power, $\sigma_z^2 = \sigma_x^2 + \sigma_y^2$ is the total variance of the noise power detected, and σ_y^2 is the variance of the detector noise added to the system. One can decompose σ_y^2 into $\sigma_{shot}^2 + \sigma_{therm}^2 + \sigma_{amp}^2 + \sigma_{quan}^2$.

To reduce the sensitivity degradation, one would like the detector shot noise to dominate over other noises, i.e., $\sigma_{therm}^2 + \sigma_{quan}^2 + \sigma_{amp}^2 << \sigma_{shot}^2$. The theoretical limit (best performance) is reached when the sensitivity degradation is dominated by the shot noise of the detector. This can be done by using detectors with a larger charge capacity. Assuming that this condition is satisfied, one can obtain a handy formula for the design purposes, using the relation $\mu = \sigma_{shot}^2$,

$$\begin{aligned} \rho_s &= \sqrt{1 + \frac{\sigma_y^2}{\sigma_x^2}} - 1 \\ &= \sqrt{1 + \frac{\sigma_{shot}^2 B_n T}{\mu^2}} - 1 \\ &= \sqrt{1 + \frac{B_n T}{\mu}} - 1 \end{aligned} \tag{3.14}$$

When the system time-bandwidth product $B_n T << \mu$, which is close to the charge capacity N of the photo-detector, one gets:

$$\rho_s = \frac{B_n T}{2N}. \tag{3.15}$$

This formula relates the time-bandwidth product of the system, the charge capacity of the photo-detector and the sensitivity degradation of the system. It is also known as the optical sampling theorem [63]. For example, if $B_n = 1$ MHz, $T = 0.1$ sec, and N = 10^6, then $\rho_s = 5\%$.

For most photo-detectors at room temperature, σ^2_{therm} and σ^2_{amp} are usually smaller than σ^2_{shot}, provided that the detector is operated near saturation level. The resolution of the A/D converter can be chosen by demanding that $\sigma^2_{quan} = \frac{q^2}{12} << \sigma^2_{shot} = \mu$. q is the quantization step width in units of number of electrons of the photo-detector. For example, if N = 10^6, then a 10-bit A/D converter would make σ^2_{quan} less than 10% of σ^2_{shot}.

Although the above derivations are for the single dish acousto-optical spectrometer, the results can be directly applied to the AOCS, since the quadrature components (or the fringe) of the correlation are obtained by some linear combinations of the pixel readouts as described in the beginning of this section.

3.4.4 The degradation of the signal visibility due to fringe smearing

The finite size of the detector caused the smearing of the fringe amplitude and a degradation of the signal visibility [61]. The net effect is to decrease the fringe visibility by a factor $sinc(\frac{yD}{\lambda z})$. The derivation is shown below.

For simplicity let the fringe intensity be represented by:

$$I(x) = I_0 cos(\frac{2\pi x D}{\lambda z} - \phi_0), \tag{3.16}$$

where I_0 is the maximum intensity of the fringe, x is the coordinate of the fringe axis, D is the separation between the slits, z is the focusing distance for the fringe, and ϕ_0 is the arbitrary phase shift.

The fringe intensity measured by a detector of width y is:

$$\begin{aligned} I(x_0, y) &= \int_{x_0-\frac{y}{2}}^{x_0+\frac{y}{2}} I_0 \cos(\frac{2\pi x D}{\lambda z} - \phi_0) dx \\ &= I_0 \cos(\frac{2\pi x_0 D}{\lambda z} - \phi_0) sinc(\frac{yD}{\lambda z}). \end{aligned} \tag{3.17}$$

So the effect of the finite aperture size of the detector is to decrease the fringe

visibility by $sinc(\frac{yD}{\lambda z})$. As an example, if $\frac{y}{\Delta x D} = \frac{1}{6}$, then $sinc(\frac{yD}{\lambda z}) = 0.95$, since $\frac{\lambda z}{D} = \Delta x D$.

Hence, there should be at least 6 detector pixels per fringe if the smearing effect is not to degrade the signal visibility by more than 5% [61].

3.4.5 The degradation of the signal visibility due to mechanical instability

Mechanical instabilities are difficult to characterize and predict. Transient vibrations would likely cause the fringe phase to fluctuate, thus either temporarily destroying the fringes or degrading the signal visibility. More permanent mechanical movements or deformations may cause misalignment in both the frequency and the fringe dimension, thus degrading the system resolution, changing the frequency scale or the setting of the fringe separation. If the measurements are not corrected for the change in the fringe separation, the fringe visibility (computed from four pixel measurements) would be further degraded.

3.4.6 The degradation of the signal visibility by optical surface irregularities

In this section, the effect of the surface roughness of the optical components traversed by the laser beams is considered. The surface roughness causes the incoming coherent laser beam to be scattered and depolarized [1]. The depolarization effect can often be ignored for highly smooth surfaces compared to the random scattering loss.

In Appendix D, Chandley's work [16], [17] for the coherent loss of a single optical surface is extended to an interferometric system. The ensemble average of the intensity due to two distinct but highly coherent (both spatially and temporally) apertures in the Fraunhofer region is calculated by assuming that surface roughness causes only a phase front variation of the incoming laser beam. To first order, the surface roughness causes a reduction of the total illumination by a factor of $e^{-\sigma_\phi^2}$ [82], where σ_ϕ^2 denotes the r. m. s. phase variation of the laser beam due to the optical surface roughness. Hence,

the visibility is also reduced by the same factor (upper bound). Although the r. m. s. surface roughness of laser quality optics is about $< \frac{\lambda}{200}$, which gives a visibility loss of less than 1%, the surface accuracy is usually less than $\lambda/20$ and hence the visibility loss may be as high as 10% per surface.

The formulation in Appendix D allows other physical effects to be treated in the same manner; i. e., from the physical effect one computes the equivalent r. m. s. phase variation, and the visibility degradation is then computed from the autocorrelation function of the phase variation.

3.4.7 The degradation of the signal visibility by air turbulence

In this section, the effect of air turbulence that affects the coherence of the laser beam is considered. The effect of the air turbulence is to introduce a phase fluctuation in the propagating plane wave front, and thus causing a degradation in the coherence.

The theory for propagation of a plane wave through a random weakly fluctuating medium has been well developed [87], [88], [55],[43]. In this section, the formulation by Ishimaru [43] is used with the results derived in Appendix D to compute the effect of air turbulence on the interferometer. The basic assumption is that the turbulence is homogeneous and locally homogeneous [43] and that the Fresnel zone size $(\lambda L)^{\frac{1}{2}}$ is very much smaller than the correlation distance l_0 of the turbulence. This means that the geometric optic approximation is valid, and that the log amplitude fluctuation is unimportant compared with the phase fluctuation. This assumption is justified because of the scale size of the turbulence $L < 1m$ (being restricted by the optical path of the system), so $\lambda L < 6.328 \times 10^{-7} m^2 < l_0^2$. ($l_0$ has a typical value from 1mm to 1 cm). From Ishimaru [43], one has:

$$\sigma_s^2 = 0.7817 C n^2 k^2 L L_0^{\frac{5}{3}}, \tag{3.18}$$

where σ_s^2 denotes the r. m. s. phase fluctuation, C_n is the structure constant of the index of refraction fluctuation typically from $10^{-9}m^{-\frac{1}{3}}$ to $10^{-7}m^{-\frac{1}{3}}$ [43], k is the usual wave constant, L is the distance of the scattering medium to the observer, L_0 is the outer scale of turbulence (the size at which energy enters into the turbulence). L_0 may be as large as 10m in open ground.

Assuming L_0 to be 10m, L to be 1m, σ_s varies from 3.4^0 (weak turbulence) to 342.8^0 (strong turbulence) at 633 nm. The figure is obviously unacceptable for strong turbulence. Fortunately, in the confined laboratory conditions where the instrument is placed, the outer scale of turbulence can never be as large as 10m. A reasonable guess for it is 1m. With some confinement it can be made to be 0.2m. If L_0 is 0.2m instead of 10m, σ_s varies only from 0.13^0 to 13.2^0. This figure is good enough for the instrument since the r. m. s. phase fluctuation due to the optical surface roughness is about 1^0 [71]. The degradation in signal visibility due to air turbulence can be treated in the same way as in the previous section and is not repeated.

3.4.8 The degradation of the signal visibility by the misalignments of the optical system

Misalignments cause losses in the visibility. When the two beams are not parallel, some of the correlated signal is wasted and so the visibility is degraded. It is difficult to characterize the visibility loss due to misalignment. In practice, one would try to align the optical system as best as one can. The visibility loss can be measured according to the formula in Section 3. 3, and was found to be the major loss mechanism of the prototype instrument.

3.4.9 The atmospheric effects

In the previous section, only the effect of the air turbulence was treated. In fact, there are also other effects due to the atmospheric conditions that may affect the signal visibility. In general, there are the absorption and the scattering due to the aerosol and molecules present in the air [60]. Since the optical path traversed by the laser beams is very small (about 1m), these atmospheric effects are not very important compared to the other effects. The Rayleigh volume scattering coefficient for standard air at $0.63\mu m$ is $7.05710^{-6}m^{-1}$ [75], and hence the effects due to the aerosol and molecules are indeed negligible.

3.5 The RF Power and the illumination requirements

The laser illumination ϕ is related to the optical efficiency of the system η and the Bragg cell RF drive power P by the following formula:

$$\phi = \frac{A\sigma}{T\eta P B_\eta}, \tag{3.19}$$

where A is the effective area of illumination, σ is the detector sensitivity (i.e. the optical power required to saturate the device, in units of $\mu J/cm^2$), T is the integration time, and B_η the diffraction efficiency of the Bragg cell (% per Watt).

In order to find out how much laser power the system requires, and how much RF power is needed to drive the Bragg cells, one must do the following efficiency analysis.

3.5.1 Optical Losses

All the factors that lead to any optical loss of the system are itemized below:

1. The polarization loss — The laser is unpolarized. Both polarizations have similar losses in all the factors below except for the prism beam expander. The S-polarization has a larger loss compared to the P-polarization [44]. So it is preferable

to use a polarized laser and adjust the beam to be P-polarized with respect to the prism beam expander. The relative transmission and reflection with respect to the incident angle for both polarizations are shown in Fig. 3-5.

2. The beam expander loss — From Fig. 3-5 one can find out the loss for each polarization per prism beam expander stage. Experimentally, one can assume a 40% overall efficiency for the two stage prism expander [66]. If we apply anti-reflective coating on each surface, an efficiency of 60% may be achieved.

3. The beam splitting — One can assume that the beam is equally split without any loss except for the few percent of loss due to internal reflection (ghost images).

4. The transmission loss of every optical component — Assume each cylindrical lens transmits 90% of the incoming light; then we have 66% of incoming light left after passing 4 cylindrical alignment lenses (with good anti-reflective coating, we may achieve 96% transmission per lens). The mirrors are 96% reflective and so the loss per reflection is 4%.

5. The spatial filter loss — The slit width of the spatial filters is about 0.1mm, so only about 20% of the light passes through the filters.

From the above considerations, it is safe to assume that about 2.5% of the light passes through the system.

3.5.2 The Bragg cell efficiency

Assuming an input RF power of 0.1W and the diffraction efficiency of the Bragg cell to be 10%/W RF (peak), then 1% of the input power would be diffracted into the detector. The RF power can be raised to a maximum of 3W (continuous rating) to improve the diffraction efficiency.

3.5.3 The detector efficiency

The quantum efficiency of the CCD chip is around 60% and its sensitivity is about $0.07\mu J/cm^2$.

3.5.4 The fringe diffraction pattern

Assume that light falls uniformly within the main diffraction lobe, which is about 3 fringes wide, with each fringe covering about 128 pixels (the actual intensity distribution is a $sinc^2$ function and 90% of the illumination falls within the main diffraction lobe). So the effective area illuminated by the laser beam is about 3 x (128 x $16\mu m$) x (403 x $20\mu m$).

3.5.5 The illumination requirement

If the device is to achieve full saturation within one frame time (say 100ms), then we need an input illumination ϕ of:

$$\begin{aligned} \phi &= \frac{A0.07\mu J/cm^2}{100ms(1\%2.5\%)} \\ &= 1.5mW. \end{aligned} \tag{3.20}$$

Hence, the illumination is adequate with a 2mW laser with the RF drive power at 0.1W.

3.6 The data rate

From the fundamental Equation (3.15), one can specify the integration time (or frame time) from the other system parameters. The smaller the system frame time, the lower will be the detector noise degradation to the SNR. However, the frame time cannot be arbitrarily assigned to any value. The reason is that the system needs to do a lot of computation for every frame readout. So, the frame time has a lower limit imposed by the speed of the backend computer.

The task that the computer has to do absolutely for every frame readout is to integrate the data. If corrections for the AOCS gain and phase fluctuation are desired by injecting a reference signal, the correction also has to be done within this frame time. Other corrections such as the corrections for the pixel gain variation and the diffraction pattern of illumination can be done after the integration has been completed and recorded into disk files.

For the present system, a frame time of 0.1 sec has been achieved by writing critical portions of the data processing in assembly language. A frame time of 50 msec is achievable with a faster machine like the IBM PC/AT.

Chapter 4

The performance measurement of the AOCS

In Chapter 2 the hardware operation of the instrument was described, and in Chapter 3, a theoretical analysis of the instrument was presented. In this chapter, the actual performance of the instrument that was measured is presented and compared with its theoretical predictions. An absolute calibration of the instrument was attempted by using the system temperature as the scale for both the correlated signal received and the noise fluctuation of the instrument. A statistical method was used to characterize the noise fluctuation so that the noise contribution from various parts of the instrument can be compared with the theoretical system noise fluctuation. The visibility loss was measured to be about 50%. The noise degradation of the AOCS was about 40%. These losses were not due to any theoretical limitations but were the results of the imperfections in the present setup of the instrument. They can be improved in the future versions of this instrument.

4.1 The absolute flux calibration of the AOCS

For a multiplying interferometer, the absolute flux measurement is difficult because of the various unknowns in the system gain. Practically, one always uses a strong astronomical source (such as Uranus) as a reference for the flux calibration. For the AOCS, there is a natural way to do the absolute flux calibration because the AOCS output has a D. C. level. The idea is to make use of the system temperature as a scale

for the correlated flux and the noise fluctuations. Consider only uncorrelated noises in the system. From Equation (3.12) one can see that the D. C. level of the output is proportional to the sum of the uncorrelated noise power of the two channels, and hence, is proportional to the system temperature. Thus, the equivalent temperature of the correlated flux and the noise fluctuations can be found from this scale.

One can also notice that such a scale can be established with many radiometers such as the adding interferometers, which have a D. C. level. The D. C. level of the radiometer output is usually proportional to the system temperature in some way. With such a scaling, the absolute flux of the astronomical sources can be measured directly.

4.2 The gain non-uniformity calibration of the AOCS

The gain non-uniformity calibration refers to *the correction of the various static or slowly changing systematic variations* of the output. In this section, the various effects that cause such systematic variations are listed, including the pixel gain variation of the CCD, the diffraction pattern due to the finite width of the slits, the Bragg cell response non-uniformity, the Gaussian profile of the laser beam, and the zero level variation of the CCD. All of these factors contribute to the static systematic variation of the detector pixel output, and must be corrected. All these effects can be corrected in one single calibration by giving every individual detector pixel a different gain correction factor.

4.2.1 The pixel gain variation of the CCD

The CCD detector pixels are not exactly the same. Each pixel has a slightly different photo-electron conversion gain because of the differences in the device geometry and the material homogeneity, and so the same amount of light falling onto different pixels yields a different number of electrons.

For CCD detectors, the photo gain non-uniformity is very small. Typically, it is less than 0.5% throughout the array. With a phase-switching scheme, the correction for the photo-gain non-uniformity is unnecessary. Individual pixel gain variations with time due to device aging etc. are also very small compared to the other effects such as the variations in the diffraction pattern due to the mechanical changes.

4.2.2 The diffraction pattern of the slits

Because of the finite width of the slits (about $100\mu m$), the amplitudes of the fringes that formed from the interference of the two slits are modulated by a sinc function (Appendix C). So, after the measurement has been taken, one must correct for the pixel intensity variation of the diffraction pattern. This effect is much larger than the pixel gain non-uniformity above and must be corrected. The differences in the slit widths (or the intensity of the diffracted beams) may cause an extra biased level and a loss of fringe visibility at the detector if not corrected.

4.2.3 The Bragg cell response non-uniformity

Another effect that causes the pixel intensity variation is the non-uniform frequency response of the Bragg cells. The Bragg cell efficiency is peaked at 150MHz, dropping by 3db towards the edges (100MHz and 200MHz). Hence, the amount of light that falls on the central frequency channels is larger than that on the edge channels, and the signal-to-noise ratio is also better for the central frequency channels.

4.2.4 The beam expander non-uniformity

The laser beam has a Gaussian profile, and when expanded, has a fairly large intensity variation across the profile. After several reflections and beam splittings, the

beams may have some non-uniformity and will lead to slightly different diffraction patterns.

4.2.5 The zero level of the CCD and its determination

For the same reasons as the pixel gain non-uniformity, the dark levels of the CCD pixels also vary. This fixed pattern noise can be measured and removed from every measurement. It can be determined by integrating for some time with the RF signal off.

4.2.6 The determination of the pixel gain correction

With only uncorrelated noises going into the Bragg cells (or pointing the antennas to the sky), the AOCS is allowed to integrate for some time. The zero level is then subtracted from the average signal of each pixel. The pixel measurements are then inverted and normalized so that the pixel reading of the strongest signal is normalized to 1. A smoothing operation (say averaging the 20 nearby frequency pixels for every individual pixel) is then applied. If the gain is very large (say > 3), then the gain is set to 0 to mask out the pixel. This usually occurs near the edge of the frequency channels where the illumination is weak. A typical set of pixel gain corrections is shown in Fig. 4 - 1. The calibration requires that the system IF level be relatively stable, and that the correlated noise have the same IF characteristics as the uncorrelated noise. If they are different, then the correlated noise should be used for pixel gain calibration.

4.3 The stability of the instrument

All the above static effects that cause the pixel gains to vary can be calibrated away. However, there are many other dynamical effects that cannot be tackled easily. They can be classified either as electronic instability or as mechanical instability.

4.3.1 The electronic instability

The system zero level variation

The electronic instability causes the drifting of the zero level of the system. This drifting is unpredictable and hampers the measurement much more seriously than the various static non-uniformities [63]. From some preliminary measurements, the drifting could be an order of magnitude larger than the theoretical noise fluctuation of the system with a fixed input. Besides the CCD zero level variation, the whole system, especially the front end receivers and the RF amplifiers, also has gain fluctuations that could cause the zero level to change, and must be properly dealt with before any accurate measurement can be taken.

The stabilization of the zero level by phase switching

By incorporating a phase-switching scheme, the drifting of the zero level can be significantly reduced. Phase switching is a very powerful technique in interferoradiometric measurements. By alternating the radio signals received from one of the two antennas by a phase of 180^0 and correspondingly adding or subtracting the correlated signal during integration, many long-term drifts and systematic errors can be eliminated [86],[91].

For our millimeter interferometer array, there are three antenna dishes, and the implementation of the phase switching is more complicated than a two-element interferometer. As we have discussed, there are two phase-switching schemes implemented. The fast phase-switching switches into two phases at a rate of 100Hz, 50Hz and 50Hz respectively, aims at removing the zero level. The slow phase switches into four phases at a rate of 5Hz, 2.5Hz and 2.5Hz. Besides removing the zero level, the slow phase switching is also used to separate the upper and lower side bands by going through a four phase

cycle.

As was shown in Chapter 3, the frame time of the AOCS was chosen to be 0.1 sec, so the fast phase switching cannot be used. The slow phase switching rate was set to either 2.5Hz or 5Hz, depending on the baseline used.

Even with only the slow phase-switching scheme implemented, the zero level has been greatly stabilized. The typical zero level (with only uncorrelated noise input) after half a minute of phase switched integration is shown in Fig. 4-2.

The ratio of the r. m. s. fluctuation to the D.C. level is about 40% higher than the theoretical $1/\sqrt{2B.T}$ value. The r. m. s. fluctuation versus time also agrees well with this relation. The technique of the measurement is presented later in this chapter. Also seen occasionally in some data sets are some very large spikes (4σ), which could be the result of the following:

1. Coupling between the video amplifier and the system synchronization circuit, especially through the 60Hz generated by the phase-locked loop.

2. RF coupling through the correlated noise source.

3. Transients in the RF amplifiers or in the noise generator.

4. Scattered laser light.

4.3.2 The mechanical instability

The mechanical instability affects the alignment of the optical system, and thus, affects the resolution, the setting of the frequency scale and the fringe separation. Transient instability causes only a temporary loss of signal coherence (or visibility), while permanent changes cause the mechanical settings to change, and recalibration may be needed.

A lot of effort has been put into stabilizing the system mechanically, such as the vibration isolation scheme of the optical table support and the removal of unstable optical components from the system. When the system was left running without disturbances, it was found that the fringe phases were visually stable to a fraction of a radian (up to hours). However, when the optical table is disturbed, there may be large permanent phase shifts. For continuous operations, it might be necessary to calibrate the fringe phase of the instrument frequently to correct for any unexpected phase shift due to any mechanical instability.

4.4 Data processing

4.4.1 Data processing tasks

As has been explained in the previous chapters, the CCD frame time was set to 0.1 sec. That is to say, the computer has to grab one frame of CCD data every 0.1 sec and process it before the next frame begins. Obviously, one would put all non-essential processing steps at the end of the integration cycle. So, one has to distinguish the real time tasks from the non-real time tasks. There are several processing steps that need to be done on the raw data.

1. Integration - the data are accumulated onto some buffer area.
2. Zero level correction - the zero level is removed from the raw data.
3. Pixel gain correction - the data are normalized by scaling the net pixel readout with its gain correction.

Of the above processing steps, only the integration is needed to be done for every frame. The other two steps can be applied once per integration cycle or delayed until the fringe amplitudes and phases are computed.

The other non-real time processing tasks provided are:

1. Fringe amplitude and phase calculation — with four pixel readouts per fringe line (90^0 apart on the fringe axis), the fringe amplitude and phase can be computed after the correction for the zero level and the gain non-uniformity.

2. Side bands separation — if the signal is a double side band signal and a four-phase switching is applied synchronously at the front end local oscillator and at the integrating buffers, the side bands can be separated. The algorithm is listed in Appendix E.

3. Phase correction — there is a linear phase shift across the frequency channels due to the different optical paths traversed by the different frequency components on the arms of the interferometer. A very small quadratic phase shift across the frequency channels was also observed. The origin of this quadratic phase shift is due to the compression of the frequency scale. This could be due to the misalignment of the optical system or the aberration of the focusing lenses.

4. Fringe separation correction — if the fringe is not measured at 0^0, 90^0, 180^0 and 270^0 because of alignment, the fringe amplitude and phase can still be estimated very accurately, provided one knows the separation between each measurement. Let the four pixels measure $I_0 = A\cos(\phi_A - \phi_X)$, $I_1 = A\cos(\phi_A)$, $I_2 = A\cos(\phi_A + \phi_X)$, and $I_3 = A\cos(\phi_A + 2\phi_X)$, respectively. A is the amplitude to be measured, ϕ_A is its phase, and ϕ_X is a known phase shift approximately equal to 90^0. By simple algebra, one can obtain

$$\begin{aligned} A\sin\phi_A &= \frac{I_0 - I_2}{2\sin\phi_X} \\ A\sin\phi_A &= \frac{1}{2\sin^2\phi_X}[I_1 - I_3 - (I_0 - I_2)\cos\phi_X]. \end{aligned}$$

5. Tilt correction — if the CCD camera is tilted by more than a few pixels with respect to the fringe axis, then the fringe can be corrected by offseting the pixels of each fringe column. If the tilt is less than about 2 pixels across the fringe axis, the correction is ineffective.

All the above tasks can be performed interactively by the user.

4.4.2 The data collection algorithm

For every CCD frame readout, the raw data are stored in a buffer area (the data hold area) and accumulated onto another buffer area (the data integrating area). There are three different cases:

1. No phase switching — the CCD output frames are accumulated in one single buffer area. After the integration is completed, the zero level is subtracted to obtain the actual signal.

2. Two-phase switching — the CCD output frames are added and subtracted alternately in one single buffer area synchronously with the phase switching. The zero level is automatically removed.

3. Four-phase switching — the CCD output frames are accumulated in two buffer areas. The 0^0 phase and the 180^0 phase are treated as a pair and are accumulated in one buffer area. The 90^0 phase and the 270^0 phase are treated as another pair and are accumulated in the other buffer area. Additions and subtractions are synchronous with the phase signal.

Compared to the two-phase switching case, the four-phase switching has this advantage, that double side band signals can be separated without any reduction in SNR

[89]. The disadvantage is that the phase cycle is twice as long and the zero level is not as stable.

4.4.3 The fringe pattern

The observed fringe pattern is shown in Fig. 4-3. Notice the constant increment of the fringe phase because of the different optical path lengths traversed by the different frequency components. This is an undesirable effect, since the sausage pattern may show up in the resultant fringe amplitudes of the frequency channels. It can be corrected by putting in an appropriate phase correcter either in the RF signal or in the optical path.

4.5 The performance measurements

In this section, the techniques used to measure the system performance, namely, the noise degradation and the signal visibility loss, are outlined, and the measurements are presented. The unit of measurement is one step of the A/D converter output level.

4.5.1 The noise generator design

To measure the system performance, one can simulate the actual environment, using a combination of correlated and uncorrelated noises. The circuit is shown in Fig. 4 - 4. The uncorrelated noises simulate the system noises of the radio telescopes, and the correlated noises simulate the signals arriving at the radio antennas from the radio source.

The uncorrelated noises are generated by two RF amplifiers with the inputs terminated to 50 ohms. The amplifier outputs are measured and are found to have an equivalent noise temperature of about $300,000^0 K$. The frequency characteristics of these uncorrelated noise sources are less than satisfactory. In Fig. 4-5 is shown the single-channel noise. The average is about 90 units. In Fig. 4-6 is shown the two-channel noise.

The average is about 180 units, verifying that the uncorrelated power simply adds up. It can be seen that the frequency responses are not very uniform.

The correlated noise is obtained by splitting the output of a noise generator into two. The correlated noise has an equivalent noise temperature of $6500^0 K$ from each output. In this setting, the uncorrelated noise power to the correlated noise power is approximately 16.5db. The uncorrelated noises and the correlated noises are combined and amplified together to drive the Bragg cells. To conserve the amplifier powers and to avoid saturation, the signals are lowpass- filtered before they are amplified at the second stage. There is also a variable attenuator on one path of the RF driver to compensate for any gain mismatch of the two Bragg cells.

In order to simulate the tests in a phase-switching environment, a phase switch composed of an RF switch and a 180^0 power splitter is made. The RF switch is controlled by the system 10Hz signal. Since the 180^0 power splitter was not available, a 0^0 power splitter was used, and a cable (approximately 0.6m long) was put on one arm to create a 180^0 phase shift at 150MHz. This is perfectly all right for the noise measurements and the CW measurement. When a correlated noise was used, the fringe visibility rolled off from the center frequency.

4.5.2 The statistical noise measurement

There are two kinds of statistics. First is the statistics on various integrated samples (the time average) of the same pixel. Second is the ensemble statistics of all pixels on one frame or averages of many frames. The first kind of statistics is important for characterizing the dynamic behavior of the system, namely, the zero level variations of the pixels, the gain variations of the pixels, and the stability of the system. The second kind of statistics is useful for characterizing the uniformity of the pixels, and for defining the system sensitivity.

4.5.3 The method of measurement

About 300 frames of data (30 sec integration time) are collected and individual pixel statistics (first kind) are calculated. The ensemble average of the r. m. s. fluctuations of the pixel readouts gives a characterization of the noise level of the measurement. The r. m. s. ensemble fluctuation of the r. m. s. pixel fluctuation shows the uniformity of the pixel noise performance. The measurement is repeated a few times to ensure accuracy. All the r. m. s. fluctuations described here refer to the the r. m. s. ensemble fluctuation of the r. m. s. pixel fluctuations.

4.5.4 The A/D converter noise measurement

The A/D converter, being a sample, was found to be defective and did not work well when the input voltage was outside $\pm 0.3V$ (the full-scale input range of the A/D converter being $\pm 5V$). The test was done by injecting triangular waves into the converter. Because of this, the converter was effectively an 8-bit converter and care had been taken to ensure that the input signal was within the working range of the converter. To increase the dynamic range of the A/D converter, the zero level was biased at an offset beyond the normal working range and was found to work well.

By running the phase-switching algorithm with the video input to the computer connected to a D. C. power supply for about 30 sec, the video amplifier noise and the A/D conversion quantization noise can be measured. The r. m. s. pixel fluctuation was measured to be about 60% of the theoretical system noise fluctuation.

4.5.5 The detector noise measurement

1. The CCD readout noise and the dark noise can be measured by setting up the instrument in the same way as was intended for the real measurement, except that

the optical path of the laser beam is blocked by covering up the CCD detector. The measurement includes the noises due to the A/D quantization, the video amplication, and the detector dark level and the read-out process. By comparing this measurement with that above, one can find the detector noise performance. The r. m. s. pixel fluctuation (A/D C + CCD zero level) was measured to be about 65% of the theoretical system noise fluctuation. A typical spectrum is shown in Fig. 4 - 8.

2. The above test can be repeated with the laser on, but the RF off. By comparing the measured r. m. s. pixel fluctuation with that of the above, the contribution due to the scattered light can be calculated. The r. m. s. pixel fluctuation was about the same as above, indicating that scattered light does not contribute much to the noise degradation.

3. The detector shot noise can be measured in the same way as above, except that the optical path is no longer blocked and the CCD camera is illuminated by uniform white light. The r. m. s. pixel fluctuation is about 95% of the theoretical system (RF) noise fluctuation.

4. The overall noise (including the system noise) was measured in the same way as above, with the Bragg cells driven by uncorrelated noises. The scale of the system noise fluctuation was decided by the level of the system noise, which was about 560 units for one channel for the present setup. If the system noise level was scaled up (say by an A/D converter with a larger dynamic range), then the system noise fluctuation would also go up until it dominated. Because of the low dynamic range of the A/D converter, the system noise contributed only half of the total noise, so the sensitivity degradation ρ_s was about 40%. The r. m. s. pixel fluctuation was about 110 units in this scale.

From these measurements, it is seen that the noise performance of the system (i.e., the ratio of the r. m. s. pixel fluctuation to the D.C. level), with only uncorrelated noise input, roughly follows the theoretical $1/\sqrt{2B.T}$ value. The system noise contributes about 1/2 of the total noise (noise output of the black box) and the system sensitivity degradation is not shot-noise dominated.

It was also found that there were some noises coupled with the 60Hz cycle, which showed up in the 2ϕ switching integration but not in the 4ϕ switching integration even with the laser turned off. Since a 4ϕ switching integration is used in the actual observation, this coupling did not cause a very serious problem. They probably came from the prototype card since the A/D converter, the video amplifier and the camera phase-locked loop were all present, and there may be couplings between them.

4.5.6 Pure CW signal and the resolution measurement

To measure the frequency resolution, one simply injects a CW signal into the Bragg cells. With the optical path of one channel blocked, the frequency resolution is better than 1 channel. That is to say, the 3 db power width is less than one channel wide (Fig. 4-7). When both optical paths are unblocked, the beams interfere. Because of some misalignment, the frequency resolution of the fringe is about 2 channels wide (Fig. 4-8).

4.5.7 The limit of signal sensitivity

In principle, the limit of signal detection should be about 3σ of the r. m. s. noise fluctuation, which scales with $1/\sqrt{2B.T}$. However, when both the input signal and the r. m. s. system noise fluctuations are less than 1 unit of the A/D converter, the system sensitivity will be greatly degraded. This situation will occur when the dynamic range of the A/D converter is small.

The reason for this is that under such conditions, the system is not shot-noise

dominated, and the A/D converter sets a limit on the detection threshold. This is not the same as the quantization noise of the A/D converter, which will go down as $1/\sqrt{2B.T}$. In this situation, the A/D converter is simply insensitive to level changes smaller than 1 unit. It is either always a '1' or always an '0'. Of course, some random level fluctuations would randomize this '1' or '0' situation and rescues a small portion of the signal. Nevertheless, the signal is greatly degraded.

The situation is different if the system noise fluctuation is much greater than 1 unit. In such situations, the signal, even though small, would add a bias to the noise fluctuation, and the A/D converter, which is sensitive to the noise fluctuation since it is above 1 unit, would also be biased to a higher average value.

This has been observed at the first astronomical test of the instrument with a very low dynamic range. By biasing the zero level of the video input, a higher dynamic range (about 10 bits) has been obtained and this problem was fixed.

In Fig. 4-9 is shown a CW signal that is -6db that of Fig. 4-8. The figures shown are the net-integrated outputs without any correction. Both have been integrated for 30 sec. The signal is on the verge of the detection threshold. In Fig. 4-10 is shown a CW signal that is - 12db that of Fig. 4-8 integrated for two minutes. The signal, although still seen, is only about half of what it should be.

4.5.8 The visibility loss measurement

The correlated noise tests were done to measure the visibility loss of the AOCS by the various factors discussed in Chapter 3. Only correlated noises were put into the system. Two different tests had been attempted.

Integration without phase switching

Correlated noises are injected into the Bragg cells and integrated without phase switching for two minutes. The zero level is then removed (Fig.4-11). The visibility loss can be measured using the definition in Section 3. 2. This measurement suffered from the zero level variation and the RF channel mismatch, since they obscured the determination of I_{max} and I_{min}. The visibility loss is about 50%.

Integration with phase switching

This measurement is an indirect measurement of the visibility loss by computing the fringe amplitude from the power of the correlated noise source and compares with the measured fringe amplitude. This method does not suffer from the zero level variation and the RF channel mismatch above. Correlated noises are injected into the Bragg cells and integrated with phase switching. In Fig. 4-12 is shown one column of the corrected data versus the frequency axis. The sausage pattern was due to the phase shift explained in Section 4. 2. The roll off in amplitude from the center is due to the inexact phase switching at frequencies other than the central one because of the cable.

The fringe amplitude measured was about 3 units. Since the two channels are balanced, it corresponds to approximately $2T_a$, where T_a is the temperature due to one single channel of the correlated noise generator. So, $T_a/T_s = 1/60$. From the power measurement, $T_a/T_s = -17\text{db} = 1/50$, and so the visibility loss measured by this method is about 20% and is considerably smaller than that measured above. However, this measurement suffered from the fact that the uncorrelated noise sources do not have a flat frequency response, and differed from the frequency characteristics of the correlated noise source. Hence, the visibility loss calculated from this measurement is not as accurate as the above test. A more precise measurement should use the same correlated noise

source for generating the uncorrelated noise power, which serves as a scale for the system temperature.

4.5.9 CW in the presence of uncorrelated noises

In Fig. 4-13 is shown the result when a CW signal is mixed with the uncorrelated sources. The correlated signal is the same as without the uncorrelated noise. The background is due to the channel mismatch of the phase switch. In Fig. 4-14 is shown the result with only the phase-switched channel on (with uncorrelated noise). The phase switching measures the difference of the frequency response and the self coupling of the phase switch inadvertently. Interestingly, this may provide a novel way of calibrating two very closely matched microwave devices. The two devices can be put on the two arms of a "good" phase switch. By phase switching and integrating, the mismatch of the device can be obtained to an accuracy $\frac{T_n}{\sqrt{BT}}$. The phase mismatch of the two devices can be measured similarly, with the other channel turned on as a reference.

4.5.10 Astronomical measurement

The instrument was used in test observations with the millimeter interferometer at Owens Valley Radio Observatory. The moon was observed for three minutes, and continuum fringes were seen (Fig. 4-15 - 4-22). The IF bandwidth of the system is from 40MHz to 120MHz, while the Bragg cell has a bandwidth from 100MHz to 200MHz. So, only the mid channels (from channel 30 to 130) have a good signal input.

The I and Q component of the first buffer is shown in Fig. 4-15 and 4-16. They showed similar fringes, shifted by 90^0 with respect to one another. The I and Q component of the second buffer is shown in Fig. 4-17 and 4-18. No fringes were seen because the upper side band and the lower side band shifted by 90^0 in opposite directions and they canceled out one another. The fringe amplitudes and phases are shown from

Fig.4-19 to 4-22. The phase has been corrected for the linear phase shift and the second order non-linearity.

The absolute continuum flux measured was about a factor of three less than what it should be, a factor of two came from the visibility loss of the optical system described above, and the rest could be due to the following reasons:

1. RF mismatch - varies from 10% for frequency channels at the center to 50% for channels near the edge.

2. Antenna efficiency change - the AOCS measurements were in units of the system temperature, whereas the actual flux received is converted to the antenna temperature by assuming a certain antenna efficiency. The antenna efficiency may vary by 20% depending on the test condition.

3. Accuracy of the system temperature measurement - since everything is scaled according to the system temperature, any inaccuracy would cause the measured flux to be scaled in the wrong way.

4. Mixing of the side bands - since the interferometer was a double side band one, the fringes of the upper side band and the lower side band were mixed up, and any phase difference between the two side band components would cause a visibility loss. This could give 10% of the visibility loss.

5. Phase stability - any phase instability in the optical system would cause fringe decorrelations unrecorded by the system, and this could give 10% of the visibility loss.

These measurements demonstrated that the instrument actually worked and is stable enough mechanically and electronically for astronomical measurements. It is just a matter of putting in more effort to make the instrument work better.

Chapter 5

Conclusion

5.1 What does this research demonstrate?

In this research, a prototype acousto-optical correlation spectrometer has been built. It has 241 frequency channels, with a channel resolution of 300 KHz. Both the frequency coverage and the resolution of this spectrometer can be easily changed. The hardware cost of this instrument is less than $20,000, which is only a fraction of the cost of a filter bank correlation spectrometer with the same number of channels. It can be made to be very compact and light weight, which might make it suitable for future space-based correlators. The stability of this instrument has been demonstrated from the various tests in Chapter 4. Phase switching solves the tough stability requirement in astronomical measurements, which is a significant improvement over the single dish acousto-optical spectrometers.

This instrument can also be used to measure any RF spectrum and the cross spectrum of any two RF signals. Since it is a time- integrating device, its sensitivity can be as high as one desires. With phase switching, one can compare the frequency characteristics of two closely matched microwave devices with great sensitivity. Because of its compactness, low cost and high sensitivity, it could be a useful and practical instrument for microwave measurements.

5.2 What have we learned?

5.2.1 The difficulties in the alignment

In this research, a very different setup of the interfering acousto-optical spectrometer was attempted. Instead of using a multi-channel Bragg cell, two single-channel Bragg cells are used. The use of single-channel Bragg cells provides absolute acoustic isolation of the channels and allows fringe widths to be adjustable. However, it also introduces other difficulties. First is the difficulty in aligning the two Bragg cells. Misalignment caused many undesirable effects such as the nonuniformity in the fringe spacing, the nonlinear compression of the frequency scale and the loss of the illumination. The other undesirable feature is the phase shift across the frequency channels, which must be compensated by a phase corrector.

Weighing the advantages and the disadvantages, it seemed that a multi-channel Bragg cell is more preferable, since a more compact system could be built, and the present day multi-channel Bragg cell channel-to-channel isolations are much better (better than 40db). It is a matter of trade-off whether one uses a multi-channel Bragg cell or many single-channel ones.

5.2.2 The stability is better than thought

The stability of the acousto-optical spectrometers has always been a concern and there has been no good scheme that guarantees its stability. With the interferometric spectrometers, there is a natural way to stabilize the zero level, which is by phase switching. From the measurement shown in Chapter 4, the zero level is very stable over a long integration time. The main source of instability was from the electronics. Occasionally, large spikes (4 σ) were also observed. They may be due various reasons explained in Chapter 4.

5.2.3 A CCD frame grabber is preferred

In this research, the full potential of the CCD is not utilized. Instead of having 403 channels of frequency resolution (the CCD has 512 x 403 pixels), only 241 channels are achieved. This is because the speed of the digital processor (both the A/D converter and the computer) is too slow to process all the data in real time. If a frame grabber is used together with a more powerful computer, a lot of problems associated with the digital readout will be gone, and the full potential offered by the CCD can be realized.

5.2.4 The phase shift is a problem

The phase shift across the frequency channels (Fig. 4-4) causes the detected amplitudes of the I and Q detectors to vary sinusoidally with respect to frequency. Although in principle, the fringe amplitude, $\sqrt{I^2+Q^2}$, should be constant, in practice, there may be some residual effects because of the incomplete cancellation of the zero level, optical misalignment etc. So, it is more preferable to remove this phase shift by the addition of a phase corrector rather than by software calibration.

5.2.5 Can ideal performance be obtained?

The ideal sensitivity of the AOCS is the same as other multiplying interferometers. As has been discussed in Chapter 3, the degradation of the SNR is due to the loss of signal visibility and the addition of noises. The noise degradation, which has been analyzed in Chapter 3, is very predictable and controllable. However, the visibility loss of the present instrument is about 50%. Most of this visibility loss came from the optical system misalignment and the RF channel mismatch. In principle, the visibility loss can be made to be very small. With a better optical alignment system, and the replacement of the faulty A/D converter, this instrument should be able to perform like

an ideal multiplying interferometer.

5.3 Possible improvements

Because of the budget constraints, many parts of the system are not made as well as they should be. With a slightly larger budget, many of these deficiencies can be removed. Here is a list of them.

5.3.1 Real time calibration

For continuous observation, one should provide a real time calibration scheme for this instrument. Both the phase and amplitude can be calibrated by injecting a reference CW signal into the RF. The computations required by this real time calibration can be performed later, provided that the fringe phase is stable within the coherence time of integration That is to say, the reference signal is also integrated as the other signals over the coherence time. This calibration can be performed by the present instrument with a little modification in hardware and software. Even real time calibration for every frame readout can be performed with a more powerful computer (about five times as fast).

5.3.2 Possible improvements on the optical system

1. The homemade optical mounts should be upgraded to higher quality commercial mounts so that the alignment can be done better and easier.

2. The laser should be upgraded to 5 mW and a variable beam attenuator should be added to control the amount of light falling onto the CCD detector.

3. The beam expansion can be made larger to fully utilize the frequency resolution of the Bragg cells by the addition of one more prism stage (a 2" x 2" laser prism is

needed).

4. The spatial filters (slits) need to be replaced by commercial adjustable slits so that there can be better control on the diffraction pattern.

5. The cylindrical lenses should be upgraded to laser quality ones with aberration correction.

6. An electro-optical phase corrector should be provided to remove the phase shift.

5.3.3 Possible improvements on the CCD camera readout

1. The faulty A/D converter should be replaced to improve the dynamic range of the system.

2. A frame grabber should be used to replace the present read-out scheme. It may cost a little more, but the number of frequency channels can be increased. A lot of other problems associated with the digital readout during the development stage can be avoided.

3. The phase-locked loop, which locked the camera with the system, should be re-designed so that it is more stable. An alternative is to use a European/Japanese camera that runs at 50Hz frame rate and can be locked directly to the system without a phase-locked loop.

5.3.4 Possible improvements on the RF circuitry

1. A reference calibration signal should be provided.

2. The present VHF outputs (40MHz to 120MHz) from the antenna IF chains are for the filter bank correlators, and do not match the frequency range of the Bragg cells (100MHz to 200MHz) very well. A new down conversion scheme should be made.

If Bragg cells with a much large bandwidth are used (say 1GHz), they may tap into the IF (about 1.4GHz) directly without further down conversions.

3. Higher power RF amplifiers (1 Watt) should be used to avoid saturation problems.

5.3.5 Selection of the control computer

1. A machine with a 16 bit data bus should be used.

2. If a frame grabber is used, one would need a much faster machine such as a Microvax.

3. There can be a lot more improvements on the software. The user interface can be expanded to provide more features for the convenience of the user. The system interface should be improved so that more control signals could flow between the antenna system and the AOCS to secure the data collection process. An example is the checking of the system "integration valid" bit so that the phase cycle can be repeated in case the front end phase-locked loop is in error.

5.4 What's next?

5.4.1 Recognizing the advantage of optical processing

Optical signal processing is the most rapidly advanced field in recent years. Optical signal processing offers many advantages over digital signal processing, namely,

1. massive parallelism in computation,

2. low cost per computation,

3. compactness.

Many high performance and compact devices with enormous power have been developed at an incredibly low cost. For example, CCDs with 2048 x 2048 pixels have been devel-

oped, and ordinary commercial CCDs with 512 x 403 pixels are available at a price of $200, which is about $0.001 per pixel! Even if the whole system cost is included (say with a camera system and a fast frame grabber), the cost is likely to be less than $0.025 per pixel. If every pixel can be utilized as an integrator, one can get 200,000 integrators (or more) for $0.025 per integrator. Similarly, Bragg cells are high quality channelized filters with wide bandwidths and high resolutions. Currently, the cost is about $1 per channel with bandwidths varying from 100KHz to 1MHz per channel. Compared to the crystal filters, this is two orders of magnitude less expensive. It is a matter of *properly utilizing the full potential of these devices* to make them very cost effective for various purposes. Below are several possible schemes that may utilize the full potential of these devices to perform the spectral correlations for many-element arrays at a very low cost.

5.4.2 Expanding a two-element correlator to a multi-element array

As has been discussed in the introduction, it is very expensive to do the back-end correlations when the number of array elements is large. Below are three different architectures that may provide a *very cost effective solution* to this problem. The practicality of these architectures is also discussed.

The interfering interferometer architecture

The interfering interferometer architecture (Fig. 5-1) [46],[19] is similar to the two-element prototype adopted in this research. The RF signals from the array elements are passed into a multi-channel Bragg cell. The fringes of different correlations are overlapped on the same detector position and have to be extracted by some algorithms.

The main disadvantage of this architecture is that when the number of array elements is large, there will be many different correlation pairs, and extracting them without any degradation is very difficult. For example, the VLA has 27 elements and 351

correlations. Building a 27-channel interfering acousto-optical correlation spectrometer is almost impossible. The practical limit is about 4 channels with 6 correlations. The other disadvantages are the channel cross talks and the difficulties in implementing a phase-switching algorithm, which has been proved to be very effective in this research in reducing the zero level fluctuation of the system.

The adding interferometer architecture

An attractive alternative is to use an adding interferometer architecture (Fig. 5-2). Basically, it is very similar to a single- channel AOS, except that the Bragg cell is fed with the sum of two RF signals to be correlated instead of a single dish signal. In Fig. 3-4 was shown a setup with four channels, which is equivalent to the two-channel interfering AOCS. If two channels are used instead of four channels, the sensitivity will be degraded by a factor of $1/\sqrt{2}$.

So, comparing to the interfering architecture, this architecture uses 2N(N-1) Bragg cell channels instead of N, where N is the number of array elements. The advantage of this architecture is that no interference is needed, so the alignment is easy, the RF signals to be correlated are matched, and there is no need to extract the different correlations. Thus, this architecture is capable of utilizing the full potential of the CCD and the multi-channel Bragg cells. Phase switching is also possible for this architecture. For example, to expand the Owens Valley three-element millimeter array to 6 elements with 15 baselines (or correlations), one would need a 60-channel Bragg cell and a high performance CCD imaging system. Both are available commercially. Conceivably, the total cost of such a system is *an order of magnitude less* than the corresponding filter bank or hybrid digital-analog correlator with the same number of channels [95].

The multiplying interferometer architecture

Another possibility, suggested by Esepkina [30] is a multiplying architecture (Fig. 5-3). The signal from one antenna is passed into an acousto-optical modulator. The diffracted beam is expanded and focused onto the second Bragg cell. The output is the correlation of the two signals. Putting a cylindrical Fourier transform lens at the output gives the spectral components of the cross spectrum. A laser diode modulated by RF can also be used in place of the AOM.

This architecture also allows the full potential of the multi-channel Bragg cells and CCDs to be realized, and allows phase switching. It uses N(N-1) Bragg cell channels and N(N-1) AOM channels (or an N(N-1) laser diode array). The optical system is a little more complicated, but is a good alternative from the adding interferometer architecture.

Appendices

Appendix A

The description of each major part of the AOCS

The spectrometer consists of the following major parts, namely, the Bragg cells and the RF drivers, the optical subsystem, the CCD detector and the data read-out, the timing and control circuitry, the control computer and the software interface. The design considerations will be discussed as the operation of each part is explained.

A.1 The physical layout of the hardware

The hardware consists of an optical alignment system (which includes a laser, a beam expander, a beam translator, a Mach-Zehnder type interferometer, spatial filters, an optical delay, and some cylindrical transform lenses), two Bragg cells and their RF drivers, an RF correlated and uncorrelated noise generator, a CCD video camera, a video amplifier, an A/D converter, an interface controller prototype card, a Tecmar Labmaster card, and a control computer (an IBM PC equivalent manufactured by Compaq). The Bragg cells, the RF drivers, the CCD camera, and the alignment optics are all mounted on the optical table.

The video amplifier, the A/D converter, and the control logic circuit are assembled on a prototype board plugged into one extension slot of the control computer. The circuit board is a double-sided prototype wire-wrapped/soldering board. The actual

circuitries are shown from Fig. A-2 to A-8. The Tecmar card is plugged into an adjacent slot of the prototype board and is connected to the prototype board by two bundles of edge connectors and connecting cables.

The schematic diagram is shown in Fig. 2-2.

A.2 The Bragg cells and the RF circuitry

In recent years, many high quality Bragg cells became available commercially at affordable costs. Bragg cells with bandwidths of 2GHz are not uncommon [37]. We decided to experiment with an inexpensive one, with a good deflection efficiency and a high resolution.

The chosen one is a low-cost Bragg cell with a modest 3db bandwidth of 100 MHz centered at 150 MHz. The peak deflection efficiency is 60%, achieved by acoustic phase array beam steering [76]. It is made of TeO_2 crystals with an aperture height of 4cm (access time is 10 usec). Thus, the time bandwidth product is about 1000. To achieve the maximum deflection efficiency, it has to be driven at 6 Watts of RF power. Hence, two RF amplifier chains with a maximum output of 0.5 Watt were built to drive the cells. Additional RF circuits for testing the instrument were also built. They will be discussed in Chapter 4.

A.3 The optical subsystem

A.3.1 The optical table and support

The instrument is set up on an 6' x 4' x 8" optical table top supported by two layers of sandbags and tire inner tubes for vibration isolation. Concrete blocks are put on top of each vibration isolation layer to maintain the level and even the loading. The sand isolates the low frequency vibrations and the tire inner tubes isolate the high

frequency vibrations from the floor. They are found to be very effective.

A.3.2 The laser

The laser is a 1mW He-Ne gas Laser operating at 633nm. The spot size is about 0.8mm with a divergence of 1.3mrad/m. The laser power requirement was figured out after an analysis of the optical losses of the system and the detector sensitivity (see the next chapter for more details). The cost of the laser is directly proportional to its power, so the lower the power required, the less is the cost. There is no particular reason for using He-Ne Laser other than its availability and its lower cost.

A.3.3 The beam expander

Expanding a laser beam by prisms [66] has the advantage that only one dimension is expanded, and the factor of expansion is adjustable. They are easy to use and have very little phase distortion. Multiple prism beam expansion stages can be conjuncted to get a higher expansion factor. In our setup, two 1" x 1", right-angled, BK-7, laser quality prisms are used. The surfaces are highly polished with a mean surface roughness of 1/20 wavelength. After the expansion, the beam has a cross section of about 0.8mm x 2cm. A single prism beam expander stage is shown in Fig. A-1. The expansion factors and the losses with respect to the incident angle are also shown.

A.3.4 The beam splitter

The beam splitter is a 2" diameter glass plate coated with partially reflective dielectric material (50% at 45^0 incident angle). A pellicle beam splitter had been used and found to be very unstable. The ghost images of the plate beam splitters did not seem to give any problem because of the presence of the slit spatial filters. The expanded beam is split into two equal intensity beams by this beam splitter, and illuminates the

Bragg cells.

A.3.5 The alignment of the Bragg cells

The Bragg cells are mounted on two homemade aluminum mounts. The mounts can be adjusted in all degrees of freedom in three dimensions and can also rotate in the plane of the beams. This allows the incident angle of the beams to be set to the Bragg angle for maximum deflection efficiency. It is very essential to have the Bragg cells aligned; otherwise, the diffracted beams would come out of the Bragg cells at an angle to one another, causing the fringes to have nonuniform widths.

A.3.6 The spatial filters

Before bringing the beams together, the beams pass through two narrow slits. The slits are homemade aluminum mounts with one razor blade on each side serving as the edges of the slits. The slits serve two purposes. Firstly, they act as spatial filters and cut down the scattered light and the ghost images from the beam splitters. Secondly, they control the widths of the diffraction lobes of the fringe axis. The slit widths are adjusted so that the resulting diffraction spot is much wider than one fringe width.

A.3.7 The optical phase delay

An optical flat is placed on a rotary mount on the pathway of one of the diffracted beams. By rotating the optical flat, the optical path traversed by the beam changes and so the delay is changed. In this way the fringe phase can be controlled precisely. The optical flat has a thickness of 1/8" and an r.m.s. surface roughness of 1/20 wavelength.

A.3.8 The beam recombination

The beams are brought to a very small separation in parallel by a mirror and a beamsplitter at the other end of the interferometer. The beamsplitter is the same as the one described above. This mirror, and all others used, have a diameter of 2", 96% reflective at $0.63\mu m$ (45^0 incident angle), and have an r.m.s. surface roughness of 1/8 wavelength. Higher performance laser mirrors were not used out of cost effectiveness considerations. The mirror is mounted on a linear translator. By moving the translator, the separation between the beams can be adjusted. This is *a very important feature* since it allows the fringes to be expanded and matches the detector geometry.

A.3.9 The cylindrical focusing lenses

After the beams have been brought back together for interference, they pass through two cylindrical lens combinations. The first set of cylindrical lenses has focal lengths of +25cm and -30cm. From them, effective focal lengths from 50cm to 100cm can be generated by varying the separation of the lenses. This set of lenses is oriented to focus the fringes onto the detector. The second set of cylindrical lenses has focal lengths of +15cm and -20cm. From them, effective focal lengths of 30cm to 60cm can be generated. This set of lenses is oriented to focus the frequency components onto the detector. This set of lenses has to be mounted slightly tilted to the horizontal so as to compensate for the tilting of the beams due to the Bragg angle difference. This helps to bring the various frequency components to the same focal distance. The lenses are all 50mm x 60mm, optical quality lenses. They did not degrade the resolution (see Chapter 4) but they have caused some non-linearity in both the frequency and fringe direction because of the lens aberrations.

A.4 The CCD camera and the data collection

The detector is a modified RCA CCD camera (model TC2821). The CCD chip on the camera is SID504, a small commercial device with 403 x 512 pixels. The pixel size is 16 μm x 20μm, and has a charge capacity of about 1.4 million electrons. The device is extremely sensitive, with a quantum efficiency over 0.5 in the visible light range and a signal-to-noise ratio better than 59db.

A.4.1 The area array detectors

The factors affecting the selection of the area array detectors are the cost, the pixel size, the charge capacity, the light sensitivity, the detector noises and the dynamic range. Photodiode arrays and CCDs are the most commonly used area array detectors. The photodiode arrays used to have a distinct advantage over CCDs by having a higher charge capacity (typically about 10^7). Hence, the shot noise degradation is smaller, and so the photodiode arrays do not have to be operated as fast as the CCDs. The disadvantages are the higher thermal noises, slower operating speed, lower sensitivity and thus higher illumination requirement.

A.4.2 The low cost high performance CCD chip

In recent years, the CCD quality to cost ratio continues to rise as CCDs are penetrating into many commercial markets. The charge capacity can be as high as the photodiode arrays (e.g. 1.4 million electrons for SID504) in a smaller area. Because of the superior device characteristics of the CCDs, they are preferred in many new applications.

While very high research quality CCD chips are available, they are relatively expensive (>$5000) and require a lot of effort to get them to work (i.e., building the data read-out circuitry for the CCDs). A way to get around all these labors and costs is to

use a low cost CCD camera. The CCD chip is usually smaller but the quality is still very good and the read out circuitry is provided. By slightly modifying the circuitry, the camera was made to work very soon. The thermal noise and the read-out noise of the device are very small. Since the camera is operated in the fast frame read out mode, they are not very important as the shot noise dominates (see next chapter for more details).

There is a small price to pay for cutting the corner. Since the chip SID504 was designed for TV applications, the architecture is less than perfect for our application. The 512 x 403 pixels of the device are divided into two banks of areas each having 256 x 403 pixels. One of the area bank is used for actual integration, while the other is used for data buffering. Such an architecture allows continuous integration while the data of the last frame is being processed. So the effective number of pixels is just 256 x 403.

When the frame transfer command is received, the device simply shifts the integrating area down to the storage area line by line. Thus, during the frame transfer, the integrated signals are polluted by the light of the other lines during shifting. Fortunately, the frame shift takes only about 1ms. Thus, if the integration time is 100ms, the pollution is only about 1%, and is not too significant.

Although there are other CCDs that have a different architecture and which do not have the above pollution problem, they do not have the high charge capacity, nor have a worse thermal noise performance, nor have a worse light sensitivity. For example, the Fairchild CCD222 has the data read-out transfer buffers, which avoids the above pollution problem, but it has a smaller charge capacity (200,000), a worse thermal noise (about 300e at room temperature), and a worse sensitivity.

The sensitivity of the CCDs is an important factor, which can affect the cost of the whole system. If a high power laser is required to illuminate the system, or if a high RF power is required to drive the Bragg cells, the system would be much more

expensive.

A.4.3 The camera circuitry

The camera comes with two circuit boards for reading out the video signal from the CCD at the standard EIA TV frame rate. There are two video timing chips that generate all the required signals for the CCD chip. One is a standard TV timing chip for generating the frame sync signals, and the other is a custom LSI chip for generating the three-phase signals necessary for operating the horizontal and the vertical charge transfer circuits of the CCD. The CCD is read continuously at the standard TV frame rate of 60 Hz, or an equivalent line rate of 15,750Hz.

Four modifications were made on the camera circuit.

The first modification [40] is to fix up the parts of the circuit that do not work because of the longer frame time. A longer frame time is necessary because the computer could not handle all the data processing within one standard TV frame time. The parts are the three vertical line drivers for the CCD chip. By replacing the capacitances C6, C12, and C18 of the circuit board by zener diodes 1N759A, the integration time can be held indefinitely long. The modification is shown in Fig. A-2.

The second modification is to change the interlacing mode of the camera to the non-interlacing mode. Since CCD SID504 is a very flexible device, one can achieve a higher resolution by manipulating the three-phase signals in different orders. This is explained as follows.

The image area of the CCD SID504 is entirely transparent, and the images of external objects are mapped perfectly onto the image area. After the integration is completed, the image area is segmented into 403 x 256 pixels (each pixel being a small bucket of charge) so that they can be read out. The three-phase signals, when applied alternately, would lower the potential of these buckets in a certain direction and cause

the charges of the buckets to flow in that direction. In this way, the charge buckets are shifted out sequentially, and each bucket remains intact with its charges [78].

Let the three-phase signals be labelled $\phi 1$, $\phi 2$, and $\phi 3$. When they are applied in this order to the CCD chip, the entire image area is segmented in a certain way. Now, when the three-phase signals are applied in the order $\phi 1$, $\phi 3$, and $\phi 2$, the image area is segmented differently. Specifically, each bucket area is offset from the previous bucket area by half a bucket width in the direction of the three-phase signals. By reading the CCD chip alternatively in these two configurations, the resolution is made twice as good. Of course, the corresponding TV signals must also be shifted by half a pixel size, so that when the pictures overlap, they complement each other and give the viewer the impression of twice the resolution.

This interlacing mechanism is very powerful in TV broadcasting, but could cause problems in our application. Thus, it is suppressed by tying pin 24 of the LSI three-phase timing chip (U1 on the circuit board) to $+V_{dd}$ instead of $-V_{dd}$. The interlacing pin is shown in Fig. A-3.

The third modification is performed to control the integration time (or frame time) of the system. The way to control the integration time is to suppress the flow of the control signals, which pass from one board to another by the analog switches. The control signals include the cathode blanking (K.Blank), the composite sync (C.SY), the horizontal drive (H.DR), and the vertical drive (V.DR). These signals are generated by the TV sync generator (U5 of the circuit board) and fed into the CCD LSI timing chip (U1). By blanking out these signals by the analog switches, one can inhibit the generation of the CCD read- out signals by the CCD LSI timing chip.

The control signals coming out of one board are directed to an external circuit, a prototype board described above. They are fed into some analog switches. The output

of these analog switches are then fed back to the other circuit board of the camera. When the external circuit desires a frame read-out, it will turn these anaolg switches on and let the control signals from the TV sync generator pass through. This modification is shown in Fig. A-4. Another way to do the same job is to analog-switch the CCD frame shift signals and let the timing generators be intact [40].

The fourth modification is to lock the camera with an external phase- locked loop. This is done by injecting the external phase locked loop signal into the TV sync generator (Fig. A-3). This is necessary because the camera has to be synchronized with the antenna phase switching (see more details later).

The above four modifications are all essential, but they are also chosen so that there is minimal on-circuit modification of the CCD camera. The integration time (or the number of frames) can be changed by a counter on the external circuit board.

The output video signal is a standard composite output, with a peak-to- peak voltage of 1.0 to 1.4V. This output is amplified by a video amplifier (described below) before it is sampled by an A/D converter.

A.4.4 The video amplifier

The A/D converter has an input voltage range of 5V or 10V, but the video output of the CCD camera is a standard video composite signal with a considerable smaller voltage range. So to fully utilize the dynamic range of the A/D converter, a video amplifier was added.

The amplifier is a single wide band operational amplifier with some feedback circuitry. The gain is adjustable from 7 to 20 by a trimmer on the feedback path. The resulting bandwidth is larger than 50 MHz and the maximum output level is $\pm 2.5V$. The circuit is shown in Fig. A-5.

A.4.5 The analog to digital converter

The A/D converter is a 12 bit hybrid analog circuit, which has a maximum data conversion rate of 1 MHz. It has a built-in sample and hold circuit, and operates with a minimum amount of external supporting circuitry and control signals. The accuracy of 12 bits is computed from the requirement that the shot noise dominates other noises, including the quantization noise due to the A/D converter. There is a quantitative statement in the next chapter.

Since this device is a very new product, some instability has been found on our chip when the input voltage is large. So care was taken to restrict the input voltage to the A/D converter. The A/D converter and its associated circuitry are shown in Fig. A-5.

A.4.6 The A/D converter data multiplexing

The digital outputs of the A/D converter are three-states buffered. In principle, they can be directly wired to the data bus of the control computer for direct memory access (DMA). However, the control computer, which has an 8-bit data bus, cannot latch in all 12 bits of the A/D converter in one data cycle. Hence, the digital outputs of the A/D converter are multiplexed onto the computer data bus in two data cycles by two multiplexers. The least significant eight bits are multiplexed as the first byte, and the most significant four bits preceded by four zeros are multiplexed as the second byte. The order of multiplexing is dictated by the byte-wrapping structure of the 8086 architecture. The circuit is shown in Fig. A-5.

A.5 The control computer and the timing and control circuitry

The control computer is a Compaq Plus IBM PC/XT compatible machine, with an 8088 processor running at a clock speed of 4 MHz. There are 512K RAM on the

mother board, and it has a 10Mbyte hard disk and a standard floppy disk drive. It is also equipped with an 8087 math co-processor.

The computer is used for controlling the CCD camera, collecting the data, and for reducing the data in real time. It is found to have adequate capacity for performing all the above jobs. However, there are two deficiencies. First is that the data bus is only 8 bits wide, despite the fact that it is a 16 bit machine. This is not quite suitable for the 12 bit A/D converter. A computer with a 16 bit data bus is much better. The second deficiency is the dynamic refreshing of the RAMs. This DMA request has the highest priority, but is a nuisance to our application, since it interferes with the data collection DMA request of the instrument.

A.5.1 The control of the integration time

The integration time is set to be an integral number of frames, each frame being a 525-lines, standard TV frame, with a duration of 16.67ms. A counter is used to keep track of the number of frames accumulated. When the counter resets, the analog switches will turn on, allowing one frame of the control signals from the TV timing chip to pass through to the custom LSI chip, thus activating a CCD frame transfer.

The present design uses a Johnson counter and the *frame count* is controlled by a dip switch on the prototype board. The dip switch can be set to 2, 4, 6, 8, 10 or 12. Hence, frame integration time from 33.3 ms to 200 ms in steps of 33.3 ms can be chosen by the appropriate setting. The circuit is shown in Fig. A-6.

A.5.2 The integration time

There are a few factors affecting the setting of the integration time (between 33.3 ms and 200 ms). The consideration is the degradation of system performance because of the detector noises. The quantitative statement is given in the next chapter. Here a

qualitative explanation is given.

The different kinds of noises associated with a detector are the photon shot noise, thermal noise, and read-out noise. The photon shot noise varies with the square root of the charges collected, and is inherent in all detectors. The only way to lower the photon shot noise is to increase the charge capacity of the detector. The thermal noise results from the thermal excitation of the device that causes some electrons to cross the potential barriers. The read-out noise refers to the noise added during charge transfer and output amplication. The thermal noise and the read-out noise are time- independent and are usually much smaller than the shot noise when the charge capacity approaches saturation.

To lower the shot noise, one can only increase the total charge capacity. By reading out the data as fast as possible, while keeping the integrated charge level for every frame close to saturation by stronger illumination, the total charge capacity-per-unit time is raised. Hence, the integration time should be made as short as possible. This is called the fast frame read-out mode.

The lower limit of the integration time is, of course, the time required to shift out one frame of CCD data. This could be as small as a few ms if a special read-out circuit is built. Even with the standard CCD camera circuit, the frame time is only 16.67 ms. However, this limit is not the only limit. Another limit that must be considered is the time one takes to reduce the data (such as the data accumulation). By writing these critical portions in 8086 assembly language, the computer can handle the data collection and all the necessary computations in about 70 ms per frame. The actual frame time is set to 0.1 sec for the convenience of phase switching. From the calculation shown in the next section, one can see that the shot-noise degradation with a frame time of 0.1 sec is less than 10 % (assuming the CCD pixels are near saturation when being read out).

A.5.3 Synchronizing the data collection with the system phase switching

The interferometer has two phase-switching schemes incorporated. Both phase-switching schemes phase modulate the front end local oscillator by injecting an appropriate phase at the lobe rotator.

The fast phase switching operates at 100Hz, 50Hz, 50Hz (two phases alternating at 180^0) for the three antennas, and aims at removing the zero level and gain variations. The slow phase switching operates at 10Hz, 5Hz and 5Hz for the three antennas. The switchings are four phases (90^0), and aim at separating the the two side bands that are present in the same IF band. One phase cycle would take 0.8 sec to complete.

The fast phase switching was not implemented in the AOCS for the reason discussed above. The slow phase switching was implemented by sending three bits from the system to the AOCS, specifying the status of the phase cycle. The AOCS control computer reads this status and take the corresponding action in the data collection algorithm. In case an integrating error occurs in the AOCS computer, it will skip the next few cycles until it reads the same phase again and repeats the integration.

The AOCS can make provisions for errors that occurred in the system during integration by reading an external "data valid" bit from the system before deciding whether or not to keep the data. This feature has not yet been implemented. During the test run, the AOCS simply ignored all system errors that might have occurred during integration.

A.5.4 Synchronizing the CCD camera with the antenna system

The CCD camera has a custom LSI chip, which generates all the sync signals for the output video signal. The chip has an input pin that locks itself with the 60Hz A.C.power supply. So the synchronization is achieved by supplying this pin with a 60Hz

signal synchronized with the antenna system. The 60Hz signal is generated by a phase-locked loop, which is locked to a 10Hz signal synchronized with the data integration cycle from the antenna system. This 10Hz signal is necessary and cannot be derived from the three bits of phase cycle signals above because the three bits are not synchronized with the data integration cycles.

A.5.5 Synchronizing the data collection with the CCD camera

The most essential circuitry is the circuit to enable the control computer to read in the data and to synchronize the data collection process. Just as the CCD camera has been synchronized with the antenna system, so the CCD frame signals are used as the synchronizing signals for the data collection process.

A lot of countings are done to synchronize the CCD camera video signal with the computer data collection. The reason is that the computer basic cycle time is about 1 μs, while the CCD video signal is at 8MHz; hence, the video signal is simply too fast for the computer. Since not all information on a line is needed to calculate the fringe amplitude and phase, only a few pixels per line need to be read.

The hardware consists of a Tecmar Labmaster card and some other logic circuitry on the prototype board. The schematic diagram is shown in Fig. A-7. Only the counters on the Tecmar Card are used. Counter A is set to mode C (see the Tecmar Labmaster reference manual for details) by software and is used for gating the vertical line signals. Counter B is set to mode L and counter C is set to mode Q. Both counters B and C are used for gating the horizontal signals.

The counters are on the same LSI MOS chip (AMD Am9513), with a maximum counting frequency of 7MHz. But the control signal H.DR. has a maximum frequency of 8MHz. Hence, for safety, H.DR. is passed through a divide-by-four counter before it is being counted by counters B and C.

The synchronization is done by hardware. When an "integrate" command is received, the software will send a signal to turn on the whole data collection hardware. This is done by setting pin 1 and pin 13 of the D-flip-flops (U18 of the prototype board). Once they are set, the flip-flop can be turned on by a V.DR. pulse. The V.DR. pulse is basically the frame start pulse of the CCD camera, and hence, it serves as the synchronization pulse.

A.5.6 Synchronizing the CCD line readout

Once the above flip-flop is turned on, it turns on counter A, and lets it gate through all line pulses of that frame. These line pulses then turn on counter B which keeps track of H.DR.. Counter B issues a level signal to counter C at the same section of each line, and enables counter C to count repetitively during that section. Hence, the number of pixels to be read per line can be changed by lengthening or shortening the level signal of counter B. The starting place of each line can also be changed by changing the hold register of counter B. In this setting, the load register of counter B must be an integral multiple of the hold register of counter C for the counting to work properly.

A.5.7 The A/D converter encode command

Each terminal pulse of counter C creates an encode command to the A/D converter. A delayed pulse (about 1 us) is sent to the "strobe" pin of the A/D converter. The delay is done by a one-shot (U7 of Fig. A-5). The circuit is shown in Fig. A-5.

A.5.8 The level translation

The control signals from the CCD camera are CMOS signals at +8.5V and -5V. The computer signals are TTL at +5V and 0V, so the camera signals are passed through a level translator (U5 of Fig. A-4) before they interact with the computer.

A.5.9 The DMA request and the data collection

Simultaneous to the encode command to the A/D converter, a DMA request signal is sent to the computer. The DMA request is wired to the DRQ1 of the I/O expansion slot bus of the computer. There are four DMA request lines on the computer, but the other three lines are used up by the system and only one DMA line is available for external use. Since two bytes must be transferred per A/D conversion, the DMA request is generated twice for every encode command of the A/D converter. The circuit and the control signals are shown in Fig. A-8.

The advantages of using DMA is that it is faster, the maximum data transfer rate being over 1 Mbyte/sec. Handshaking is also done automatically via the DMA acknowledge line (DACK1). Hence, secure data transfer is assured. Of course, one needs to be sure that the DMA request is not generated at a rate faster than its capacity.

The computer uses dynamic RAMs, and they have to be refreshed once every few milliseconds. So there is a dynamic refreshing circuitry hardwired into the computer, which employs the DMA0 line to generate a dummy data read for every refreshing request. Since the DMA0 line has the highest priority, it must be handled by the computer before anything else. Thus, the duration between the A/D conversions must allow for such an occurrence in the middle of the process. This tends to lower the overall conversion rate of the A/D conversions.

In the actual operation, it was found that some data were missing occasionally when a faster computer (the Compaq Deskpro) was used, and it is believed that the loss was due to the DMA request competition and the incompatibility of the 8086 data bus (16 bits) with the I/O bus (8-bits). By lowering the conversion rate, the amount of losses decreases. At the present setting, with four conversions done per line (i.e., 8 DMA request per 63.5 us), about 7% of all frames are corrupted with one loss or so, and

must be rejected. This problem is fixed by using a slower but compatible Compaq Plus computer, which has an 8-bit processor data bus.

A.5.10 The DCC interrupt

DCC stands for data collection completed. During the data collection, the computer is halted, waiting for an external interrupt to resume its operation. After all the lines in the frame have been read, the interface circuit issues an interrupt signal to reactivate the halted computer. The circuit is shown in Fig. A-7 (U18). Once the operation resumes, the computer checks to see how much data has been read in. If the check sum is not correct, then the frame must be rejected. In this way, the system is protected from corruption by bad data.

A.6 The software

The software can be divided into the instrument interface and the user interface. The instrument interface consists of two parts. The hardware controller part, which is written in MS-8086 Macro Assembly language (version 4.1), is for controlling the operation of the CCD camera and for data collection. The data processing algorithms part, written in high level MS-Pascal (version 3.2), is for continuous data accumulation and for real time data processing during integration. The user interface is also written in MS-Pascal, allowing the user to specify different tasks to the system. All the software is linked together into a single package. The entire program is listed elsewhere.

The instrument interface performs the following major tasks.

1. The initialization and synchronization of the instrument.

2. The data read-out.

3. The calibration of the zero level and the gain variation of each pixel.

4. The continuous integration and the real time data processing.

5. The phase-switching cycles and the real time data processing.

6. The computation of the fringe amplitude and phase.

7. The separation of the side bands.

The first two tasks above are basically the interface to the prototype controller card. They consist of the following individual tasks:

1. Synchronizing the data collection with the system phase cycle by reading the three bits specifying the status of the phase cycle from the antenna system.

2. Initializing the counters on the Tecmar Labmaster Card. The counters are for keeping track of the data transfers from the CCD camera to the computer, initiating the appropriate signals to activate the A/D conversion and the DMA request at the right timing.

3. Initializing the digital I/O ports on the Tecmar Labmaster card and starting the data collection cycle by resetting the two master control flip-flops (U18 of Fig. A-7) of the circuit. The digital I/O ports are for controlling the two master flip-flops above. These flip-flops act as the turnkey elements of the hardware. When they are set, they wait for the synchronization signal from the camera. When the signal arrives, they turn on the hardware to begin a frame read-out cycle.

4. Initializing the DMA registers on the computer for automatic reading of the data.

5. Terminating the data collection cycle by interrupting the computer at the end of the data frame, and turning off the turnkey master flip flops.

The other tasks are for the data processing, aimed at calibrating the instrument and for measurements. These tasks will be described in more detail in Chapter 4.

The user interface is basically a hierachical menu system, which allows the user to use and to debug the instrument. The following tasks can be performed.

1. The calibration of the zero level. and the gain variation of each pixel.
2. The evaluation of the noise performance of the system.
3. The continuous integration or the phase-switched integration cycles.
4. The single cycle integration.
5. The removal of the zero level from the the raw data and the correction of the pixel gain variations.
6. The computation of the fringe amplitude and phase, and the separation of the side bands.
7. The display of the raw data, the integrated data, the corrected data, the pixel gain calibration data, the zero level data, the fringe amplitude and phase or the quadrature components of the fringe.
8. The graphic display of the data.
9. To get the statistics of any of the above data set.
10. The setting of the system parameters.
11. The saving and loading of the data into/from files.
12. The debug mode to save 8 subsequent frames when one frame check sum is wrong.

The user interface contains almost everything that is needed by the user. The actual commands and the detailed working will not be described here. More details can be found from the program listing.

Appendix B

Physics of the Bragg cell

The following simplified analysis basically follows the couple mode analysis of the Bragg diffraction in a periodic medium [90]. A more complete treatment can be found in the above reference. A Bragg cell is an acousto-optical deflector operating in the Bragg regime (Fig.B-1). The center piece of a Bragg cell is a photoelastic material, which couples the mechanical strain to the optical index of refraction. When a plane acoustic wave propagates in the photoelastic medium, there is a strain field that is a periodic function of position, and the refractive index of the medium becomes periodically perturbed with a period equal to that of the acoustic wavelength. Consider for simplicity an isotropic photoelastic material. The modulation in the dielectric constant of the photoelastic material due to the acoustic strain field can be represented by:

$$\Delta\varepsilon(z,t) = \Delta\varepsilon\cos(\Omega t - Kz). \tag{B.1}$$

Assume that the periodic dielectric perturbation couples the incident and the diffracted light wave is represented by:

$$\mathbf{E} = A_1\mathbf{E}_1 \exp i(\omega_1 t - \mathbf{k}_1.\mathbf{r}) + A_2\mathbf{E}_2 \exp i(\omega_2 t - \mathbf{k}_2.\mathbf{r}), \tag{B.2}$$

where $\mathbf{E}$ is the total electric field, and $\mathbf{E}_1$ and $\mathbf{E}_2$ are the incident and the diffracted field with propagation vectors $\mathbf{k}_1$ and $\mathbf{k}_2$ and frequencies ω_1 and ω_2, respectively. From Maxwell's equations, $\mathbf{E}$ must satisfy the following wave equation:

$$[\nabla^2 + \omega^2\mu(\varepsilon + \Delta\varepsilon)]\mathbf{E} = 0. \tag{B.3}$$

Both $\mathbf{E}_1 \exp i(\omega_1 t - \mathbf{k}_1.\mathbf{r})$ and $\mathbf{E}_2 \exp i(\omega_2 t - \mathbf{k}_2.\mathbf{r})$ are solutions of the above equation when $\Delta\varepsilon = 0$. For small perturbations, the parabolic approximation [90] is valid and $\partial^2 A/\partial z^2$ and $\partial^2 A/\partial x^2$ can be neglected from the above equation. The time dependence of the mode amplitudes can be neglected since Ω is much smaller than $\omega_{1,2}$, and the dielectric perturbation $\Delta\varepsilon$ is essentially stationary. In the case of small incident angle or large incident angle, the mode amplitudes A_1 and A_2 depend only on x or z. Here we shall examine only the case of small incident angle. $\mathbf{E}$ can be written as

$$\mathbf{E} = A_1\mathbf{E}_1 \exp i(\omega_1 t - \alpha_1 x - \beta_1 z) + a_2\mathbf{E}_2 \exp i(\omega_2 t - \alpha_2 x - \beta_2 z). \tag{B.4}$$

Substituting $\mathbf{E}$ into the above equation, we have:

$$\begin{aligned} -2i\alpha_1 \frac{dA_1}{dx}\mathbf{E}_1 \exp i(\omega_1 t - \alpha_1 x - \beta_1 z) - 2i\alpha_2 \frac{dA_2}{dx}\mathbf{E}_2 \exp i(\omega_2 t - \alpha_2 x - \beta_2 z) = \\ -\omega^2\mu(\varepsilon_1 \exp i(\Omega t - Kz) + \varepsilon_1 \exp -i(\Omega t - Kz)) \\ \times[A_1\mathbf{E}_1 \exp i(\omega_1 t - \alpha_1 x - \beta_1 z) - A_2\mathbf{E}_2 \exp i(\omega_2 t - \alpha_2 x - \beta_2 z)]. \end{aligned} \tag{B.5}$$

When the energy and momentum conservation conditions (Bragg condition) are satisfied, $\omega_2 = \omega_1 \pm \Omega$ and $\beta_2 = \beta_1 \pm K$, the above equation can be decoupled into the following equations:

$$\begin{aligned} \frac{dA_1}{dx} &= -i\kappa_{12} A_2 \exp i(\Delta\alpha x) \\ \frac{dA_2}{dx} &= -i\kappa_{12}^* A_1 \exp i(-\Delta\alpha x), \end{aligned} \tag{B.6}$$

where κ_{12} is the coupling constant equal to $\omega\Delta\varepsilon\mathbf{E_1}\mathbf{E_2}/8$, and $\Delta\alpha = \alpha_1 - \alpha_2$ is the momentum mismatch in the x-direction. The Bragg condition is satisfied when $\beta_1 = -\beta_2 = \pm k \sin\theta_B = \pm K/2$. Physically, this corresponds to the emission or absorption of a phonon. The Bragg angle of incidence is given by:

$$\theta_B = \sin^{-1}(\frac{K}{2k}) = \sin^{-1}(\frac{\lambda}{2\Lambda}). \tag{B.7}$$

At this incident angle, the momentum mismatch $\Delta\alpha = 0$ (Fig. B-2). The solution of the decoupled equation is:

$$\begin{aligned} A_1(x) &= A_1(0)\cos\kappa x - i\frac{\kappa_{12}}{\kappa}A_2(0)\sin\kappa x \\ A_2(x) &= A_2(0)\cos\kappa x - i\frac{\kappa_{12}^*}{\kappa}A_1(0)\sin\kappa x, \end{aligned} \tag{B.8}$$

where $\kappa = |\kappa_{12}|$. Consider a single wave incident at $x = 0$; the solution becomes

$$\begin{aligned} A_1(x) &= A_1(0)\cos\kappa x \\ A_2(x) &= -i\frac{\kappa_{12}^*}{\kappa}A_2(0)\sin\kappa x, \end{aligned} \tag{B.9}$$

and $|A_1(x)|^2 + |A_2(x)|^2 = |A_1(0)|^2$ shows that the total mode power is conserved. The fraction of the power of the incident beam transferred into the diffracted beam is given by:

$$\begin{aligned} \frac{I_{diffracted}}{I_{incident}} &= \frac{|A_2(L)|^2}{|A_1(0)|^2} = \sin^2\kappa L \\ &= \sin^2\left(\frac{\pi L}{\sqrt{2}\lambda}\sqrt{M_2\, I_{acoustic}}\right), \end{aligned} \tag{B.10}$$

where L is the interaction distance, $I_{acoustic}$ is the acoustic intensity, and $M_2 = \frac{n^6\overline{p}^2}{\rho v^3}$ is the diffraction figure of merit. n is the refractive index of the material, v is the acoustic velocity in the material, ρ is the mass density of the material, and $\overline{p}$ is the effective photoelastic coefficient of the material.

When the incident angle is not exactly the Bragg angle, say $\theta_1 = \theta_B + \Delta\theta$, then the Bragg condition requires that $\theta_2 = \theta_B - \Delta\theta$ and $\Delta\alpha = 2k\Delta\theta\sin\theta_B = K\Delta\theta$. The solution to the decoupled equation with $A_2(0) = 0$ becomes:

$$\begin{aligned} A_1(x) &= \exp i(\Delta\alpha x/2)A_1(0)[\cos sx - i\frac{\Delta\alpha}{2s}\sin sx] \\ A_2(x) &= -i\exp -i(\Delta\alpha x/2)A_1(0)\frac{\kappa_{12}^*}{s}A_1(0)\sin sx, \end{aligned} \tag{B.11}$$

where $s^2 = \kappa^2 + (\Delta\alpha/2)^2 = \kappa^2 + (K\Delta\theta/2)^2$.

The diffraction efficiency is:

$$\frac{I_{diffracted}}{I_{incident}} = \frac{\kappa^2}{\kappa^2 + (\frac{K\Delta\theta}{2})^2} \sin^2 \kappa L \sqrt{1 + (\frac{K\Delta\theta}{2\kappa})^2}. \tag{B.12}$$

The maximum diffraction efficiency is $\frac{\kappa^2}{\kappa^2+(\frac{K\Delta\theta}{2})^2}$. The bandwidth can be found by differentiating the Bragg condition:

$$\Delta f = \frac{2nv\cos\theta_B}{\lambda}\Delta\theta. \tag{B.13}$$

The number of resolvable spots N can be found when the laser beam spot size ω_0 is known:

$$N = \frac{\Delta\theta}{\delta\theta}, \tag{B.14}$$

where $\delta\theta = 2\lambda/\pi n\omega_0$ is the Gaussian laser beam divergence angle. Therefore,

$$N = \frac{\pi\omega_0}{2v\cos\theta_B}\Delta f = \tau\Delta f, \tag{B.15}$$

where $\tau = \frac{\pi\omega_0}{2v\cos\theta_B}$ is the access time of the deflector.

Appendix C

The effect of the finite aperture size on the fringe

Consider a monochromatic polarized plane wave illuminating two rectangular apertures (fig. C-2). The electromagnetic field at the Fraunhofer region can be represented by a single scalar field [34]:

$$\begin{aligned} u(x_1, y_1) &= a_1 \exp j\phi_{a_1} rect[(x_1 - D/2)/L_x] rect[y_1/L_y] \\ &\quad + a_2 \exp j\phi_{a_2} rect[(x_1 + D/2/L_x] rect[y_1/L_y], \end{aligned} \tag{C.1}$$

where $rect[x] = 1 for |x| < 1/2$, 0 otherwise. The resultant amplitude at the Fraunhofer region is:

$$U(x_0, y_0) = k \int_{-\infty}^{+\infty} u(x_1, y_1) \exp[-j2\pi(x_0 x_1 + y_0 y_1)/\lambda z] dx_1 dy_1 \tag{C.2}$$

$$\begin{aligned} &= ka_1 L_x L_y exp(j\pi x_0 D/\lambda z + \phi_{a_1}) sinc(x_0 L_x/\lambda z) sinc(y_0 L_y/\lambda z) + \\ &\quad ka_2 L_x L_y exp(-j\pi x_0 D/\lambda z + \phi_{a_2}) sinc(x_0 L_x/\lambda z) sinc(y_0 L_y/\lambda z), \end{aligned} \tag{C.3}$$

where k is a constant factor, λ is the wavelength, z is the focal length of the Fourier transform lens, and $sinc(x) = sin(\pi x)/\pi x$.

The intensity $I(x_0, y_0)$ is:

$$\begin{aligned} I(x_0, y_0) &= |U(x_0, y_0)|^2 \\ &= (kL_x L_y sinc(x_0 L_x/\lambda z) sinc(y_0 L_y/\lambda z))^2 \\ &\quad (a_1^2 + a_2^2 + 2a_1 a_2 cos(2\pi x_0 D/\lambda z + \phi)). \end{aligned} \tag{C.4}$$

It can be seen from the last equation that the intensity distribution is the same as that produced by the point sources except by the diffraction envelope $sinc^2$ due to the finite size of the apertures.

Appendix D

The effect of the optical surface roughness on the interferometer visibility

In this appendix, the expressions for the expected value of the intensity in the image plane (Fraunhofer region), due to two distinct but highly coherent (both spatially and temporally) sources, are derived. The present approach extends the treatment of scattering from a single rough surface by Chandley [16],[17], Chandley and Welford[15] to two distinct surfaces. The expressions derived here allow one to evaluate the loss of illumination and the degradation in system sensitivity (or visibility) due to the roughness of the optical surfaces traversed by the laser beam (see Section 3.4). Depolarization effects are ignored in the present treatment and are justified when the surfaces under consideration are relatively smooth. The roughness is also assumed to be homogeneous throughout the surface.

The treatment assumes that the surface roughness causes a small phase fluctuation of the wavefront of the illumination, which is characterized by its autocorrelation function and the r. m. s. value of the phase fluctuation. This assumption is valid for smooth surfaces. To first order, the visibility is lowered by a factor $\exp(-\sigma_\psi^2)$ [82], where σ_ψ^2 is the r. m. s. phase fluctuation of the wavefront. If higher accuracy is desired, one must measure the autocorrelation function of the phase fluctuation and integrate the expression numerically. The same treatment can be applied to other physical effects (such

as air turbulence) which introduce a small phase fluctuation to the wavefront.

Following the notations of appendix C, the intensity due to any aperture in the Fraunhofer region is:

$$\begin{aligned} I(x_0,y_0) &= |U(x_0,y_0)|^2 \\ &= k^2 \int_{-\infty}^{+\infty} (x_1,y_1)dx_1dy_1exp[-j2\pi(x_0x_1+y_0y_1)/\lambda z] \times \\ &\quad \int_{-\infty}^{+\infty} u^*(x_2,y_2)dx_2dy_2exp[+j2\pi(x_0x_2+y_0y_2)/\lambda z] \qquad \text{(D.1)} \\ &= k^2F\{U(x,y)\}F\{U^*(-x,-y)\}, \qquad \text{(D.2)} \end{aligned}$$

where F{ U(x,y) } denotes the Fourier transform of U(x,y).

By the convolution theorem, one gets:

$$I(x_0,y_0) = k'^2F\{U(x,y) \otimes U^*(-x,-y)\}, \qquad \text{(D.3)}$$

where k' differs from k by some constant factors.

Let the aperture function $U(x,y)$ be composed of two distinct apertures $U_1(x,y)$ and $U_2(x,y)$, where

$$U_1(x,y) = \begin{cases} U(x,y) & \text{if the point (x,y) is in aperture I} \\ 0 & \text{if the point (x,y) is not in aperture I} \end{cases}$$

$$U_2(x,y) = \begin{cases} U(x,y) & \text{if the point (x,y) is in aperture II} \\ 0 & \text{if the point (x,y) is not in aperture II.} \end{cases}$$

Splitting U into U_1 and U_2, we have:

$$\begin{aligned} I(x_0,y_0) &= k'^2[\int\int_{-\infty}^{+\infty} U_1... + \int\int_{-\infty}^{+\infty} U_2...][\int\int_{-\infty}^{+\infty} U_1^*... + \int\int_{-\infty}^{+\infty} U_2^*...] \\ &= k'^2[\int\int_{-\infty}^{+\infty} U_1... \int\int_{-\infty}^{+\infty} U_1^*... + \int\int_{-\infty}^{+\infty} U_2... \int\int_{-\infty}^{+\infty} U_2^*... \\ &\quad + \int\int_{-\infty}^{+\infty} U_1... \int\int_{-\infty}^{+\infty} U_2^*... + \int\int_{-\infty}^{+\infty} U_1^*... \int\int_{-\infty}^{+\infty} U_2...] \\ &= I_1(x_0,y_0) + I_2(x_0,y_0) \\ &\quad + k'^2F\{U_1(x,y) \otimes U_2^*(-x,-y) + U_1^*(-x,-y) \otimes U_2(x,y)\}. \qquad \text{(D.4)} \end{aligned}$$

where I_1 and I_2 are the intensities due to apertures I and II alone. The last term represents the interference effect of the two source apertures. For highly coherent sources (both temporally and spatially), one can further simplify the last term by writing the aperture distribution in the following form:

$$\begin{aligned} U_1(x,y) &= V_1(x,y)exp[j\psi_1(x,y)] \\ U_2(x,y) &= V_2(x,y)exp[j\psi_2(x,y)], \end{aligned}$$

where V_1 and V_2 are real functions of two variables representing the amplitudes of the aperture functions, and ψ_1 and ψ_2 are real stationary Gaussian functions of two variables with zero means representing the phase of the aperture functions. With this representation, the surface roughness is incorporated into the phase fluctuation of the aperture. This is a very useful representation for smooth surfaces (r. m. s. roughness $<< \lambda$).

For smooth optical surfaces (e.g., laser mirrors) illuminated by a laser beam, V(x,y) is Gaussian, $< \psi(x,y) >= 0$ and $< \psi^2(x,y) >= (2\pi/200)^2$ [71]. $< \psi >$ denotes the ensemble average of ψ. One can now proceed to evaluate the ensemble average of $I(x_0, y_0)$.

$$\begin{aligned} < I(x_0,y_0) > &= < I_1(x_0,y_0) > + < I_2(x_0,y_0) > + \\ & \quad k'^2 < F\{U_1(x,y) \otimes U_2^*(-x,-y) + U_1^*(-x,-y) \otimes U_2(x,y)\} > \end{aligned} \tag{D.5}$$

Assuming that the ensemble averaging commutes with integrations, one has:

$$\begin{aligned} & < F\{U_1(x,y) \otimes U_2^*(-x,-y)\} > \\ & \quad = F\{< U_1(x,y) \otimes U_2^*(-x,-y) >\} \\ & \quad = F\{\int \int_{-\infty}^{+\infty} < V_1(x_1,y_1)V_2(-x+x_1,-y+y_1) \times \\ & \quad \exp j[\psi_1(x_1,y_1) - \psi_2(-x+x_1,-y+y_1)] > dx_1 dy_1 \\ & \quad = F\{\int \int_{-\infty}^{+\infty} V_1(x_1,y_1)V_2(-x+x_1,-y+y_1) \times \\ & \quad < \exp j[\psi_1(x_1,y_1) - \psi_2(-x+x_1,-y+y_1)] > dx_1 dy_1\}. \end{aligned} \tag{D.6}$$

The last step assumes that V_1 and V_2 are slowly varying functions (spatially) compared to ψ_1 and ψ_2. Assuming that the surface roughness (height) has a Gaussian distribution, and that the r. m. s. phase fluctuation is much less than 2π, one has:

$$< \exp j[\psi_1(x_1, y_1) - \psi_2(-x + x_1, -y + y_1)] >= exp[-\sigma^2_{\psi_{12}}(x, y)/2], \qquad (D.7)$$

where $\sigma^2_{\psi_{12}}(x, y)$ is the variance of the random Gaussian function $\psi_1(x_1, y_1) - \psi_2(-x + x_1, -y + y_1)$. Hence,

$$< F\{U_1(x, y) \otimes U_2^*(-x, -y) >\} =$$
$$F\{exp[-\sigma^2_{\psi_{12}}(x, y)/2] \int \int_{-\infty}^{+\infty} V_1(x_1, y_1)V_2(-x + x_1, -y + y_1)dx_1 dy_1\}. \qquad (D.8)$$

The last term inside the integral is the same expression that would be obtained when the two source apertures were perfectly coherent.

One can proceed further with the following identity:

$$\begin{aligned} \sigma^2_{\psi_{12}}(x, y) &= < [\psi_1(x_1, y_1) - \psi_2(-x + x_1, -y + y_1)]^2 > \\ &= < \psi_1(x_1, y_1)^2 > + < \psi_2(-x + x_1, -y + y_1)^2 > \\ &\quad - < 2\psi_1(x_1, y_1)\psi_2(-x + x_1, -y + y_1) > . \end{aligned} \qquad (D.9)$$

Physically, the phase at any point in one aperture is independent of the phase at any point of the other aperture, and so $< 2\psi_1(x_1, y_1)\psi_2(-x + x_1, -y + y_1) >= 0$. With the assumption that the roughness is homogeneous and that the apertures are similar (i.e., they have the same statistical properties), one obtains:

$$\sigma^2_{\psi_{12}}(x, y) = 2\sigma^2_{\psi_1}. \qquad (D.10)$$

Hence,

$$< F\{U_1(x, y) \otimes U_2^*(-x, -y) >\} =$$
$$exp[-\sigma^2_{\psi_1}] \times F\{\int \int_{-\infty}^{+\infty} V_1(x_1, y_1)V_2(-x + x_1, -y + y_1)dx_1 dy_1\}. \qquad (D.11)$$

Similarly,

$$< F\{U_1^*(-x,-y) \otimes U_2(x,y) >\} =$$
$$exp[-\sigma_{\psi_1}^2] F\{\int\int_{-\infty}^{+\infty} V_1(-x+x_1,-y+y_1)V_2(x_1,y_1)dx_1dy_1\}. \qquad \text{(D.12)}$$

Now one can proceed to evaluate $< I_1(x_0,y_0) >$. Following the same procedure, one arrives at:

$$\begin{aligned} < I_1(x_0,y_0) > &= k'^2 < F\{U_1(x,y) \otimes U_1^*(-x,-y)\} > \\ &= k'^2 F\{exp[-\sigma_{\psi_{11}}^2(x,y)/2] \times \\ &\quad \int\int_{-\infty}^{+\infty} V_1(x_1,y_1)V_2(-x+x_1,-y+y_1)dx_1dy_1\}, \end{aligned} \qquad \text{(D.13)}$$

where $\sigma_{\psi_{11}}^2(x,y)$ is the variance of the random Gaussian function $\psi_1(x_1,y_1) - \psi_1(-x+x_1,-y+y_1)$. Unlike $\sigma_{\psi_{12}}^2(x,y)$, $\sigma_{\psi_{11}}^2(x,y)$ is not independent of (x,y). In fact,

$$\begin{aligned} \sigma_{\psi_{11}}^2(x,y) &= < [\psi_1(x_1,y_1) - \psi_1(-x+x_1,-y+y_1)]^2 > \\ &= < \psi_1(x_1,y_1)^2 > + < \psi_1(-x+x_1,-y+y_1)^2 > \\ &\quad - < 2\psi_1(x_1,y_1)\psi_1(-x+x_1,-y+y_1) > \\ &= 2\sigma_{\psi_1}^2 - < 2\psi_1(x_1,y_1)\psi_1(-x+x_1,-y+y_1) > . \end{aligned} \qquad \text{(D.14)}$$

Let $C(x,y) =< \psi_1(x_1,y_1)\psi_1(-x+x_1,-y+y_1) > /\sigma_{\psi_1}^2$ denote the normalized autocorrelation function of ψ_1. Then

$$\begin{aligned} < I_1(x_0,y_0) > &= k'^2 F\{exp(-\sigma_{\psi_1}^2[1-C(x,y)]) \times \\ &\quad \int\int_{-\infty}^{+\infty} V_1(x_1,y_1)V_1(-x+x_1,-y+y_1)dx_1dy_1\}. \end{aligned} \qquad \text{(D.15)}$$

Hence, the expression differs from the perfectly coherent case by the factor $\exp \sigma_{\psi_1}^2[1 - C(x,y)]$ inside the integral. From the homogeneity assumption, one can write $C(x,y) = C(\rho)$, where $\rho^2 = x^2 + y^2$. With a known $C(\rho)$, one can determine $< I(x_0, y_0) >$. For many years it has been assumed that $C(\rho)$ is Gaussian (e.g. [1]), but in recent years, $C(\rho)$ has been measured and found to be quite different from a Gaussian distribution [2],[3],[4],[15],[17]. With a given $C(\rho)$, and a known aperture illumination, one can numerically integrate the equations above to obtain the intensity distribution and the visibility loss.

To first order, one can ignore the effect of the autocorrelation function $C(\rho)$. Then the intensity distribution is exactly the same as that for a smooth surface, with a reduction of the total illumination by a factor $\exp[-\sigma_{\psi_1}^2]$, which depends only on the r. m. s. surface roughness. Thus, the visibility is also degraded by $\exp[-\sigma_{\psi_1}^2]$.

The results derived above are quite general and are applicable to all kinds of aperture illumination. The results are also independent of the shape of the apertures as long as the surfaces are relatively smooth and homogeneous.

In concludion, the general expression for $< I(x_0, y_0) >$ is:

$$
\begin{aligned}
< I(x_0, y_0) > =& < I_1(x_0, y_0) > + < I_2(x_0, y_0) > + \\
& k'^2 < F\{U_1(x,y) \otimes U_2^*(-x,-y) + U_1^*(-x,-y) \otimes U_2(x,y)\} > \\
& = k'^2 \exp(-\sigma_{\psi_1}^2) F\{\int\int_{-\infty}^{+\infty} exp[\sigma_{\psi_1}^2 C(x,y)][V_1(x_1,y_1)V_1(-x+x_1,-y+y_1) + \\
& V_2(x_1,y_1)V_2(-x+x_1,-y+y_1)]dx_1dy_1 + \int\int_{-\infty}^{+\infty} [V_1(x_1,y_1)V_2(-x+x_1,-y+y_1) \\
& + V_1(-x+x_1,-y+y_1)V_2(x_1,y_1)]dx_1dy_1\}. \qquad \text{(D.16)}
\end{aligned}
$$

Appendix E

Separation of the side bands

If a double side-band signal with a four phase switching is applied synchronously at the front end local oscillator and at the integrating buffers, the side bands can be separated by the following algorithm:

Let $F_0(I)$, $F_0(Q)$, $F_{90}(I)$, and $F_{90}(Q)$ represent the amplitude detected by the I and Q detectors, with the susbscript 0 or 90 denoting the phase shift of the first front end local oscillator, and let U and ϕ_u, L and ϕ_l be the amplitude and phase of the upper side band and lower side band, respectively. Then,

$$\begin{aligned} F_0(I) &= U\sin\phi_u + L\sin\phi_l \\ F_0(Q) &= U\cos\phi_u + L\cos\phi_l \\ F_{90}(I) &= U\sin(\phi_u + 90^0) + L\sin(\phi_l - 90^0) \\ F_{90}(Q) &= U\cos(\phi_u + 90^0) + L\cos(\phi_l - 90^0). \end{aligned}$$

Therefore,

$$\begin{aligned} U\sin\phi_u &= \frac{1}{2}[F_0(I) - F_{90}(Q)] \\ U\cos\phi_u &= \frac{1}{2}[F_0(Q) + F_{90}(I)] \\ L\sin\phi_l &= \frac{1}{2}[F_0(I) + F_{90}(Q)] \\ L\cos\phi_l &= \frac{1}{2}[F_0(Q) - F_{90}(I)]. \end{aligned}$$

Physically, what the above equations say is that U and L rotate in opposite directions

with respect to the phase shifts of the front end local oscillator. Hence, the side bands can be separated.

Bibliography

[1] Beckmann, P. and Spizzichino, A. (1963). *The Scattering of Electromagnetic Waves from Rough Surfaces*, Pergamon Press, The Macmillan Company, N. Y. .

[2] Bennett, J. (1974). "Statistical Characterization of Mirror and Window Surfaces," *NBS Special Publication* **414**, *Laser Induced Damage in Optical Materials*, 157-162, edited by A. Glass and A. Guenther, US Department of Commerce.

[3] Bennett, J. (1976). "Measurement of the rms Roughness, Autocovariance function and other Statistical Properties of Optical Surfaces using a FECO Scanning Interferometer," *Applied Optics* **15**, 2705-2721.

[4] Bennett, J. and Merle Elson, J. (1977). "Surface Statistics of Selected Optical Materials," *NBS Special Publication* **509**, 142-156, *Laser Induced Damage in Optical Materials*, edited by A. Glass and A. Guenther, US Department of Commerce.

[5] Berg, N. and Lee, J. (1985). *Acousto-optics Signal Processing*, Marcel Dekker, Inc. , N. Y..

[6] Berge, G. L. private communication.

[7] Blum, E. J. (1959). *Ann. Astrophys.* **22**, 139.

[8] Borsuk, G. , (1981). "Photodetectors for Acousto-Optic Signal Processors," *Proc. IEEE* **69**, 100-118.

[9] Bowers, F. , and Klinger, R. (1973). "Quantization Noise of Correlation Spectrometers," *Astron. Astrophy. Suppl.* **15**, 373-380.

[10] Bowers, F. , Whyte, D. , Landecker, T. and Klinger, R. (1973). "A Digital Correlation Spectrometer Employing Multiple-Level Quantizatio," *Proc. IEEE* **61**, 1339-1343.

[11] Bracewell, R. (1965). *The Fourier Transform and Its Applications*, McGraw-Hill, Inc. , N. Y. 244-250.

[12] Brillouin, L. (1922). "Diffusion de la lumiére et des rayons X par in corps transparent homogêne," *Ann. Phys. (Paris), 9th ser.* **17**, 88-122.

[13] Burton, W. and Gordon, M. (1976). "The Morphology of Hydrogen and of other Tracers in the Galaxy," *Ann. Rev. Astron. Astroph.* **14**, 275.

[14] Burton, W. and Gordon, M. (1976). "CO in the Galaxy (III)," *Astron. Astroph.* **63**, 7-27.

[15] Chandley, P. and Welford, W. (1975). "A Re-formulation of some results of P. Beckmann for Scattering from Rough Surfaces," *Optical and Quantum Electronics* **7**, 393-397.

[16] Chandley, P. (1976a). "Surface Roughness Measurements from Coherent Light Scattering," *Optical and Quantum Electronics* **8**, 323-327.

[17] Chandley, P. (1976b). "Determination of the Autocorrelation Function of Height on a Rough Surface from Coherent Light Scattering," *Optical and Quantum Electronics* **8**, 329-333.

[18] Chang, I. (1977). "Tunable Acousto-Optic Filters: An Overview," *Opt. Eng.* **16**, 455-460.

[19] Chikada, Y. (1981). "Techniques for Spectral Measurements," *Nobeyama Radio Observatory Technical Report* **8**, Japan.

[20] Chikada, Y. , Ishiguro, M. , Hirabayashi, H . , Morimoto, M. , Morita, K. , Miyazawa, K. , Nagane, K. , Murata, K. , Tojo, A. , Inoue, S. , Kanzawa, T. , and Iwashita, H . (1984). "A digital FFT spectro-correlator for radio astronomy," *Indirect Imaging*, edited by Roberts, J. A. , Cambridge, London.

[21] Clancy, R. T. , Muhleman, D. O. and Jakosky, B. M. (1983). "Variability of Carbon Monoxide in the Mars Atmosphere," *Icarus* **55**, 282-301.

[22] Cole, T. (1968a). "Electro-Optic Spectrograph for Radio Astronomy," *Opt. Technol.* **1**, 31.

[23] Cole, T. (1968b). "Finite Sample Correlations of Quantized Gaussians," *Aust. J. Phys.* **21**, 273-282.

[24] Cole, T. (1973). "Electrooptical Radio Spectrograph," *Proc. IEEE* **61**, 1321-1323.

[25] Cole, T. (1974). "An Electro-Optical Spectrograph for Weak Signals," *Astron. Astrophys.* **34**, 149-151.

[26] Cooper, B. (1970). " Correlators With Two-bit Quantization," *Aust. J. Phys.* **23**, 521-527.

[27] Coppock, R. A. , Croce, R. F. , and Regier, W. L. (1978). "Bragg cell RF Signal Processing," *Microwave Journal*, Sep. , 1978.

[28] Debye, P. and Sears, F. (1932). "On the Scattering of Light by Supersonic Waves," *Proc. Nat. Academy of Science (USA)*, **18**, 409-414.

[29] Dicke, R. H. , 1946. *Rev. Sci. Instrm.* **17**, 268.

[30] Esepkina, N. , Petrun'kin, V. , Bukharin, N. , Kotov, B. and Kotov, Y. (1979). "Acousto-Optical Correlator Design for Processing Interferometric Signals for Radio Astronomy," *Soviet Tech. Phy. Lett. (USA)* **5**, 24-25.

[31] Evans, G. and Mcleish C. W. 1977. *RF Radiometer Handbook*, Artech House Inc. , Dedham, MA. .

[32] Ewen, H. I. and Purcell, E. M. (1951). *Nature (London)* **168**, 356.

[33] Formalont, E. and Wright, M. (1974). "Interferometry and Aperture Synthesis" in *Galactic and Extragalactic Radio Astronomy*, edited by G. L. Vershuur and K. I. Kellermann, Springer-verlag, N. Y. .

[34] Goodman, J. (1968). *Introduction to Fourier Optics*, McGraw-Hill, 1st edition, N. Y. .

[35] Gordon, M. and Burton, W. (1976). "CO in the Galaxy (I)," *Ap. J.* **208**, 346.

[36] Gradshteyn, I. and Ryzhik, I. (1965). *Table of Integrals, Series, and Products*, Academic Press, N. Y. .

[37] Grasse, C. and Brubaker, D. (1983). "Acousto-Optic Bragg cells speed EW Signal Processing," *Microwave System News*, Sep. , 1983.

[38] Gunn, J. and Westphal, J. (1981). "Care, feeding and use of Charge-coupled device (CCD) Imagers at Palomar Observatory," *Proc. SPIE* **290**, 16-23.

[39] Gursky, H. , Geary, J. , Schild, R. , Stephenson, T. and Weekes, T. (1981). "Astronomical Performance for the 512 x 320 RCA CCD," *Preprint* **1383**, Center for Astrophysics, Harvard College Observatory and Smithsonian Astrophysical Observatory.

[40] Harris, F. Private communication.

[41] Hawkins, D. G. (1980). "Resolution Criteria for Acoustooptic Deflectors," *Applied Optics* **19**, 186-187.

[42] Hecht, D. (1977). "Spectrum Analysis Using Acousto-Optic Devices," *Optical Engineering* **16**, 461-466.

[43] Ishimaru, I. (1978). *Wave Propagation and Scattering in Random Media*, **I & II**, Academic Press, N. Y. .

[44] Jackson, J. D. (1974). *Classical Electrodynamics*, John Wiley and Sons, 2nd edition, N. Y. .

[45] Jenkins, F. and White, H. (1976). *Fundamentals of Optics*, McGraw-Hill, 2nd edition, N. Y. .

[46] Kai, K. and Kosugi, T. (1979). "An Acousto-Optical Image Processor and Its Application To a 160MHz Interferometer," *Image Formation from Coherence Functions in Astronomy*, 165-172, edited by C. van Schooneveld, D. Reidel Publishing Company, Holland.

[47] Kaifu, N. and Ukita, N. (1978). "A high-resolution Acousto-optical Radiospectrometer for Millimeter-wave Astronomy," *Publ. Astron. Soc. Japan* **29**, 429.

[48] Kakar, R. K. and Walters, J. W. (1976). "Venus:Microwave Detection of Carbon Monoxide," *Science* **191**, 379-380.

[49] Kakar, R. K. , Walters, J. W. and Wilson, W. J. (1977). "Mars:Microwave Detection of Carbon Monoxide," *Science* **196**, 1090-1091.

[50] Kellman, P. , Shaver, H. and Murray, J. (1981). "Integrating Acousto-Optic Channelized Receiver," *Proc.IEEE* **69**, 93-100.

[51] Klein, W. and Cook, B. (1967). "Unified Approach to Ultrasonic Light Diffraction," *IEEE Trans. on Sonics and Ultrasonics* **SU-14**, 123-134.

[52] Korpel, A. (1981). "Acousto-Optics – A Review of Fundamentals," *Proc.IEEE* **69**, 48-53.

[53] Kremer, I. , Golub, V. and Nakhmanson, G. (1979). "Internal Noise Sources in Acoustic-optical Devices for Radio Signal Processing," *Radio Phys. and Quantum Electronics (USA)* **22**, 588-592.

[54] Lambert, L. (1962). "Wide-band, Instantaneous Spectrum Analyzers employing Delay-Line Light Modulator," *IRE National Convention Record* **10**, part 6, 69-78.

[55] Lawrence, R. and Strohbehn, J. (1970). "A Survey of Clear-air Propagation Effects Relevant to Optical Communications," *Proc.IEEE* **58**, 1523-1545.

[56] Leighton, R. B. (1978). *Final Technical Report for National Science Foundation Project* **AST 73-04908**, Caltech, CA.

[57] Lo, K. Y. , Berge, G. L. , Claussen, M. J. , Heiligman, G. M. , Leighton, R. B. , Masson, C. R. , Moffet, A. T. , Phillips, T. G. , Sargent, A. I. , Scott, S. L. , Wannier, P. G. , Woody, D. P. (1984). "Aperture Synthesis Observation of CO emission from the nucleus of IC342 ," *Ap. J.* **282**, L59.

[58] Lo, K. Y. , Cheung, K. W. , Masson, C. R. , Phillips, T. G. , Woody, D. P. (1984). "Aperture Synthesis Observation of CO emission from M82 ," *ESO Proceedings of Workshop on (Sub)millimeter-wave Astronomy*, Aspenas, Sweden, June, 1985.

[59] Lo, K. Y. , Cheung, K. W. , Masson, C. R. , Phillips, T. G. , Scott, S. L. , Woody, D. P. (1987). "Molecular Gas in the Starburst Nucleus of M82," *Ap. J.* **312**, 574-591.

[60] Lutomirski, R. (1979). "Atmospheric Effects on Optical Coherence," *Proc. SPIE* **194**, Applications of Optical Coherence, 122-128.

[61] Masson, C. (1979). Unpublished report, OVRO, Caltech, CA.

[62] Masson, C. (1980). "The Design of Stable Acousto-Optical Spectrometers for Radio Astronomy," *Proc. SPIE* **231**, 291.

[63] Masson, C. (1982). "A Stable Acousto-Optical Spectrometer for Millimeter Radio Astronomy," *Astron. Astrophys.* **114**, 270-274.

[64] Masson, C. R. , Cheung, K. W. , Berge, G. L. , Claussen, M. J. , Heiligman, G. M. , Leighton, R. B. , Lo, K. Y. , Masson, C. R. , Moffet, A. T. , Phillips, T. G. , Sargent, A. I. , Scott, S. L. , Woody, D. P. (1984). "High Resolution CO Observation of NGC7027 ," *Ap. J.* **292**, 464-470.

[65] Melles Griot, (1985). *Optics Guide* **3**, Melles Griot, CA, USA.

[66] Milne, D. and Cole, T. (1979). "A Broad Band Radio Astronomy Spectrograph," *Proc. IREE Aust.* Mar. 1979, 44-47.

[67] Moffet, A. T. (1984). "Arrangement of Expanded Filter Banks," *Internal Memo*, OVRO, Caltech, CA.

[68] Muhleman, D. O. and Berge, G. L. (1982). "Microwave Emission from Saturn's Ring," *I. A. U. Colloquium* **75**.

[69] Muhleman, D. O. , Berge, G. L. and Clancy, R. T. (1984). "Microwave Measurements of Carbon Monoxide on Titan," *Science* **223**, 393-396.

[70] Napier, P. J. and Crane, P. C. (1982). In Lecture 3 of *Synthesis Mapping, Proceedings of the NRAO-VLA workshop held at Socorro, New Mexico, June 21-25, 1982*, edited by A. R. Thompson and L. R. D'Addario, NRAO.

[71] Newport Corporation, (1986). *Newport Corporation 1986-87 Catalog*, Newport Corporation, CA, USA.

[72] Ohm, E. A. and Snell, W. W. (1963). *Bell Syst. Tech. J.* **42**, 2047.

[73] Orhaug, T. and Waltman, W. (1962). *Publ. Nat. Radio Astron. Observ.* **1**, 179.

[74] Penfield, H. (1976). "Multichannel-Filter Spectrometers," in *Methods of Experimental Physics* **12**, part B, edited by M. L. Meeks, Academic Press, N. Y. .

[75] Penndorf, R. (1957). "Tables of the Refractive Index for Standard Air and the Rayleigh Scattering Coefficient for the Spectral Region between 0. 2 and 20. 0 μ, and their Application to Atmospheric Optics," *J. Opt. Soc. Am.* **47**, 1010-1015.

[76] Pinnow, D. (1971). "Acousto-optic Light Deflection: Design Consideration for First Order Beam Steering Transducers," *IEEE Transactions on Sonics and Ultrasonics* **SU-18**, 209-214.

[77] Randolph, J. and Morrison, J. (1971). "Rayleigh-Equivalent Resolution of Acoustooptic Deflection Cells," *Applied Optics* **10**, 1453-1454.

[78] RCA Internal documentation on CCD (1980).

[79] Rogers, A. (1970). "Very Long Baseline Interferometry with Large Effective Bandwidth for Phase-delay Measurements," *Radio Science* **5**, 1239-1247.

[80] Rogers, A. (1976). "Theory of Two-element Interferometers," in *Method of Experimental Physics* **12**, Astrophysics, Part C, Radio Observations, edited by M. L. Meeks, Academic Press.

[81] Robinson, B. (1982). "Wideband Spectrometers for Millimeter Wavelengths," in *Interstellar Molecules I.A.U. Symp.* 84.

[82] Ruze, J. (1966). *Proc.IEEE* **54**, 633-640.

[83] Ryle, M. and Vonberg, D. D. (1948). *Proc. Roy. Soc. London A* **193**, 98.

[84] Scoville, N. and Solomon, P. (1975). "Molecular Clouds in the Galaxy," *Ap. J.* **199**, L105-109.

[85] Scoville, N. and Young, J. (1983). "The Molecular Gas Distribution in M51," *Ap. J.* **265**, 148-165.

[86] Steinberg, J. L. (1952). *Onde Elec.* **32**, 519.

[87] Tatarski, V. (1961). *Wave Propagation in a Turbulent Medium*, McGraw-Hill, N. Y. .

[88] Tatarski, V. (1971). *The Effects of the Turbulent Atmosphere on Wave Propagation, U. S. Department of Commerce*, **TT-68-50464**, Springfield, Virginia.

[89] Thompson, A. R. , Moran, J. M. and Swenson Jr. , G. W. (1986). *Interferometry and Synthesis in Radio Astronomy*, Wiley, N. Y. .

[90] Yariv, A. and Yeh, Pochi (1984). *Optical Waves in Crystals*, John Wiley and Sons, Inc. , N. Y. .

[91] Yaroshenko, V. (1964). *Radiotechnica* **7**, 749.

[92] Young, E. and Yao, S. (1981). "Design Considerations for Acousto-Optic Devices," *Proc. IEEE* **69**, 54-64.

[93] Uchida, N. and Niizeki, N. (1973). "Acoustooptic Deflection Materials and Techniques, " *Proc. IEEE* **61**, 1073-1092.

[94] Weinreb, S. (1963). M. I. T. Research Laboratory of Electronics Report **412**, 119pp.

[95] Weinreb, S. (1984). "Analog-filter, digital-correlator hybrid spectrometer ," NRAO Electronics Div. Internal Report **248**.

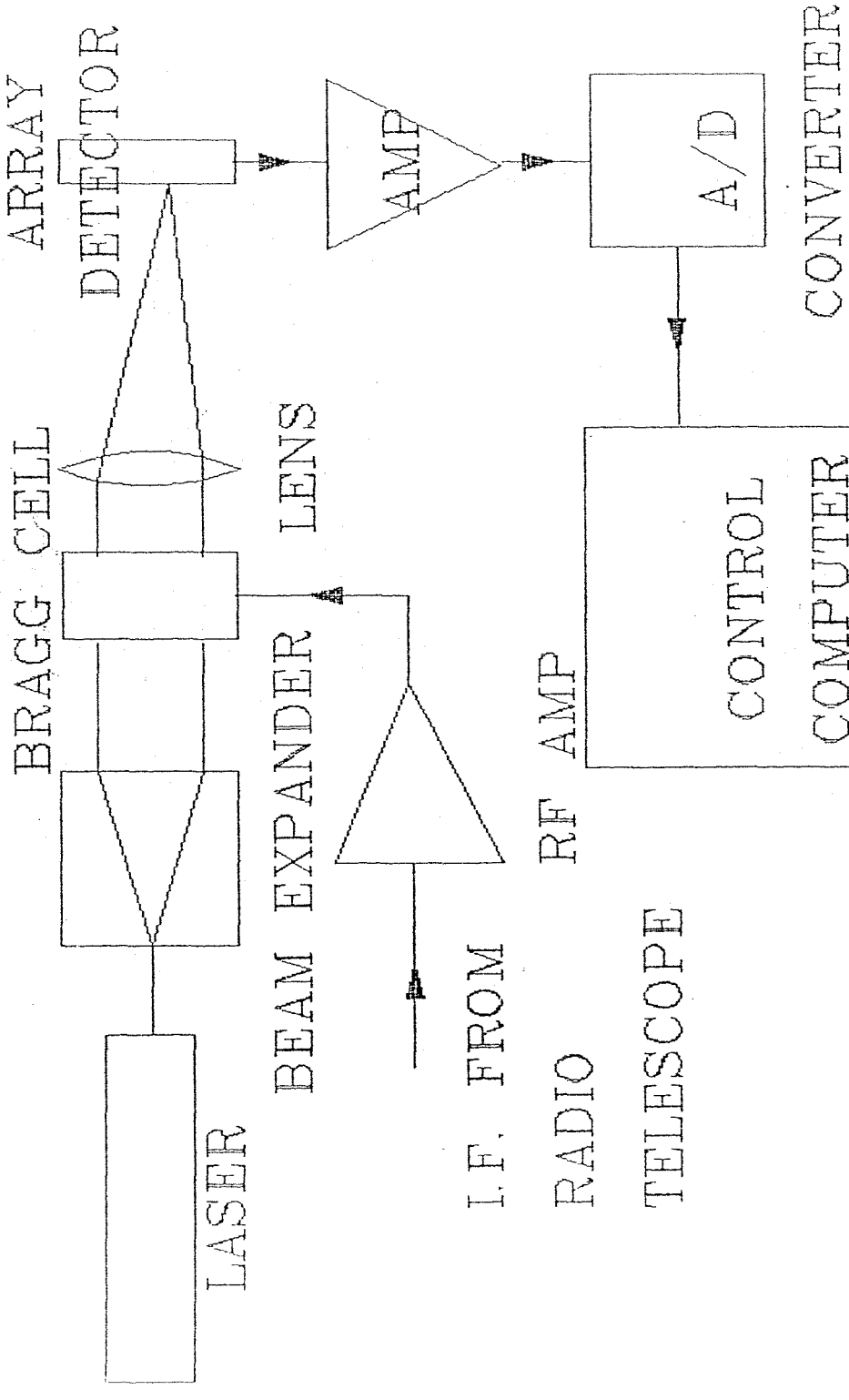

Fig. 2—1 Single channel AOS

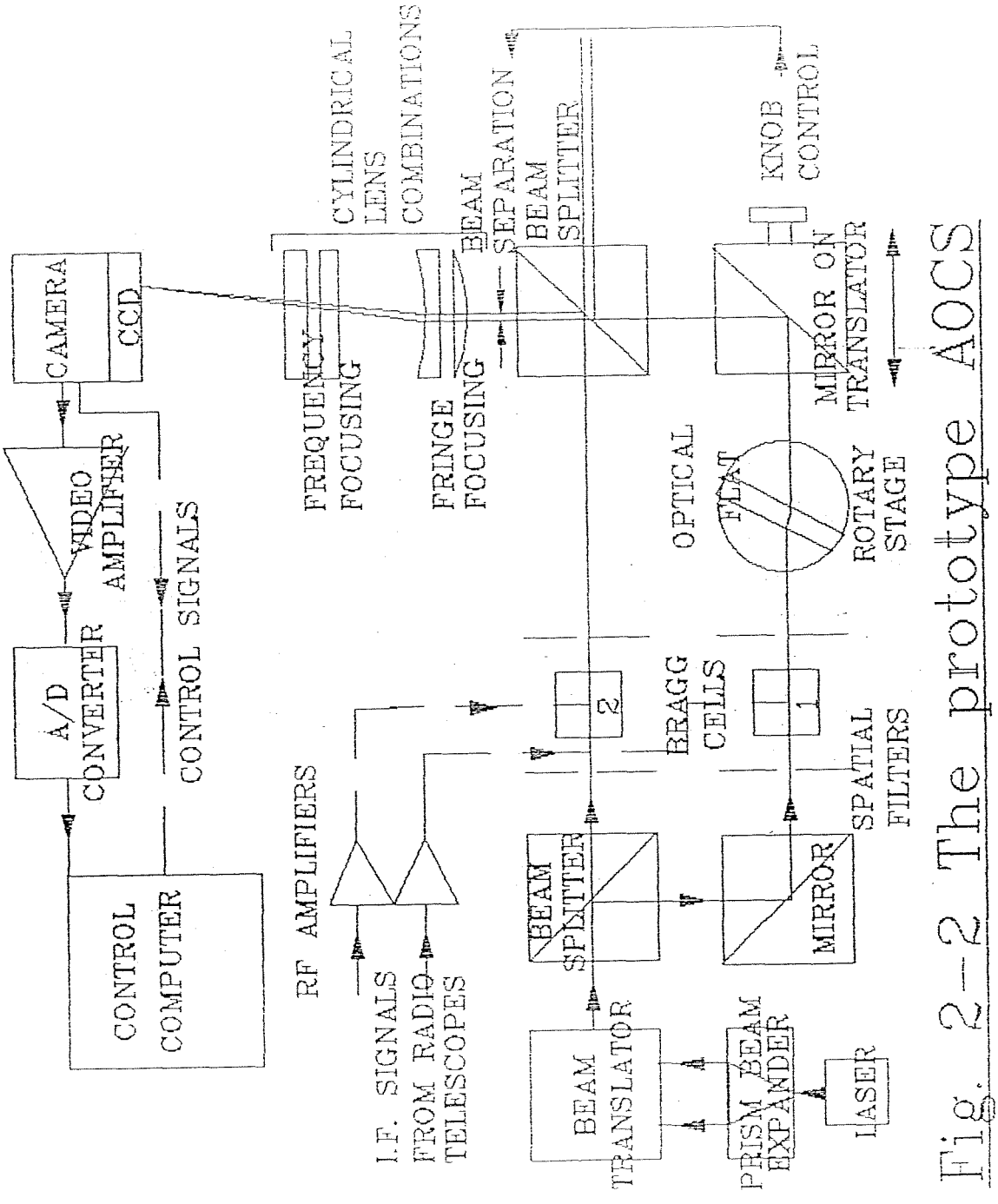

Fig. 2-2 The prototype AOCS

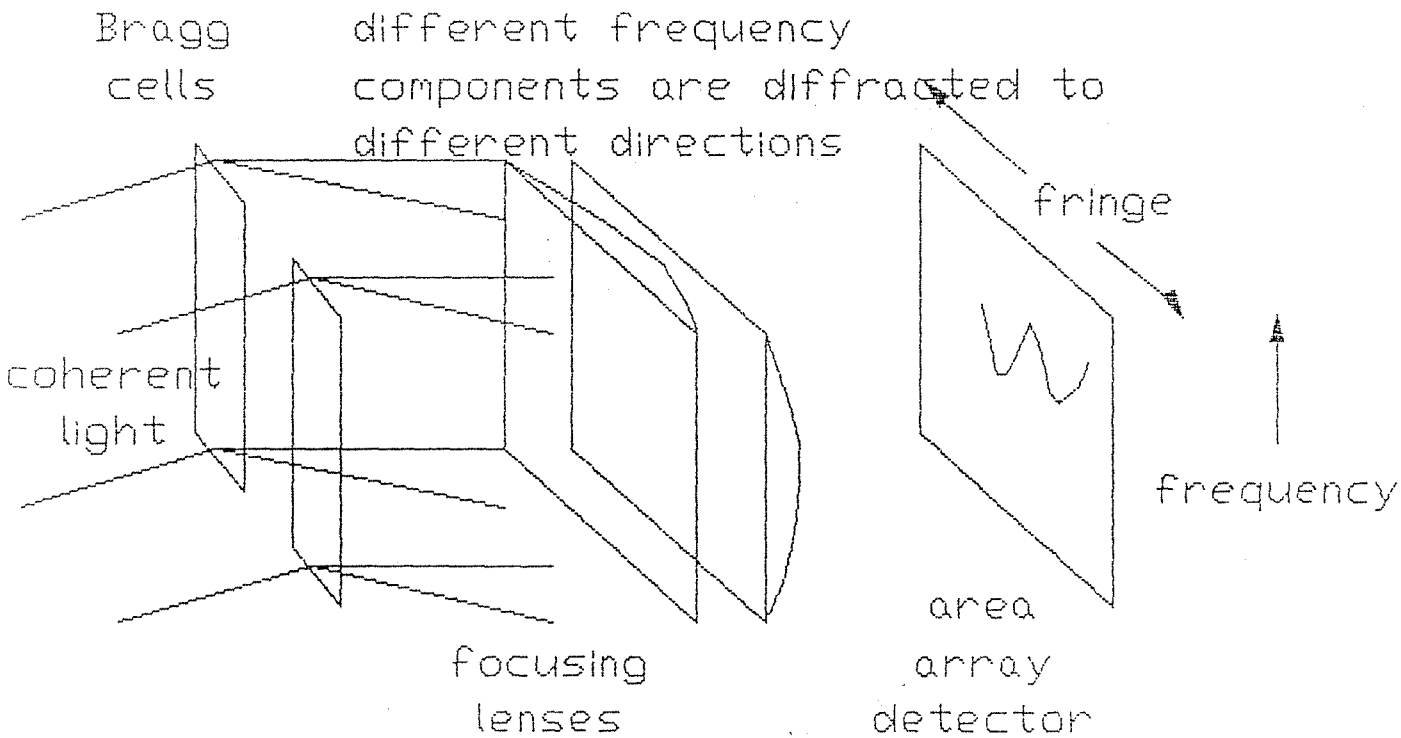

Fig.2-3 Geometry of the A□CS

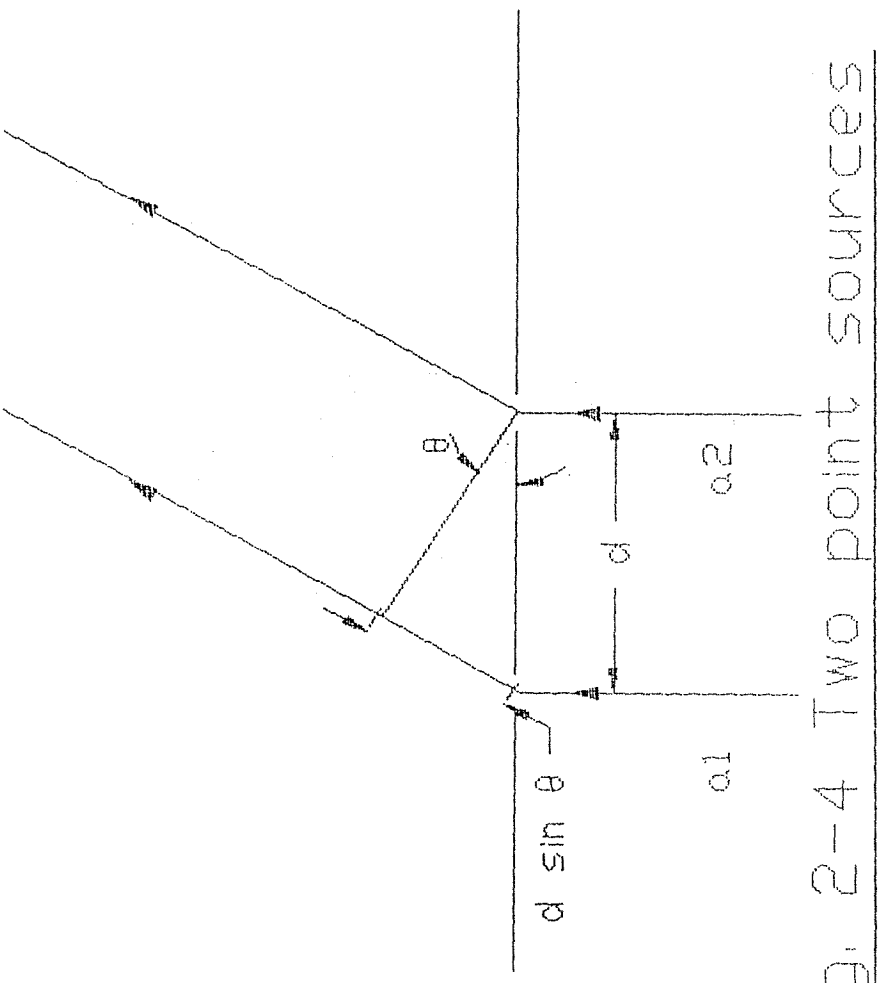

Fig. 2-4 Two point sources

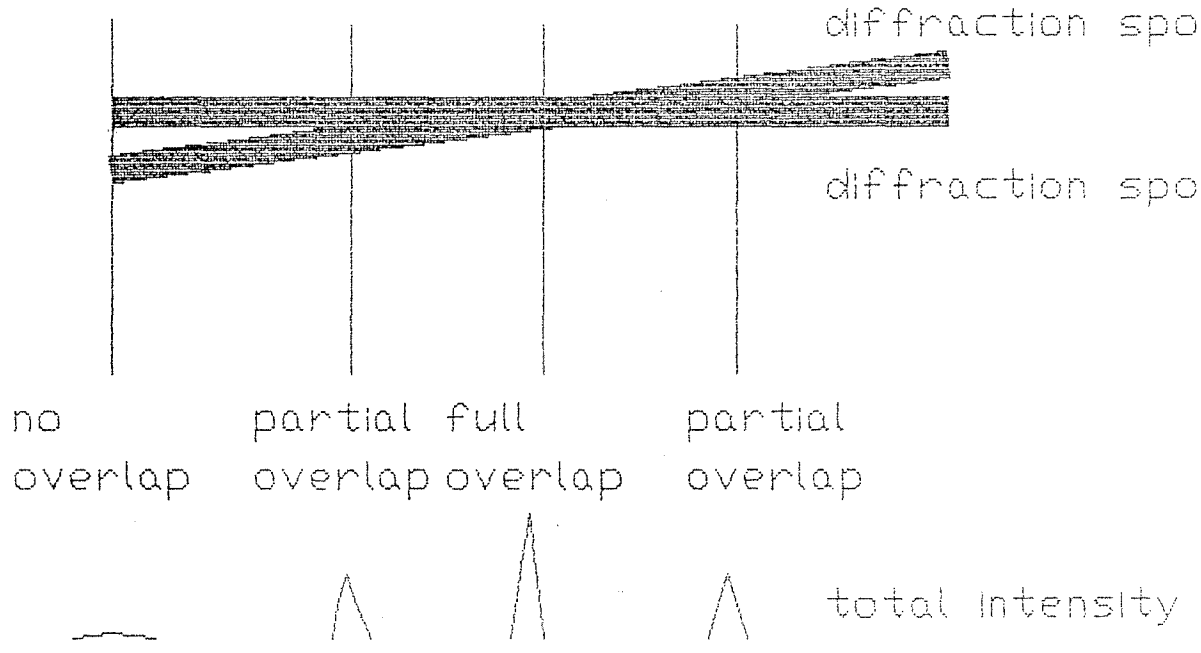

Fig. 3-1 Tilted alignment degrades resolution

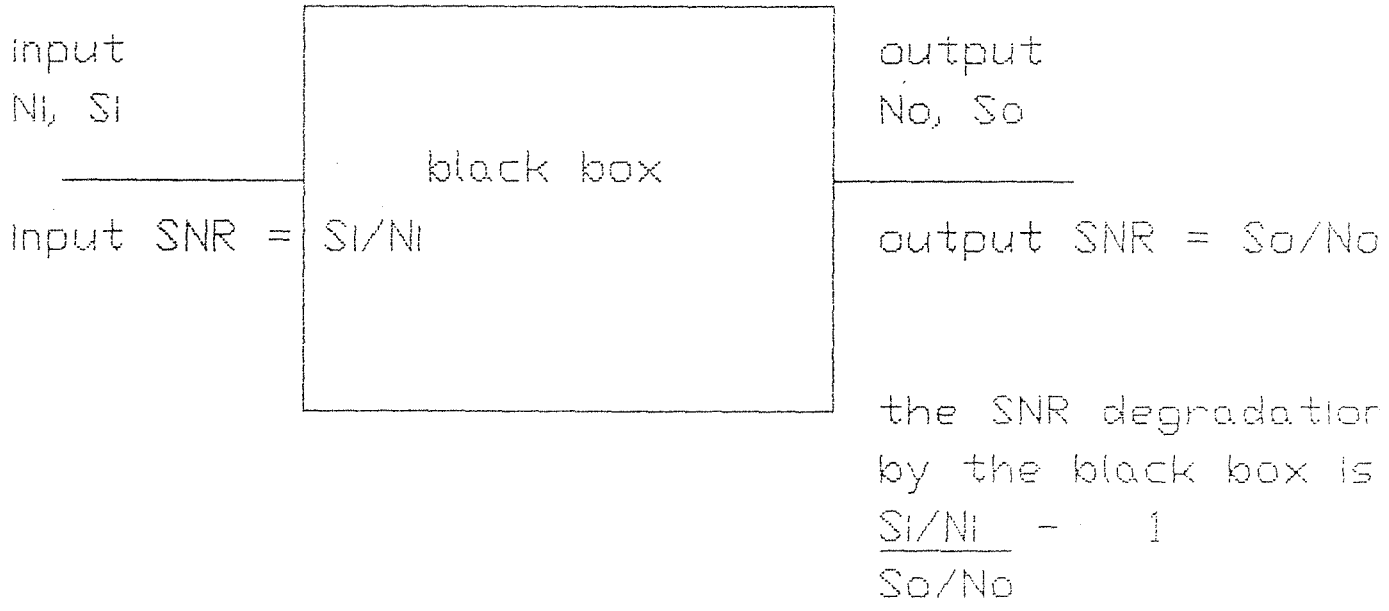

Fig. 3-2 The black box model

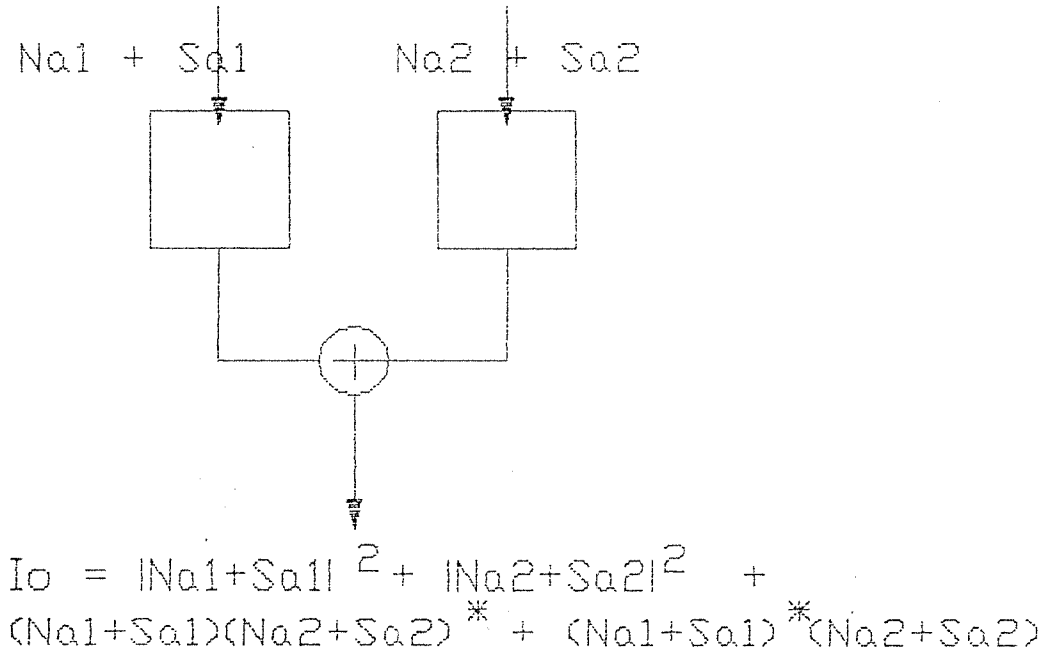

Fig. 3-3 Simplified representation of A□CS for SNR analysis

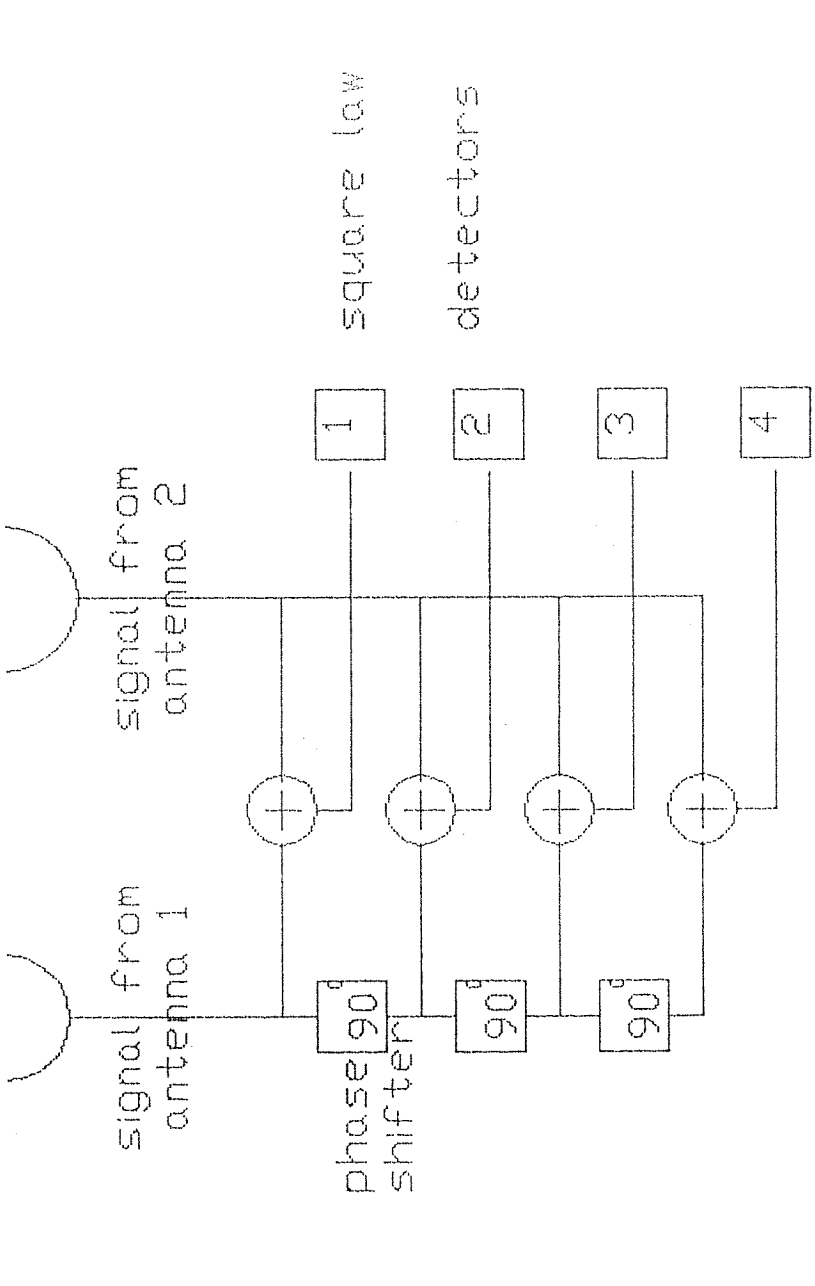

Fig. 3-4 Equivalent representation of ADCS

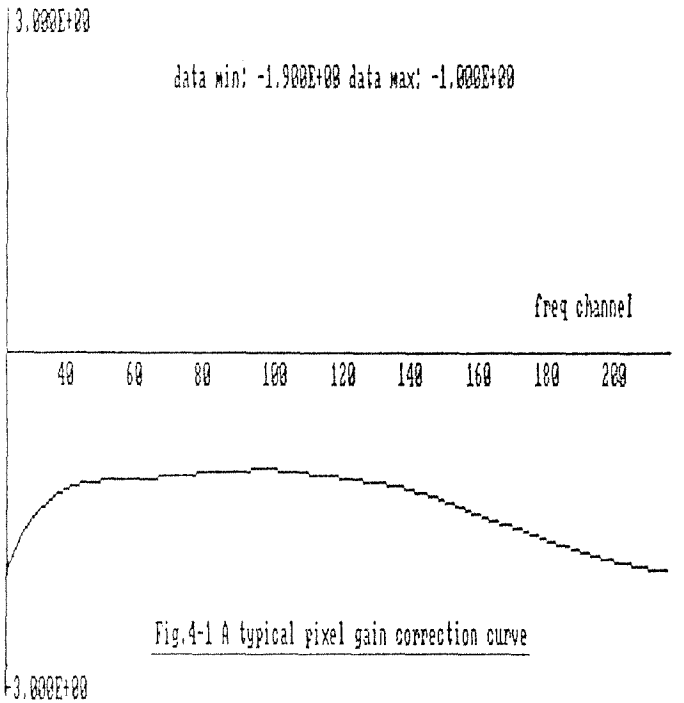

Fig.4-1 A typical pixel gain correction curve

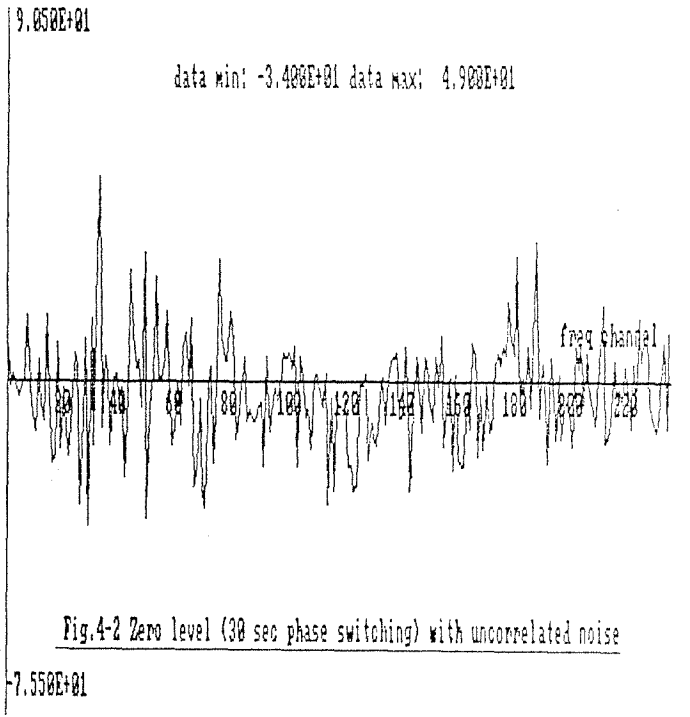

Fig.4-2 Zero level (30 sec phase switching) with uncorrelated noise

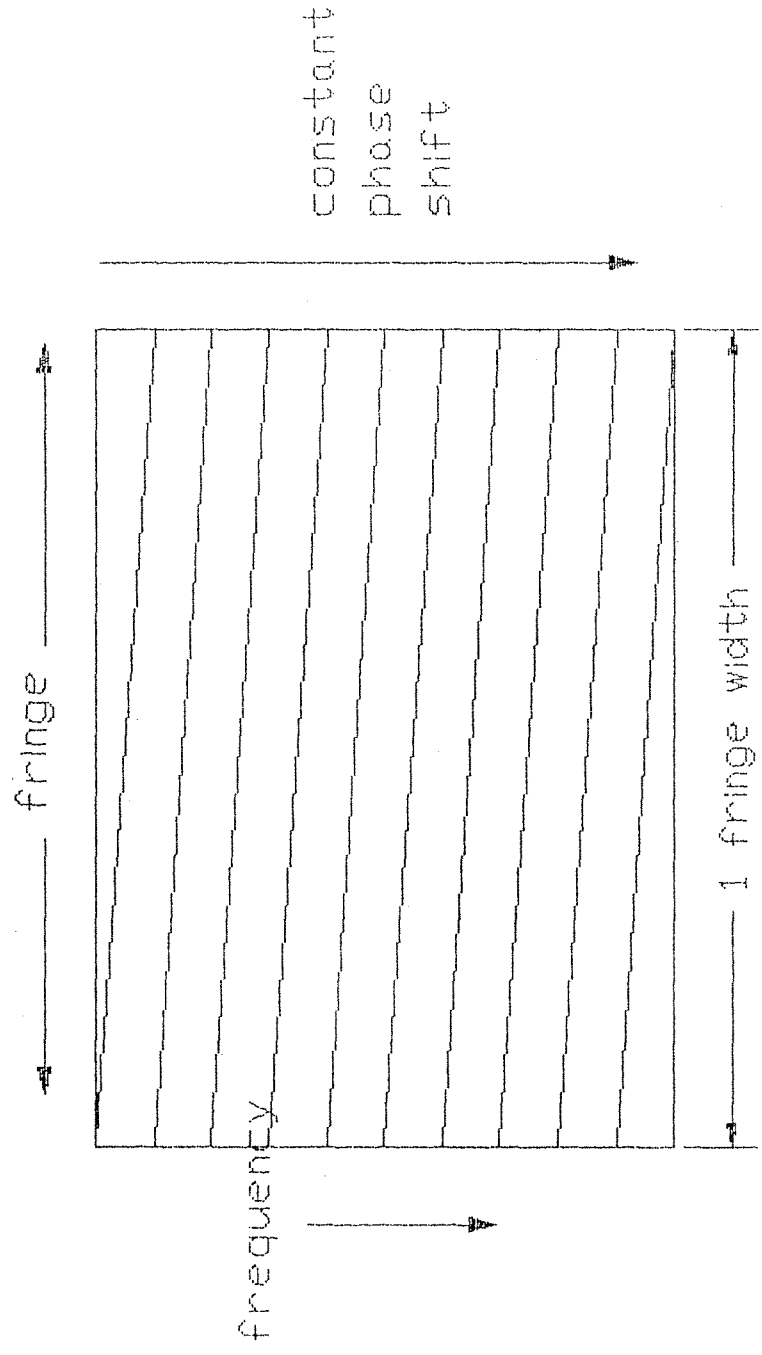

Fig. 4-3 Fringe pattern of correlated noise input

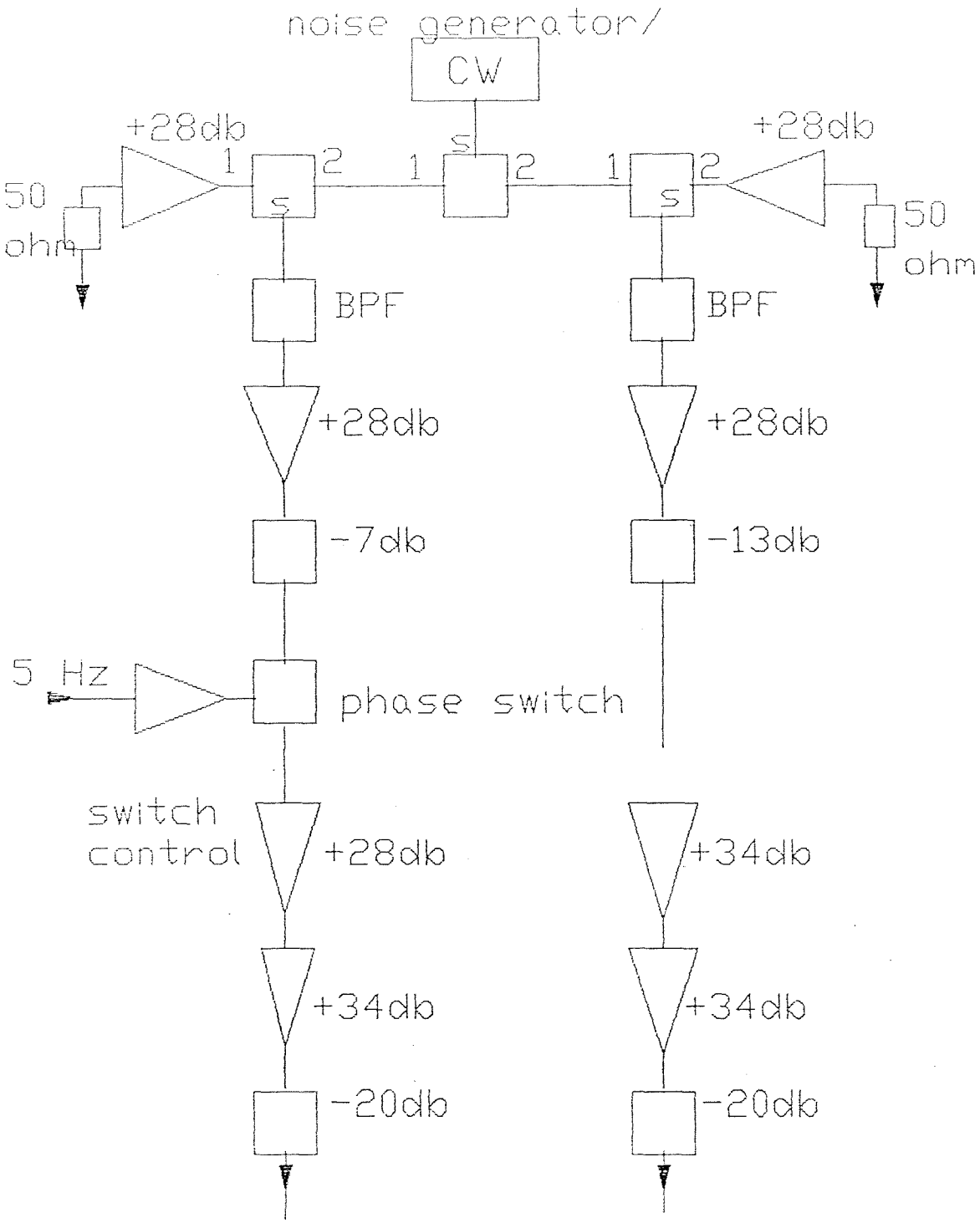

Fig.4-4 Noise generator

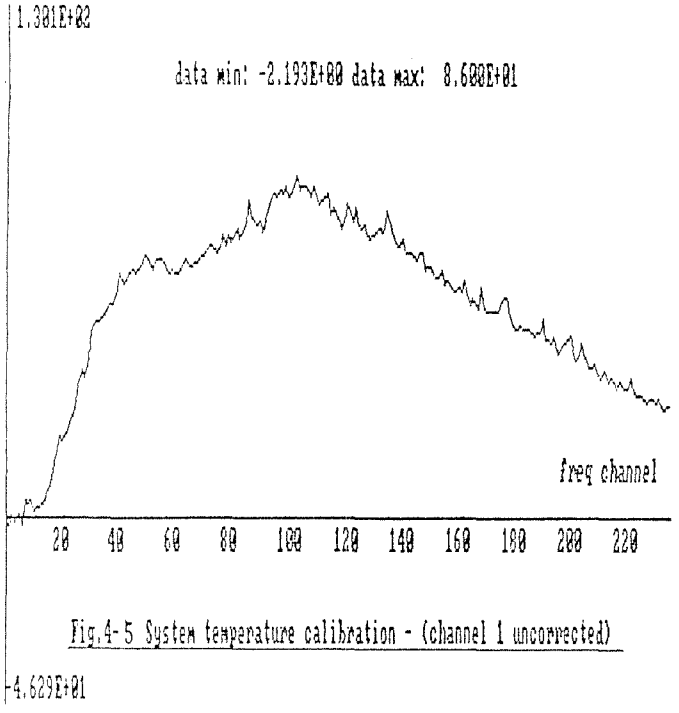

Fig.4-5 System temperature calibration - (channel 1 uncorrected)

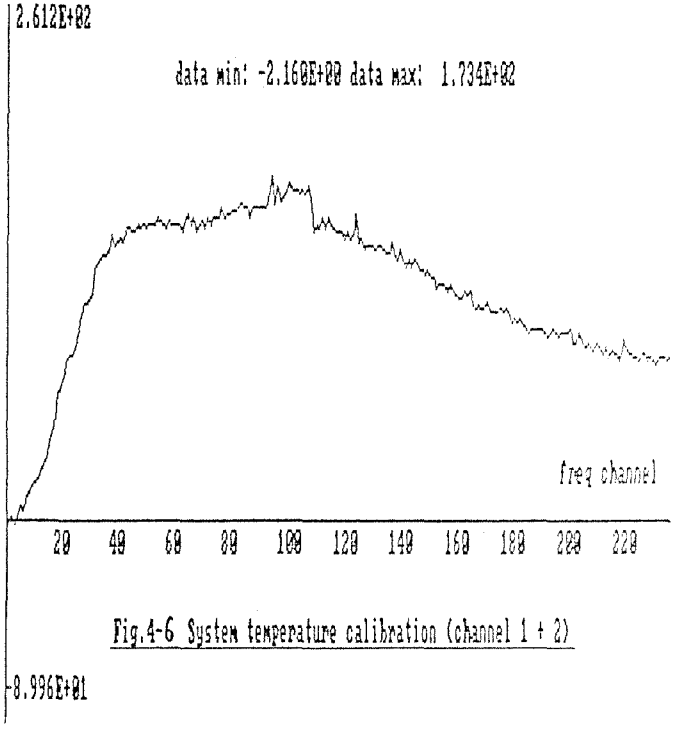

Fig.4-6 System temperature calibration (channel 1 + 2)

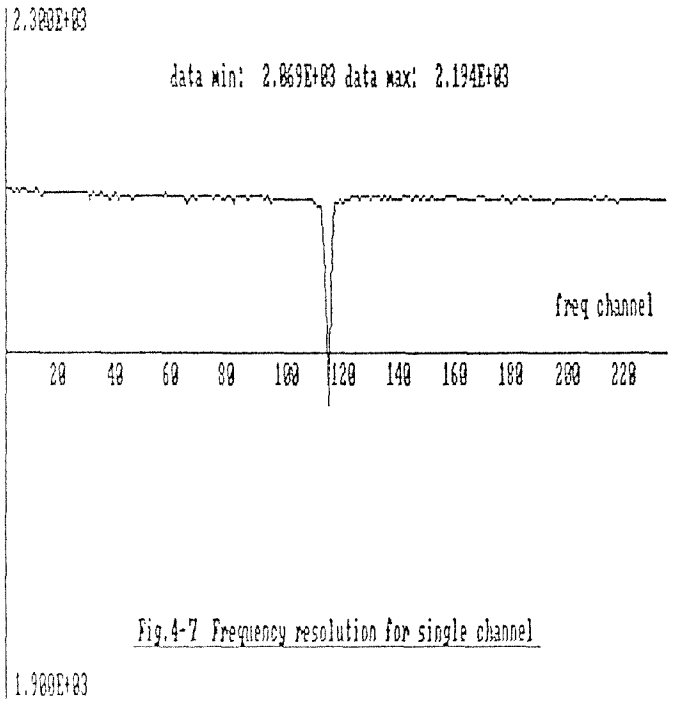

Fig.4-7 Frequency resolution for single channel

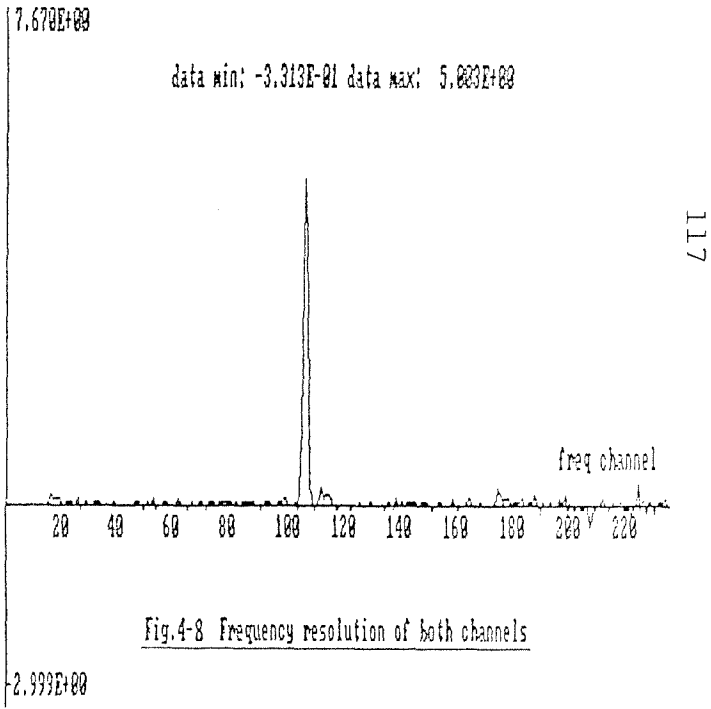

Fig.4-8 Frequency resolution of both channels

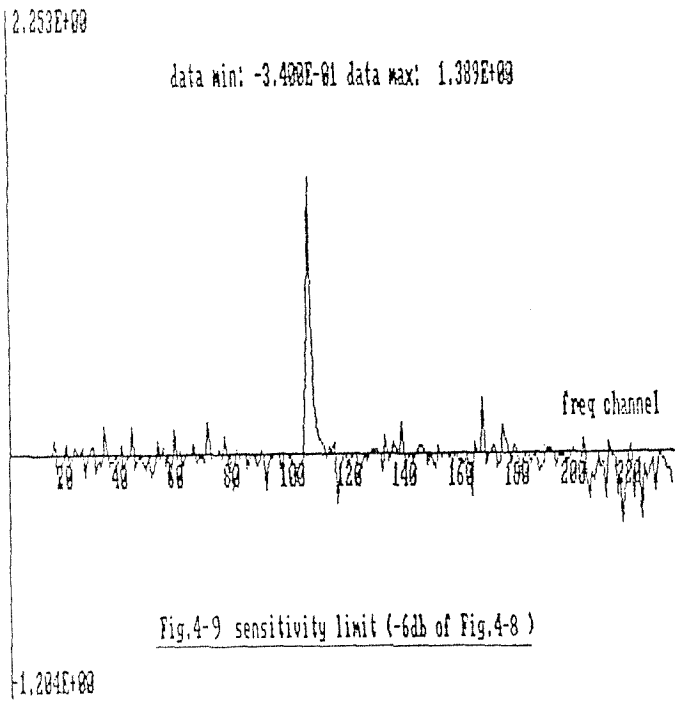

Fig.4-9 sensitivity limit (-6db of Fig.4-8)

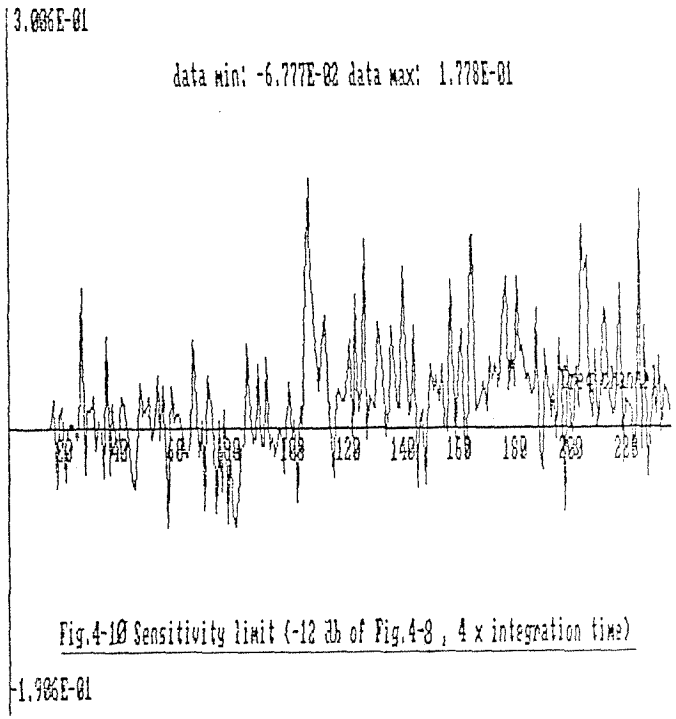

Fig.4-10 Sensitivity limit (-12 db of Fig.4-8 , 4 x integration time)

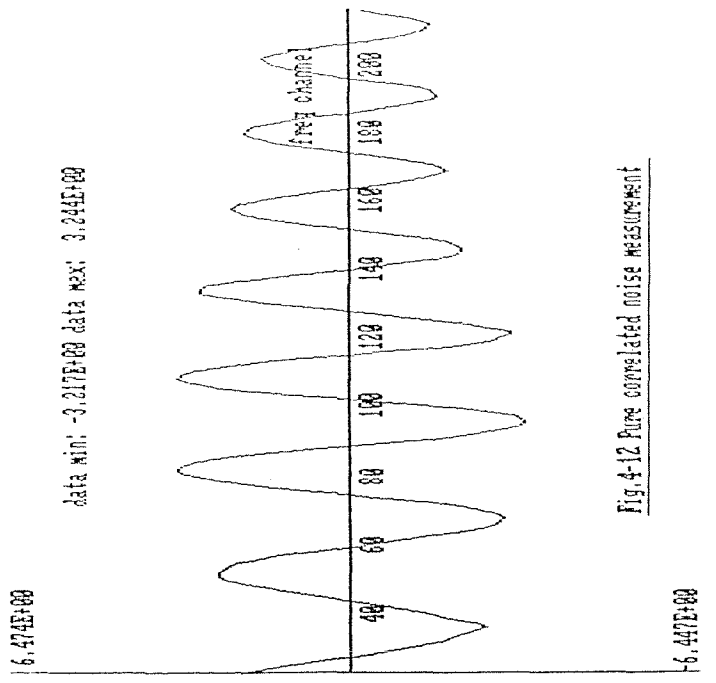

Fig.4-12 Pure correlated noise measurement

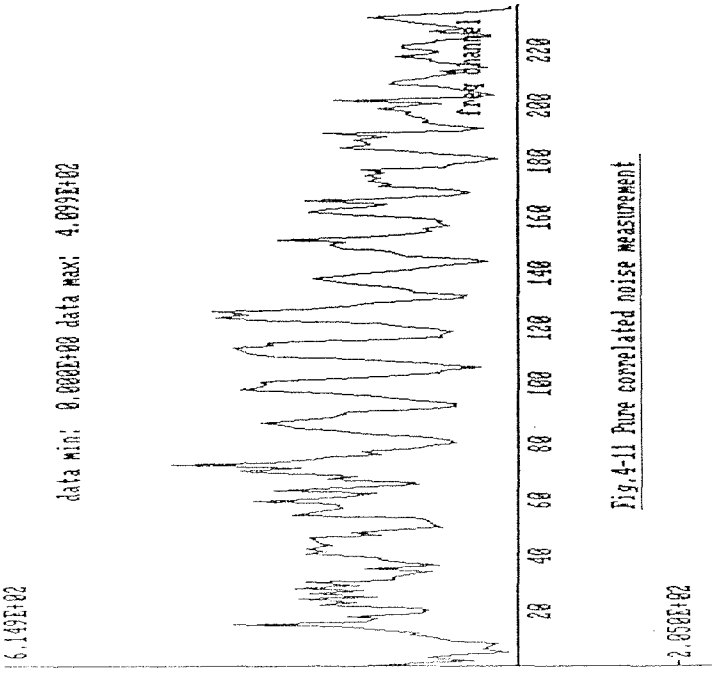

Fig.4-11 Pure correlated noise measurement

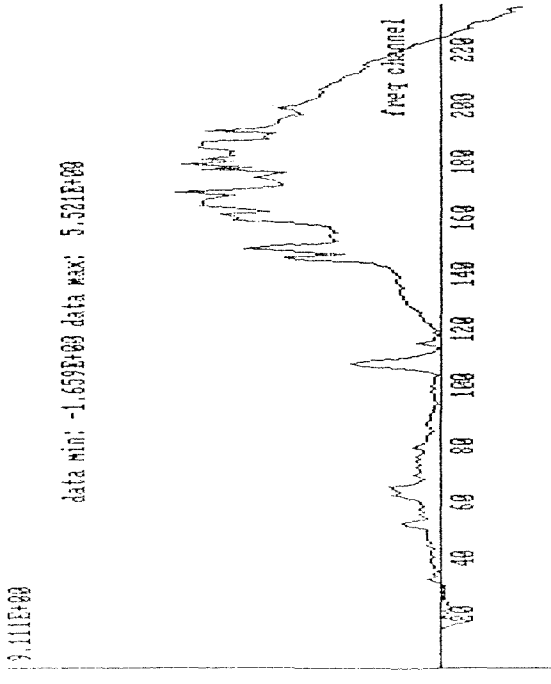

Fig.4-13 CW with uncorrelated noise

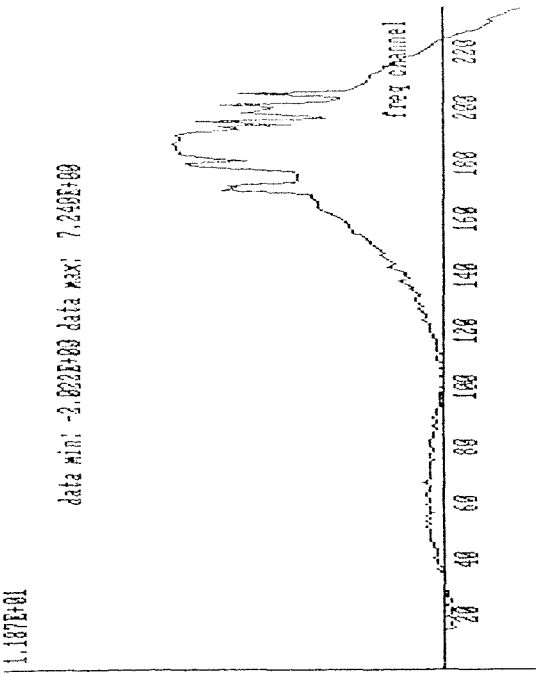

Fig.4-14 Phase switched channel mismatch

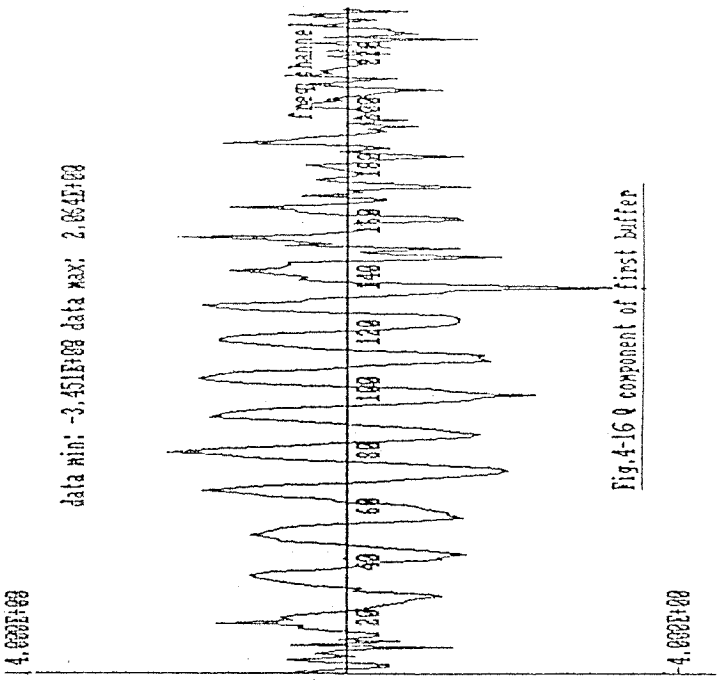

Fig.4-16 Q component of first buffer

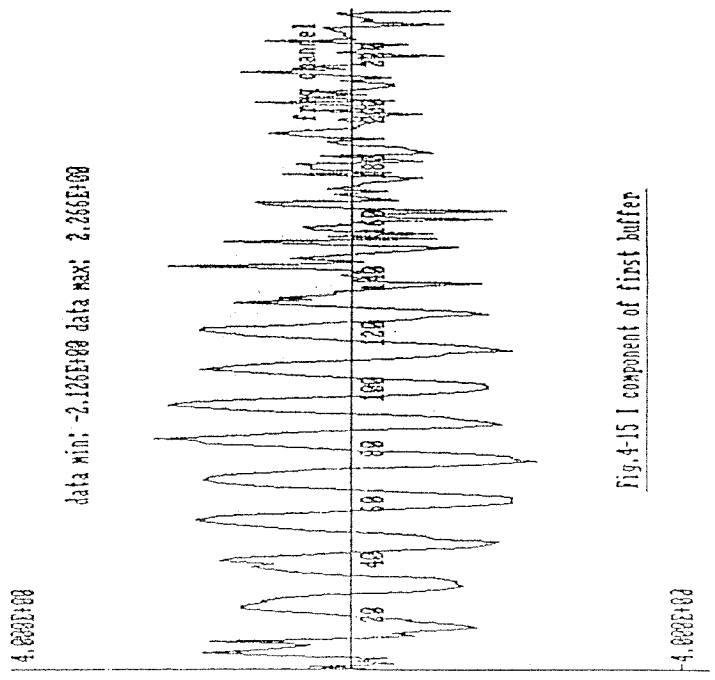

Fig.4-15 I component of first buffer

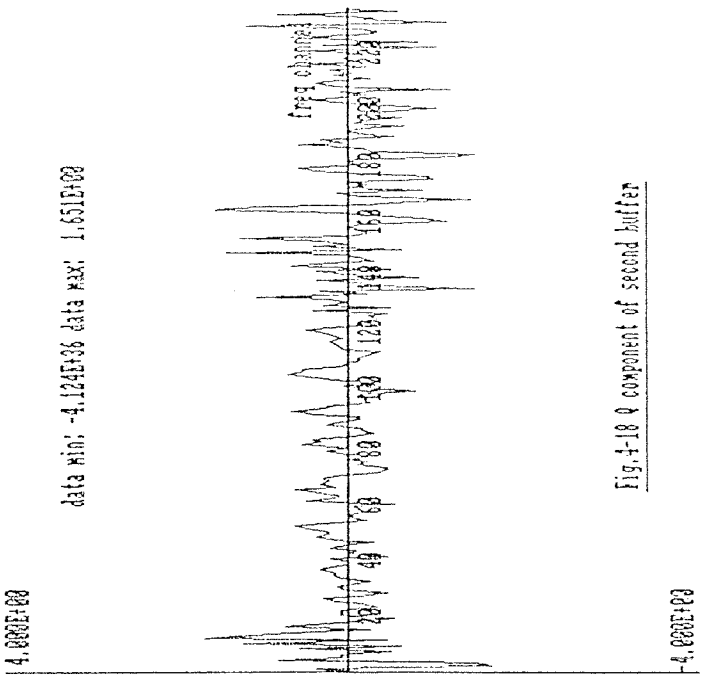

Fig.4-18 Q component of second buffer

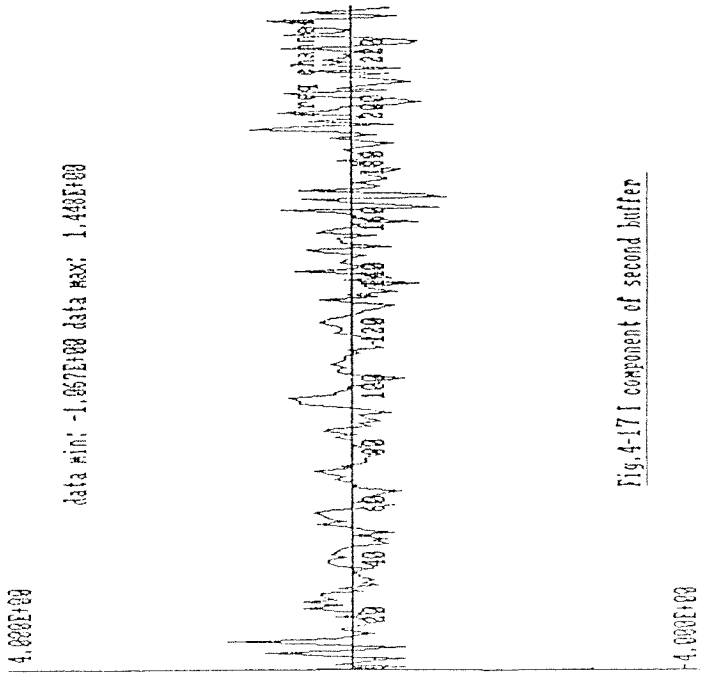

Fig.4-17 I component of second buffer

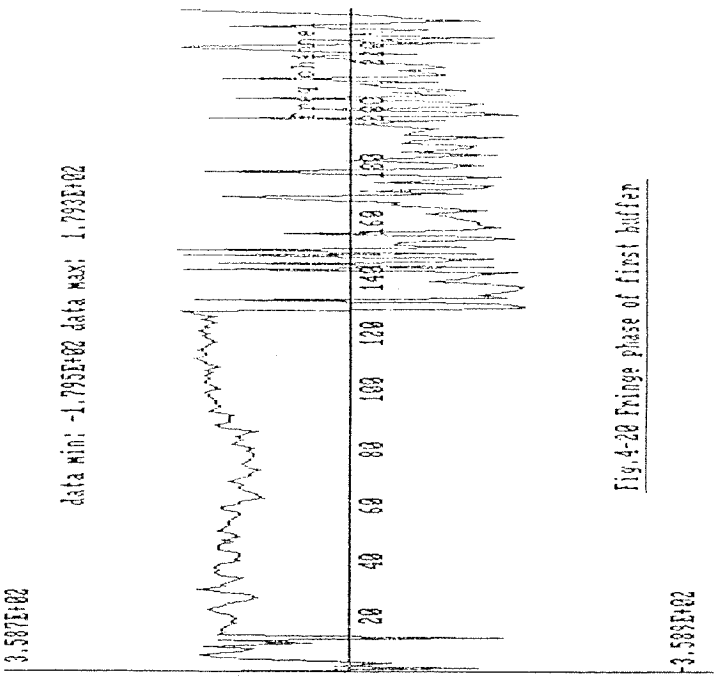

Fig.4-20 Fringe phase of first buffer

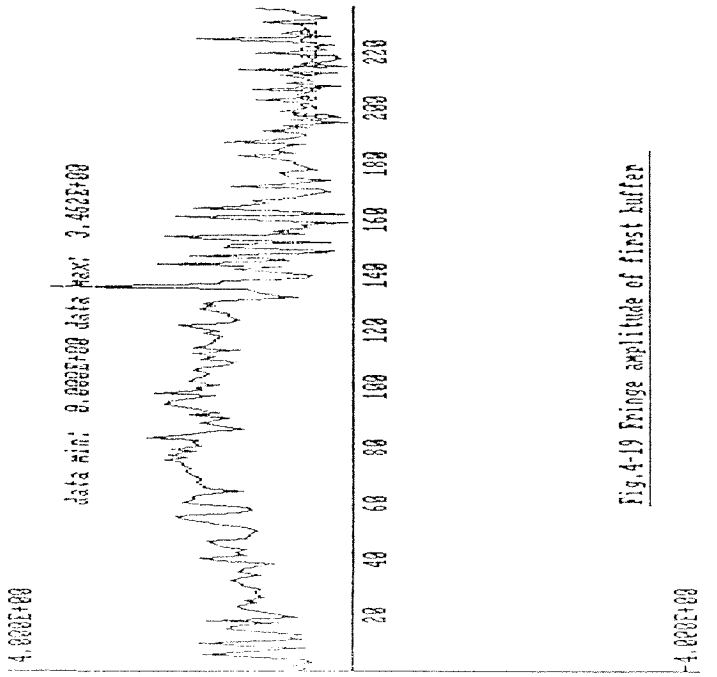

Fig.4-19 Fringe amplitude of first buffer

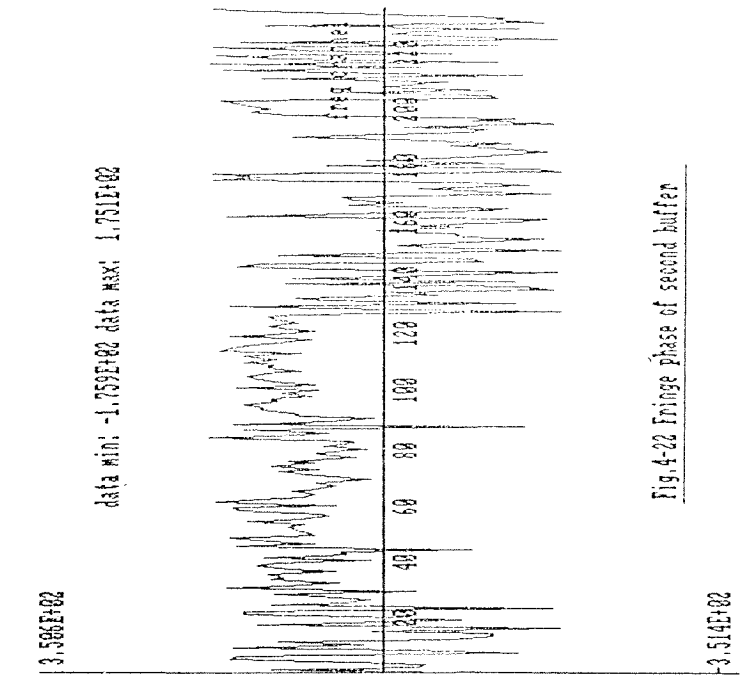

Fig.4-22 Fringe phase of second buffer

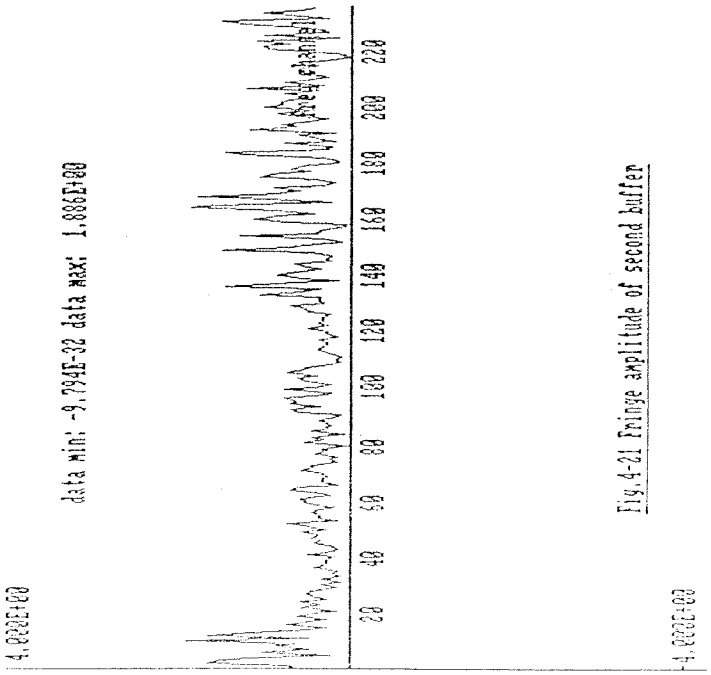

Fig.4-21 Fringe amplitude of second buffer

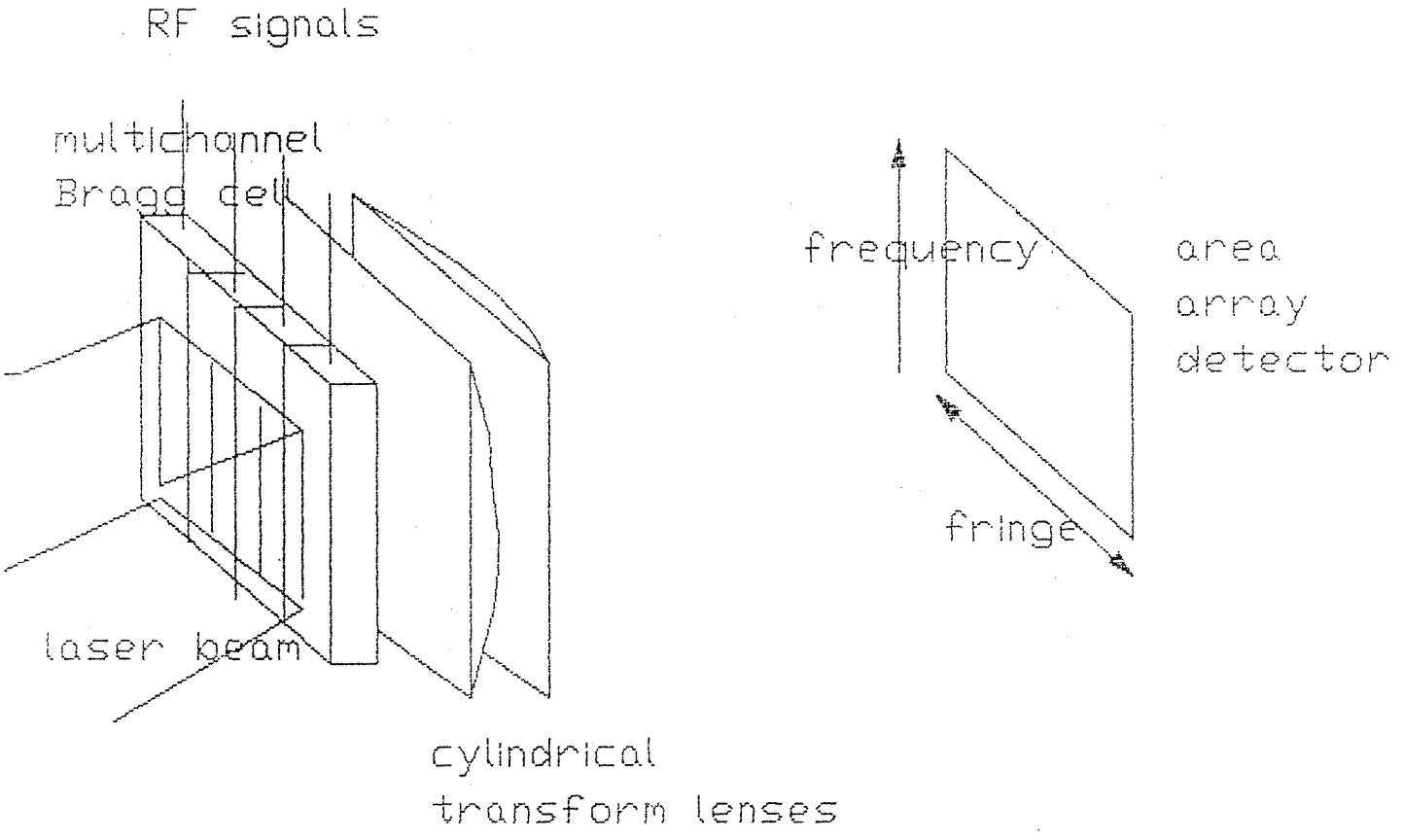

Fig. 5-1 Expanding the A□CS (I)
(Interfering A□CS)

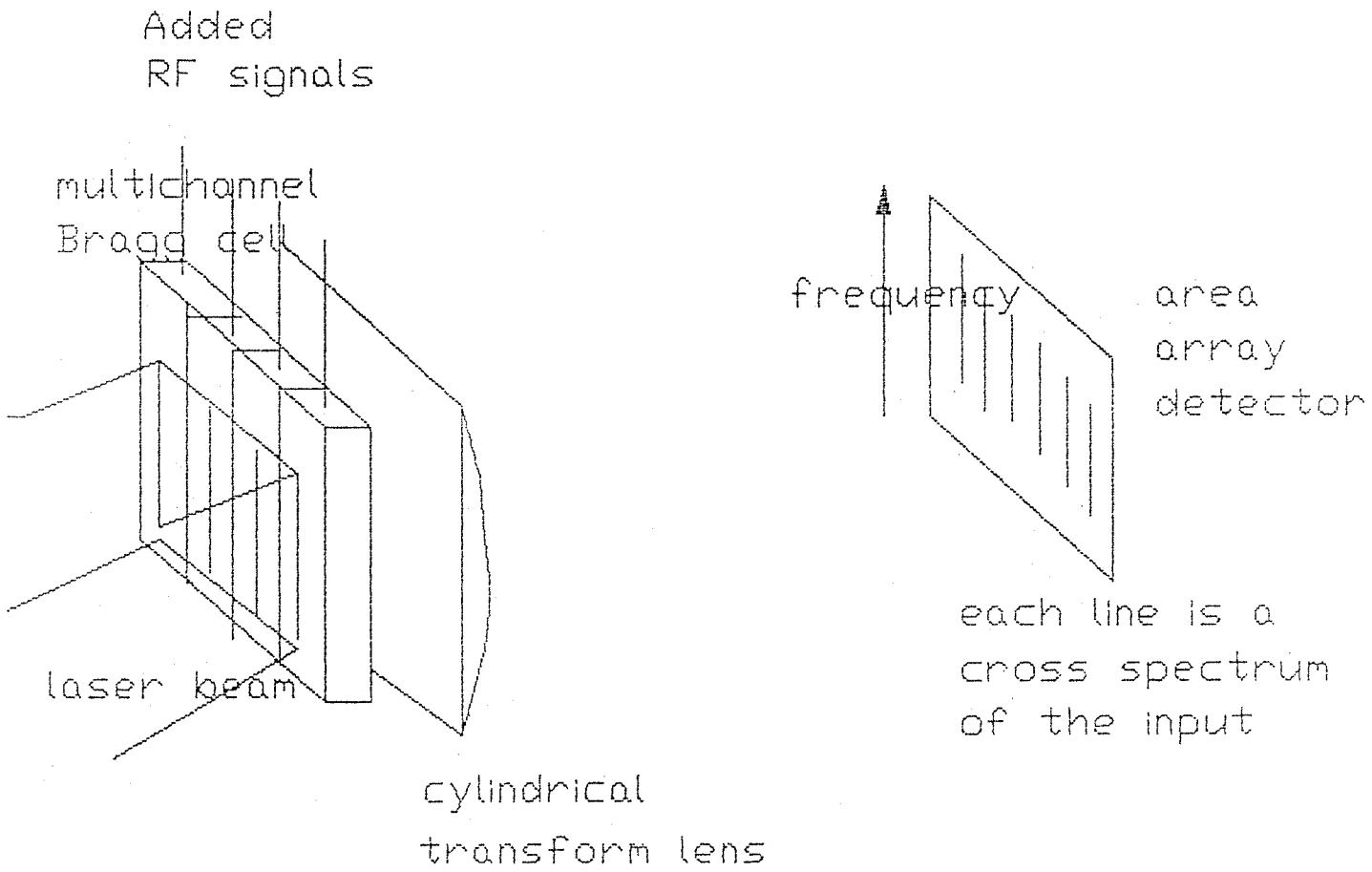

Fig. 5-2 Expanding the A□CS (II)

(Adding A□CS)

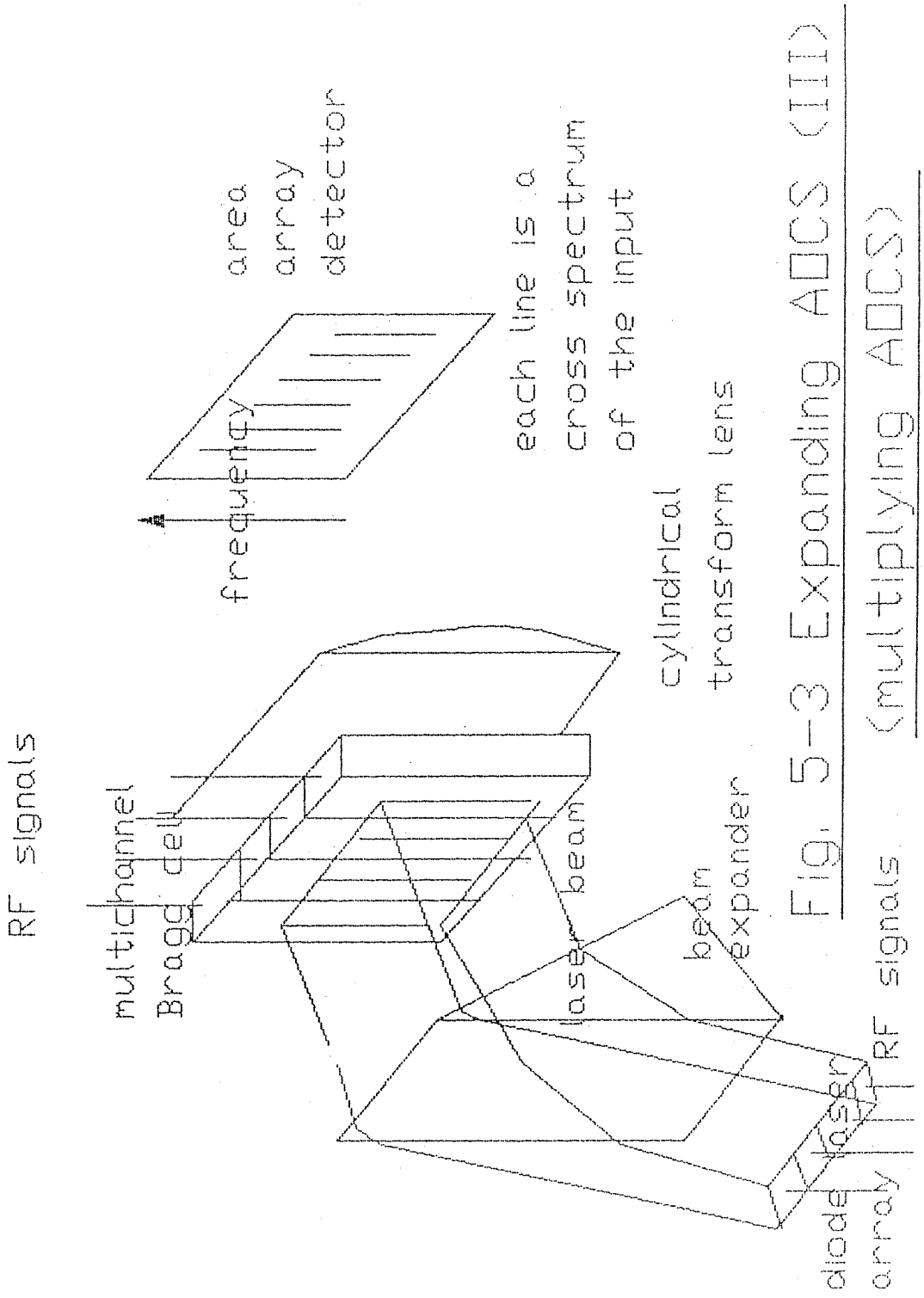

Fig. 5-3 Expanding ADCS (III)
(multiplying ADCS)

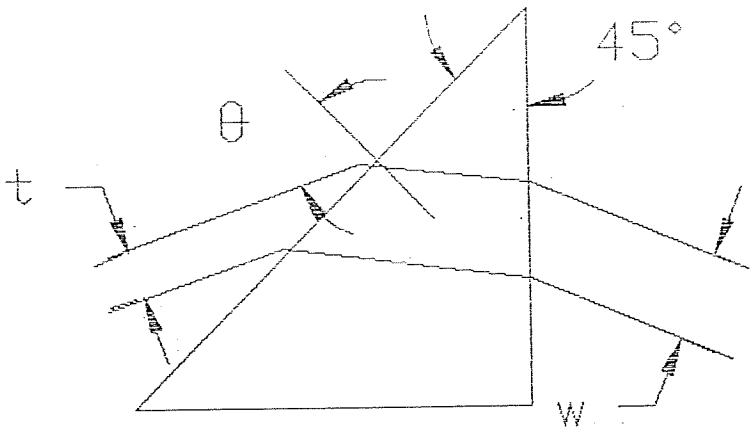

w/t prism beam expander

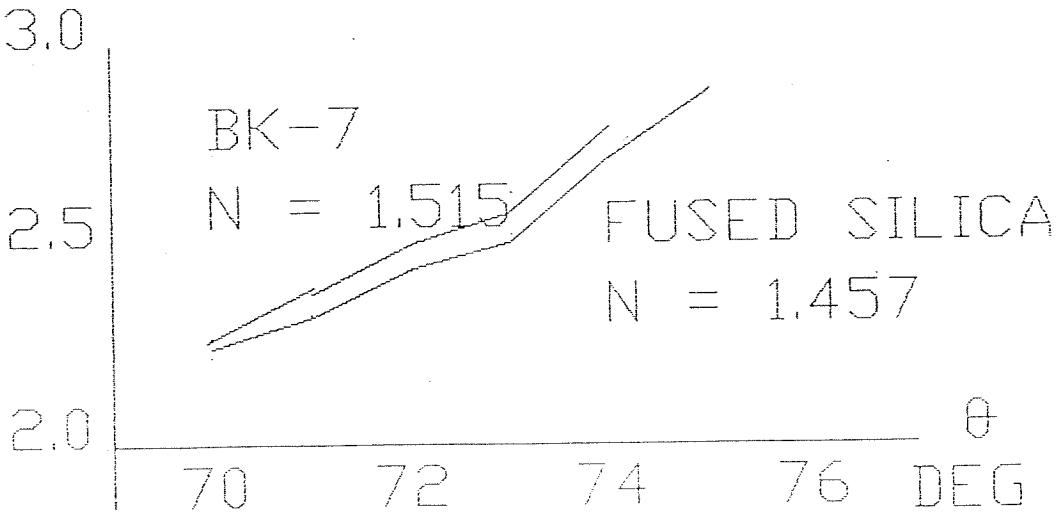

Fig. A-1

camera modification I

REPLACE C6 BY

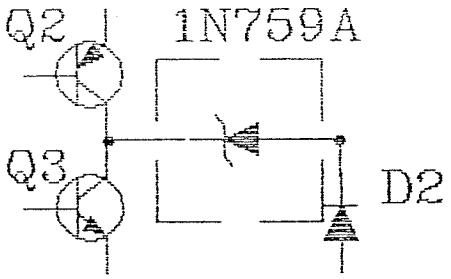

REPLACE C12 BY

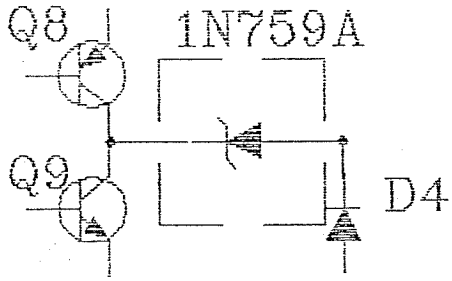

REPLACE C18 BY

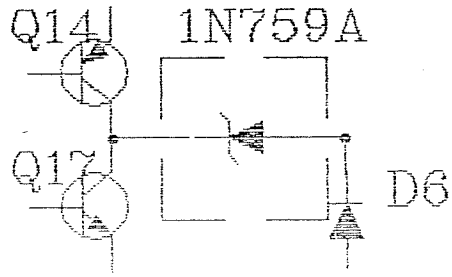

Fig. A-2

Camera modifications II and IV

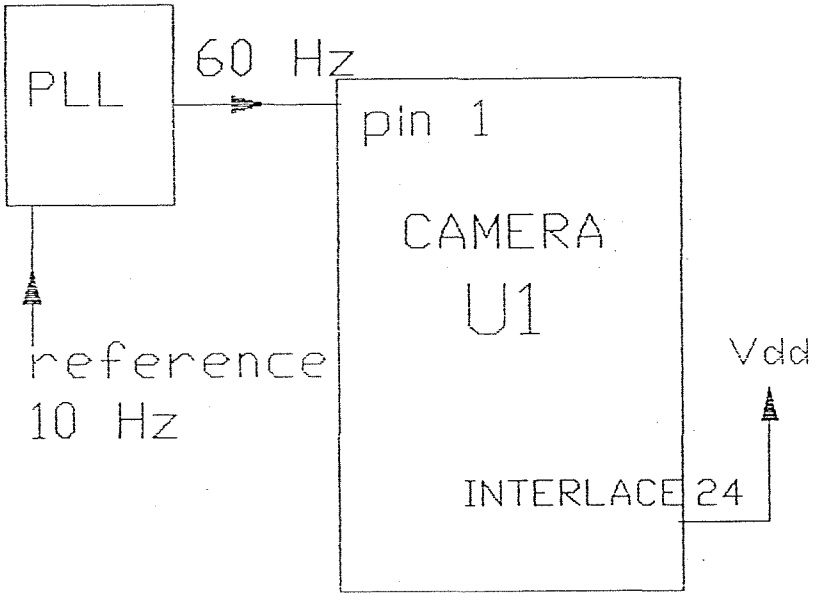

Fig. A-3

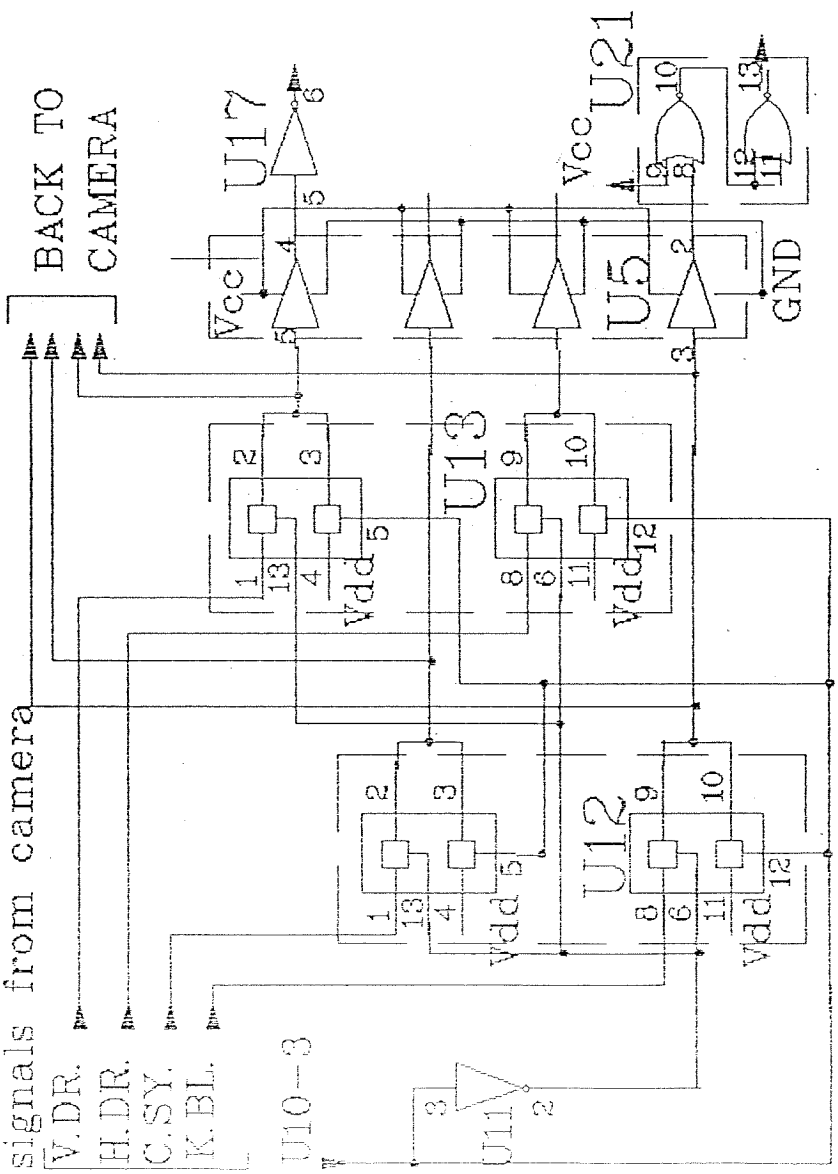

Fig. A-4 Camera modification III

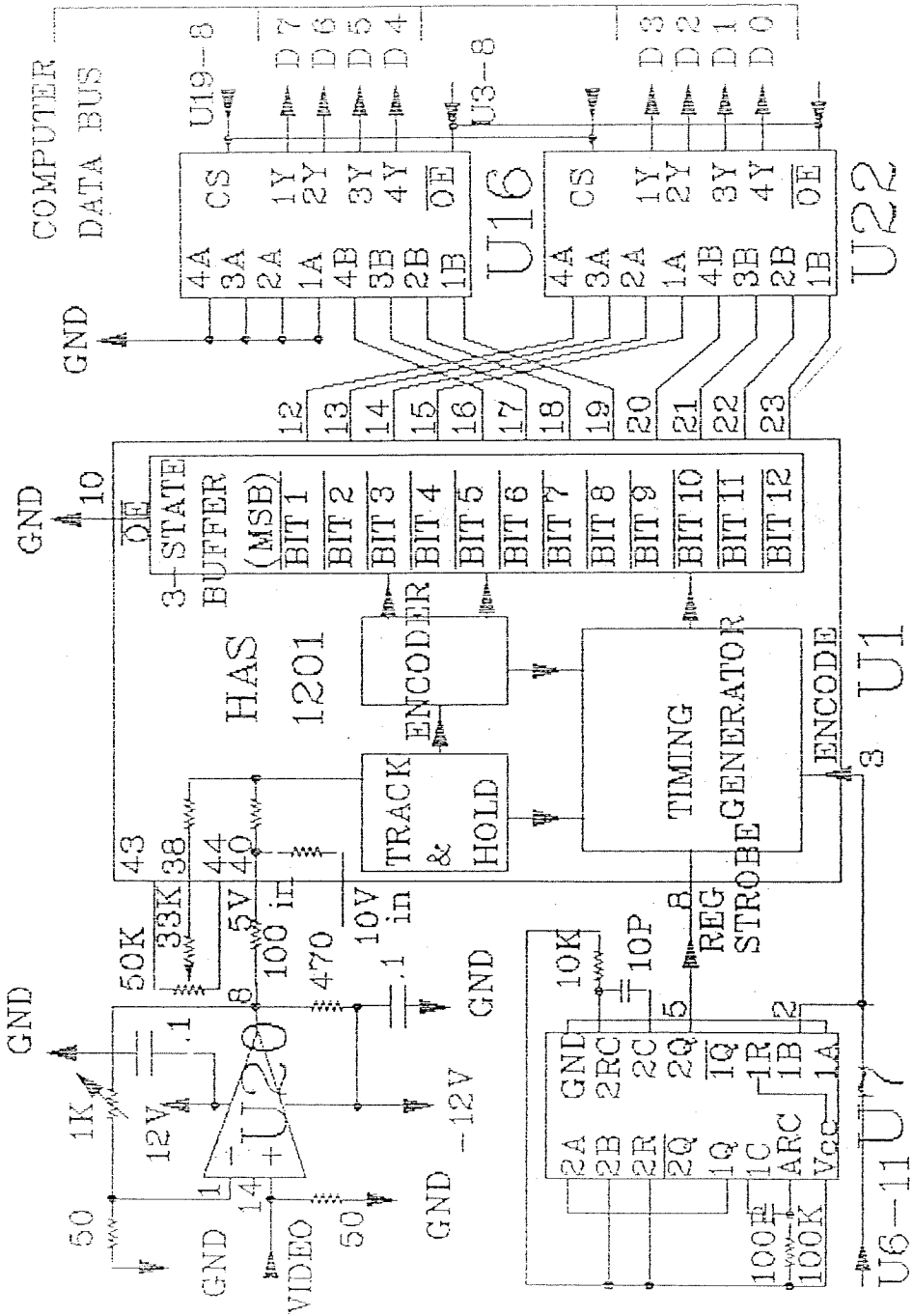

Fig. A-5 A/D converter

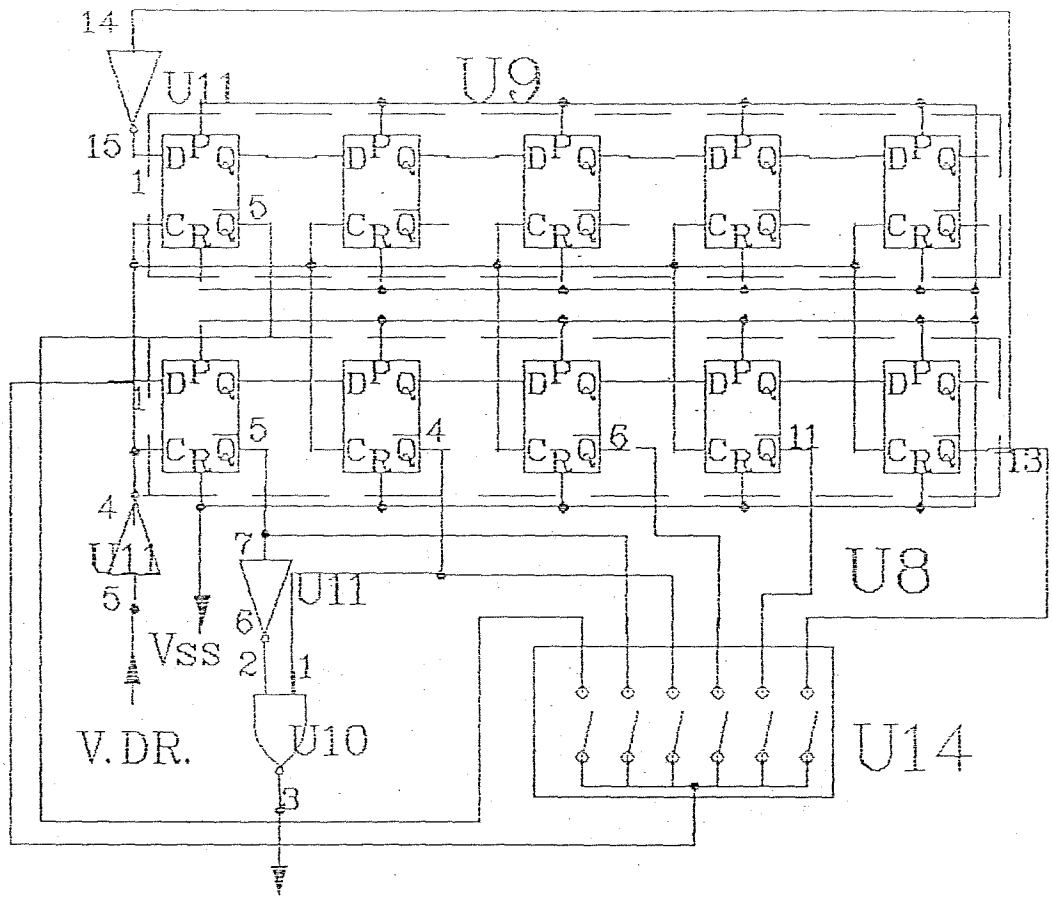

Fig. A—6 Control of integration time

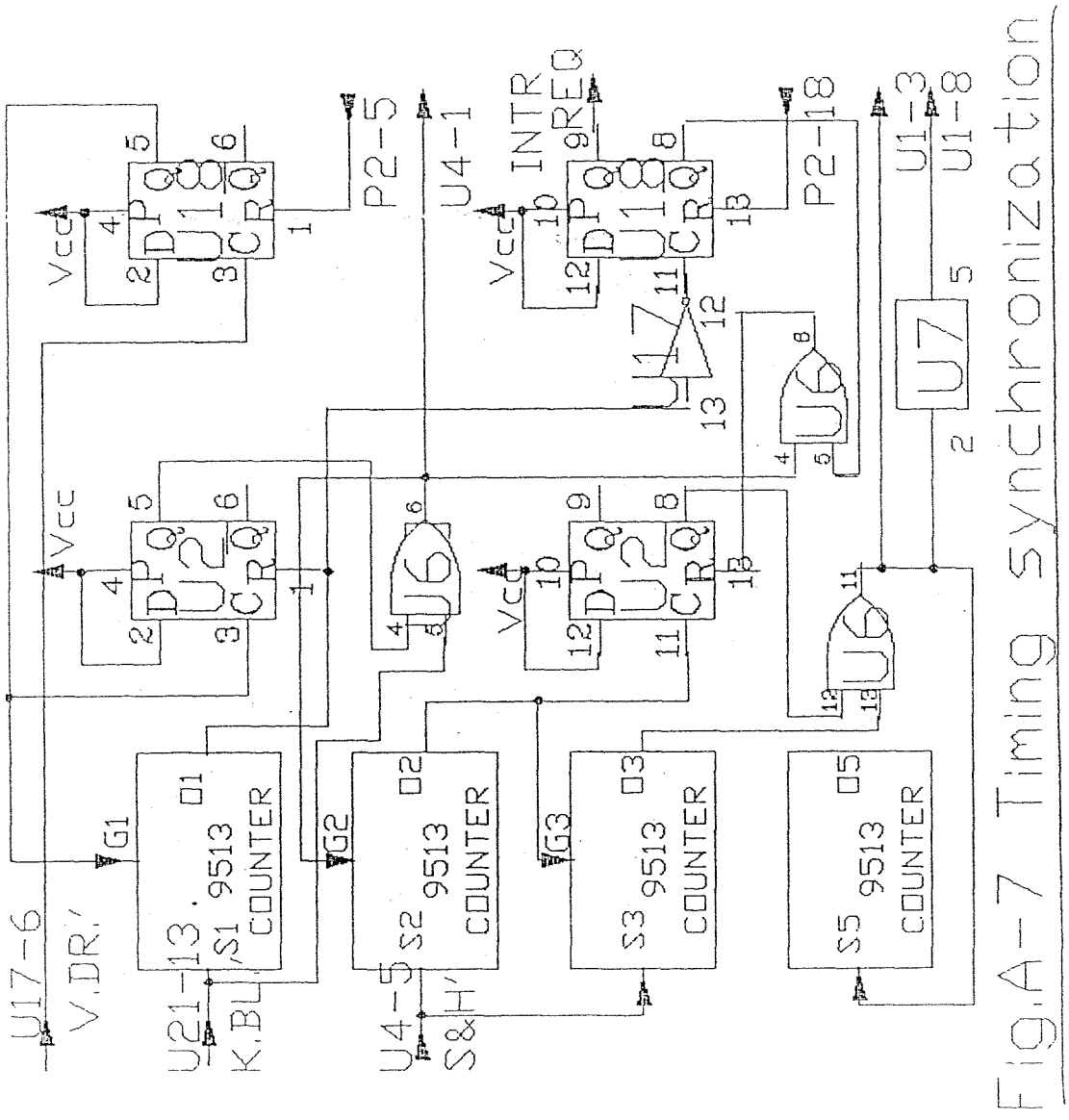

Fig.A-7 Timing synchronization

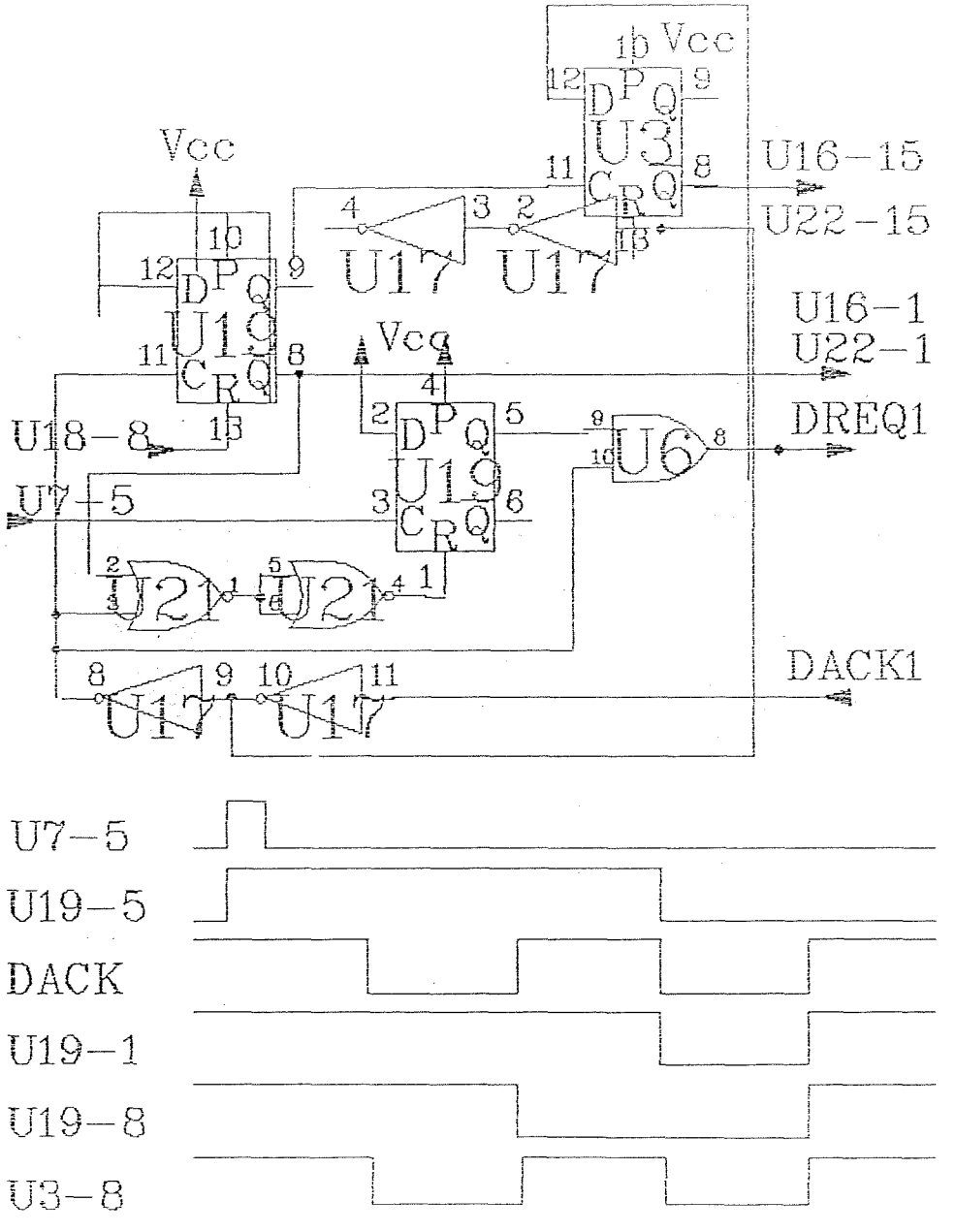

Fig.A-8 DMA request

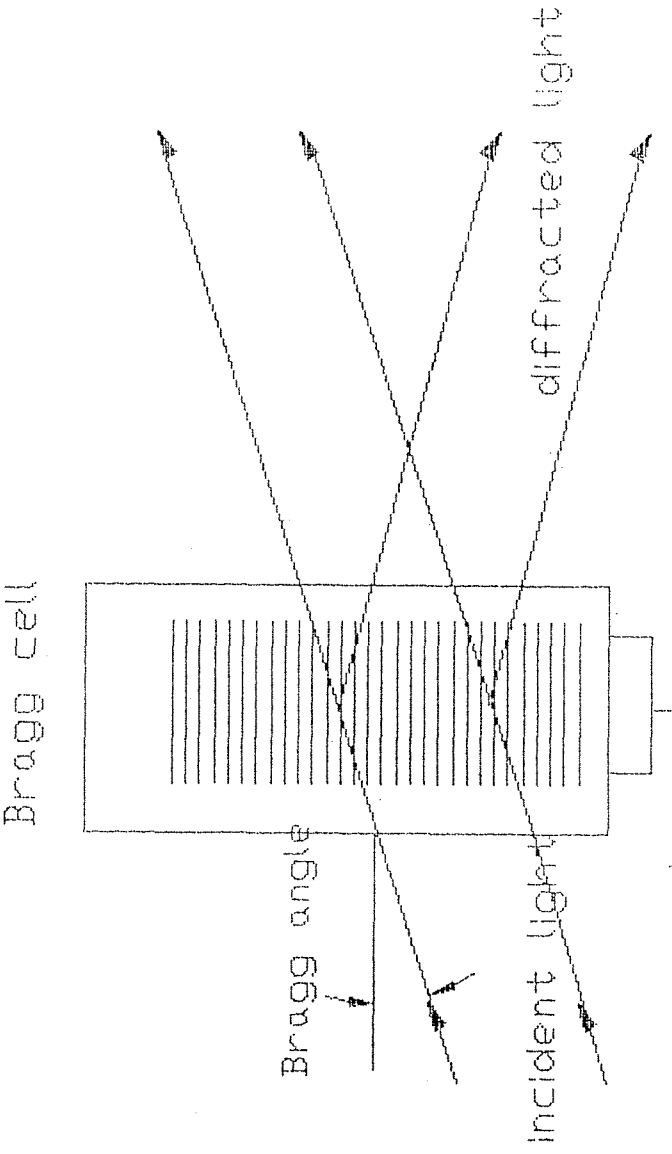

Fig. B-1 A Bragg cell

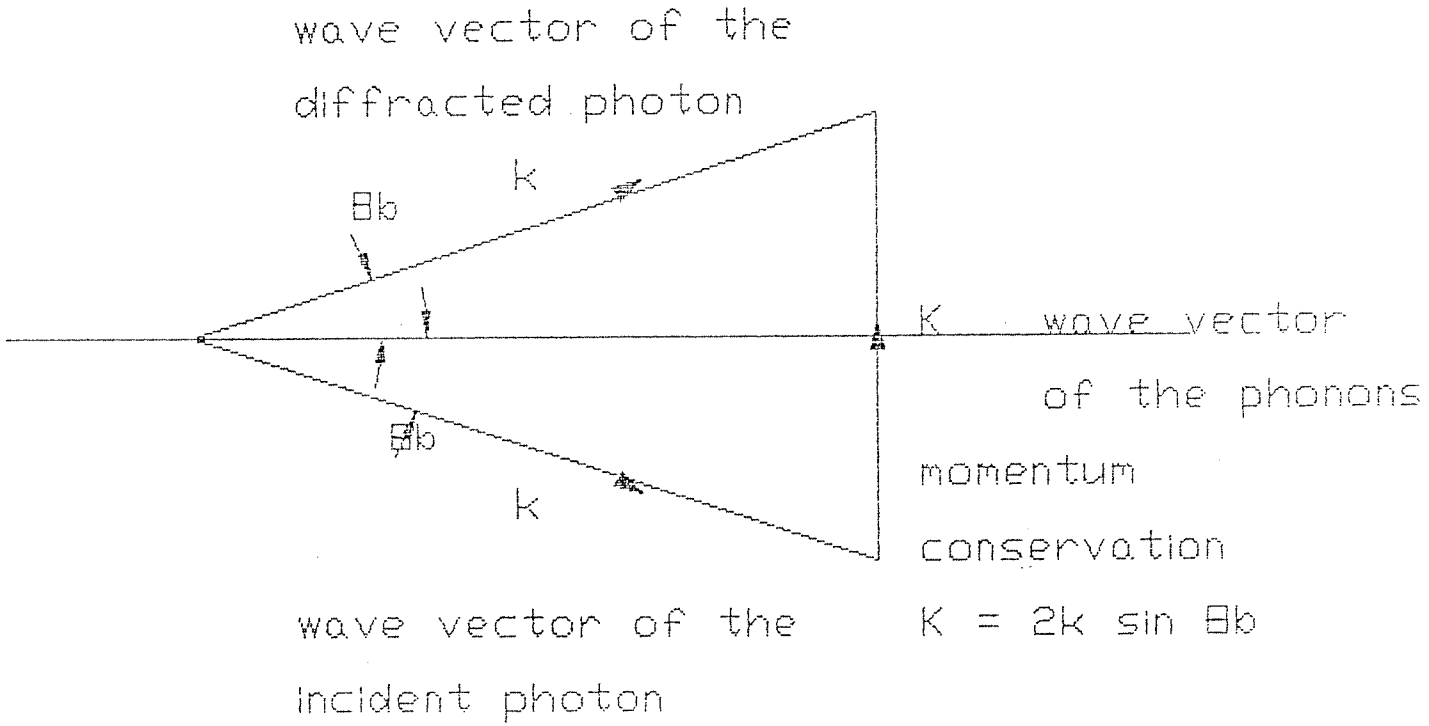

Fig. B-2 Momentum conservation

at the Bragg condition

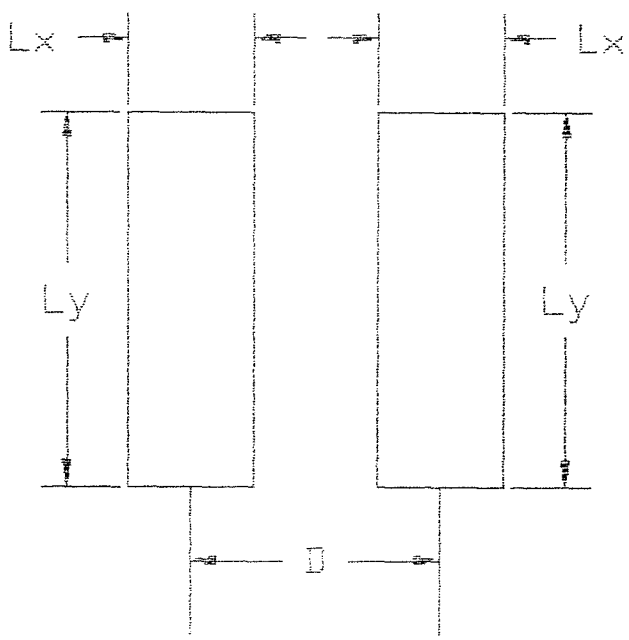

Fig. C-1 Two rectangular apertures